Flavor Fluctuations in Central Pb+Pb Collisions at 158 GeV/Nucleon

Dissertation
zur Erlangung des Doktorgrads
der Naturwissenschaften
vorgelegt beim Fachbereich Physik
der Johann Wolfgang Goethe-Universität
in Frankfurt am Main
von
Christof Roland
aus Frankfurt am Main

Frankfurt am Main
Oktober 1999
(D F 1)

Vom Fachbereich Physik der
Johann Wolfgang Goethe-Universität als Dissertation angenommen.

Dekan:	Prof. Dr. Reinhard Stock
Gutachter:	Prof. Dr. Reinhard Stock
	Prof. Dr. Horst Stöcker

Datum der Disputation:

Zusammenfassung

Das Ziel der Untersuchung von ultra-relativistischen Schwerionenkollisionen ist die Suche nach dem Quark Gluon Plasma (QGP), einem Zustand hochdichter stark wechselwirkender Materie in dem der Einschluss von Quarks und Gluonen in Hadronen aufgehoben ist. Die bisher gewonnenen experimentellen Hinweise deuten darauf hin, daß in Schwerionenkollisionen bei den derzeit höchsten zur Verfügung stehenden Energien von 158 $GeV/Nukleon$ in Pb+Pb Reaktionen am CERN-SPS die Rahmenbedingungen für einen Phasenübergang von hadronischer Materie zu einer partonischen Phase erfüllt sind.
Die exakte Phasenstruktur stark wechselwirkender Materie hingegen ist derzeit noch nicht vollständig verstanden. Da inklusive hadronische Observablen und "penetrierende Proben" nicht direkt sensitiv auf die Existenz und Natur des Phasenübergangs sind, wurde die Analyse von Einzelereignis- *"event-by-event"*-Fluktuationen vorgeschlagen. Das Fluktuationsverhalten von Einzelereignis-Observablen sollte direkt sensitiv auf die Natur des zu beobachtenden Phasenübergangs sein.
In dieser Arbeit wurden Fluktuationen in der "chemischen" Zusammensetzung der Teilchenquelle untersucht und erste Ergebnisse werden präsentiert. Die im Vergleich zu elementaren Nukleon-Nukleon Stössen beobachtete Überhöhung der Seltsamkeitsproduktion in Schwerionenkollisionen um einen Faktor 2 gilt als ein wichtiges Indiz für einen veränderten Teilchenproduktionsmechanismus aufgrund der kollektiven Natur des erzeugten Vielteichensystems. Als Observable für den Seltsamkeitsgehalt einzelner Schwerionenreaktionen wurde das Verhältnis geladener Kaonen zu geladenen Pionen gewählt ($< K^+ + K^- > / < \pi^+ + \pi^- >$). Kaonen als leichteste, Seltsamkeit tragende, Teilchen werden in einzelnen Reaktionen in ausreichender Zahl produziert um eine statistisch signifikante Aussage über den gesamten Seltsamkeitsgehalt der erzeugten Teilchenquelle zu machen.
Das NA49 Experiment wurde vor dem Hintergrund konzipiert, eine solche Einzelereignisanalyse zu ermöglichen. Grundvoraussetzung hierfür ist es, den hadronischen Endzustand von Schwerionenkollisionen möglichst vollständig zu erfassen und die gemessenen Teilchen zu identifizieren. Dazu stehen vier großvolumige Spurendriftkammern zur

Verfügung, die es ermöglichen, durch Rekonstruktion der Teilchentrajektorie in einem Magnetfeld den Teilchenimpuls zu bestimmen und zusätzlich durch Messung der spezifischen Ionisation die Teilchensorte zu identifizieren.
Die Einzelereignisanalyse mit Hilfe von Spurendriftkammern in einer Umgebung solch hoher Spurdichte stellt eine grosse experimentelle Herausforderung dar. Um systematische Fehler in der Messung von Einzelereignisfluktuationen zu vermeiden, ist es unbedingt notwendig sicherzustellen, daß Variationen der lokalen Spurdichte die Leistungsfähigkeit des Detektors nicht beeinflussen.
Im Rahmen dieser Arbeit wurden zwei relevante Ursachen für systematische Unsicherheiten in der Fluktuationsmessung identifiziert, die von der lokalen Spurdichte beeinflusst werden:

- Die Effizienz der Spurrekonstruktion.

- Die Ionisationsmessung zur Teilchenidentifizierung.

Eine eingehende Untersuchung der Spurerkennungsprogramme hat gezeigt, daß ein gewisser Teil der gemessenen Spuren in mehrere Spurstücke aufgebrochen wird, was zu einer Mehrfachmessung von einzelnen Spuren führt. Im Rahmen dieser Arbeit wurden Mechanismen zur Erkennung und Zusammenfügung aufgebrochener Spuren entwickelt (Kapitel 3).
Erste Untersuchungen der Teilchenidentifizierung durch Messung der spezifischen Ionisation haben gezeigt, daß die Leistungsfähigkeit der Detektoren weit hinter den erwarteten Werten zurück bleibt. Insbesondere wurde eine starke Abhängigkeit der Ionisationsmessung von der lokalen Spurdichte festgestellt.
Durch eine genaue Untersuchung der Ausleseelektronik und des Aufbaus der Auslesekammern konnten Nullinienverschiebungseffekte und ein Übersprechen zwischen den einzelnen Auslesekanälen über die Auslesedrähte der Proportionalkammern als Ursache identifiziert werden. Es wurden im weiteren Korrekturmechanismen entwickelt um diese Effekte zu korrigieren (Kapitel 4). Die zuvor beobachtete Spurdichteabhängigkeit der Ionisationsmessung konnte beseitigt und das Trennungsvermögen der Spurendriftkammern konnte um einen Faktor 1.5-2 (siehe Abb. 1) erhöht werden. Die schliesslich erreichte Auflösung in der Messung der spezifischen Ionisation liegt knapp unter 4%, was ein mit diesem Detektortyp bei hoher Spurdichte bisher unerreichtes Qualitätsniveau darstellt.
Im Hinblick auf die Einzelereignisanalyse des K/π-Verhältnisses wurde eine Methode zur Extraktion dieses Verhältnisses aus Ereignissen stark limitierter Statistik (ca. 400 Teilchen in der Akzeptanz) entwickelt und deren Sensitivität und systematisches Verhalten untersucht (Kapitel 5).

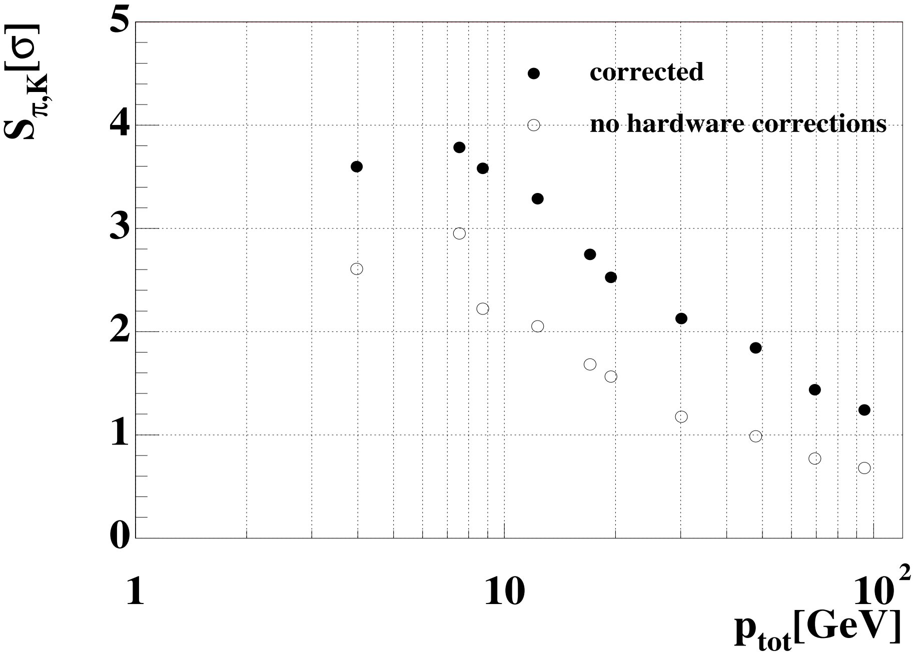

Abbildung 1:
Trennungsvermögen der Teilchenidentifikation $S_{K,\pi}$ zwischen Kaonen und Pionen in Einheiten von Standardabweichungen als Funktion des Gesamtimpulses p_{tot}. Die korrigierten Daten sind durch gefüllte Symbole dargestellt. Die offenen Symbole entsprechen einem Datensatz ohne die im Rahmen dieser Arbeit entwickelten Korrekturalgorithmen.

Mit dieser Methode wurden in zentralen Pb+Pb Stössen bei 158GeV/Nukleon dynamische Fluktuationen im K/π-Verhältnis von nur $2.8\% \pm 0.5\%$ ermittelt (siehe Abb. 2). Die beobachtete Verteilung des Einzelereignis-K/π-Verhältnisses weicht nur geringfügig von einer rein statistischen Verteilung ab. Damit können "kritische Fluktuationen" im K/π-Verhältnis mit hoher statistischer Signifikanz ausgeschlossen werden (Kapitel 6).
Vergleiche mit String-Hadronischen Modellen haben gezeigt, daß die lokale Erfüllung von Erhaltungsätzen (z.B. Seltsamkeit, Energie, etc), die implizit in diesen Modellen enthalten ist, zu Fluktuationen des K/π-Verhältnisses führt, die durch die im Rahmen dieser Arbeit durchgeführte Analyse ausgeschlossen werden können. Der Einfluß von hadronischen Endzustandswechselwirkungen auf Fluktuationen des K/π-Verhältnisses wurde mit Hilfe des UrQMD-Models untersucht.

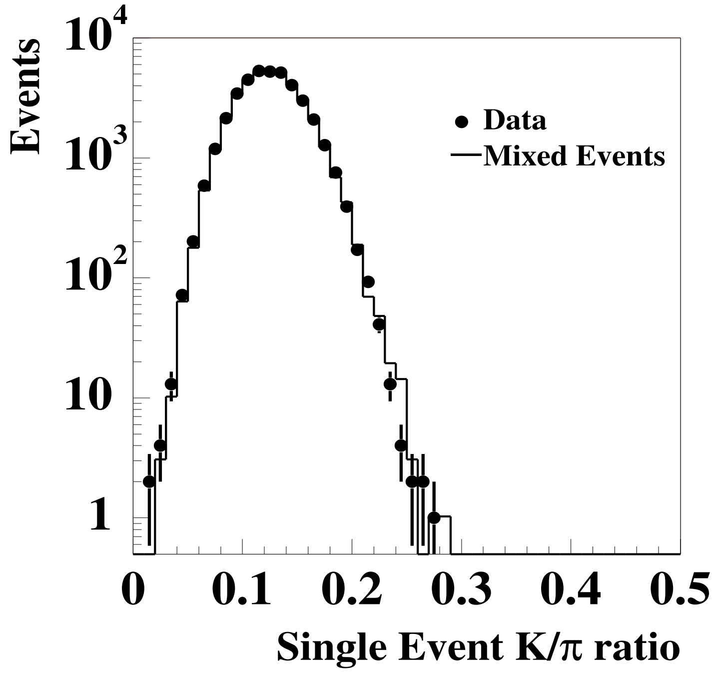

Abbildung 2:
Einzelereignisverteilung des K/π-Verhältnisses (Punkte). Die durchgezogene Linie zeigt als Referenz die Verteilung des K/π-Verhältnisses für gemischte Ereignisse. Aus dem Unterschied in der Breite der Verteilungen läßt sich das Signal für dyanische Fluktuationen von $2.8\% \pm 0.5\%$ abschätzen.

Ein Vergleich zu einem thermisch und chemisch equilibrierten Resonanz-Gas hat gezeigt, daß die Fluktuationen des K/π-Verhältnisses die aus der korrelierten Produktion der beobachteten Teilchensorten durch den Zerfall von höher angeregten Resonanzen herrühren, das in zentralen Pb+Pb Stößen beobachtete Signal fast vollständig erklären können.
Infolgedessen kann das Ergebnis dieser Arbeit durch die Feststellung zusammengefasst werden, daß in zentralen Blei-Blei-Stößen keine wesentlichen Fluktuationen der hadrochemischen Komposition gefunden werden. Dieser Befund wäre zu erklären durch die Annahme eines kollektiven Hadronisierungsprozesses, der chemisches Gleichgewicht in der entstehenden Hadronenphase erzwingt. Man sieht also durchaus den Einfluß eines Phasenübergangs von partonischen zu hadronischern Freiheitsgraden, nur daß dieser Übergang nicht zu kritischen Fluktuationen führt, sondern im Gegenteil zu einer streng statistisch populierten Hadronenphase.

Contents

1 Introduction

1.1 Heavy-Ion-Physics

Several decades ago deep inelastic lepton-nucleon scattering revealed the inner structure of the nucleon. Each nucleon was found to be built of three pointlike elementary particles, called "partons" in the Parton Model arising from this observation. The gauge theory of the strong interactions, **Quantum Chromodynamics (QCD)**, later on identified these partons with the quarks (q) and antiquarks ($\overline{q}$) of the static Quark Model proposed by Gell-Mann and Zweig. Experiments have identified 6 different types (*flavors*) of quarks (up u, down d, strange s, charm c, bottom b and top t) and their antiquarks. However no free quarks have been observed so far despite many experimental searches, rather they seem to exist only as bound states of quark-antiquarks $q\overline{q}$ (mesons), or triplets of (anti)quarks ($\overline{qqq}$) qqq.
In QCD three *color* quantum numbers representing the charges of the strong interaction are introduced to accommodate the fermionic nature of bound states of 3 identical quarks, e.g. Δ^{++} (uuu). In the QCD vacuum only color neutral objects are allowed to propagate freely. This is attributed to the fact that *gluons*, the exchange quanta mediating the strong interaction, carry color charge and thus can interact with themselves. Color neutrality or *color confinement* for hadrons is realized by combining color and anticolor ($q\overline{q}$) or the exact amount of each of the 3 (anti)colors ($\overline{qqq}$) qqq.
Due to the self interaction of the gluons the vacuum polarization induced by a quark produces an antiscreening effect which spreads out the effective color charge of the quark. As a consequence the coupling between quarks is small in case of short distances or large momentum transfers $V_{QCD} \propto 1/r$, but increases proportional to the distance $V_{QCD} \propto r$ for small momentum transfers or large distances. This effect is often referred to as "*asymptotic freedom*". When a quark antiquark pair is separated it becomes energetically favorable for the color field to break up and form an extra quark antiquark pair instead of freeing a bound quark. It was suggested [1, 2], however, that at high energy densities or high temperatures quarks would behave as essentially free particles forming

a collective state of strongly interacting matter, the **Quark Gluon Plasma (QGP)**, see figure 1.1.

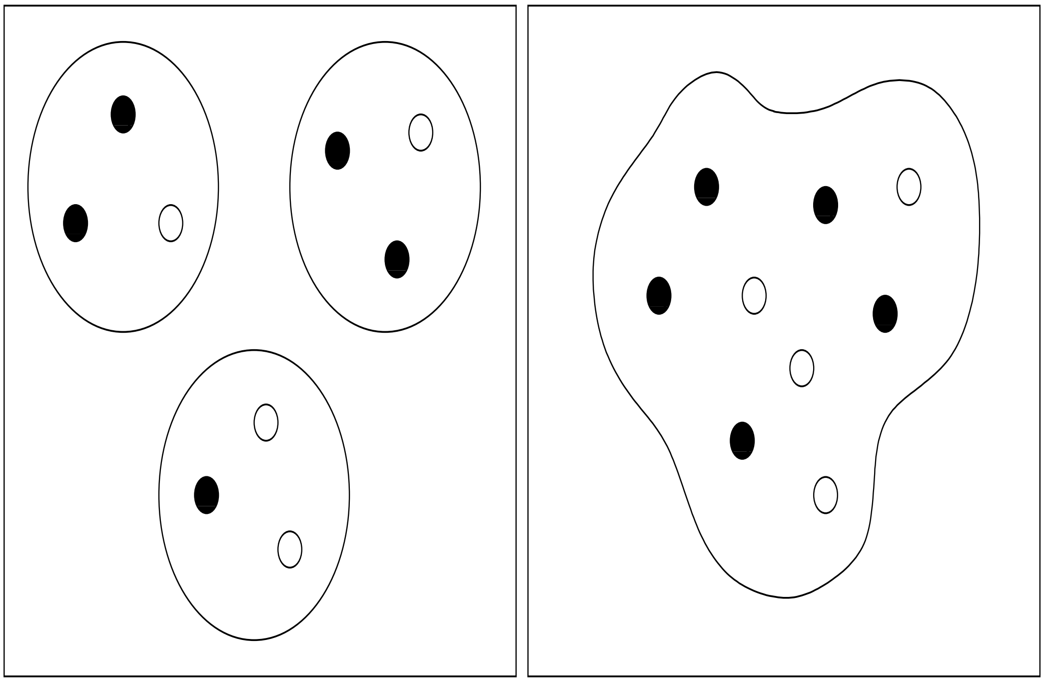

Figure 1.1 Left: in normal nuclear matter the quarks are confined inside nucleons. Right: In a QGP the quarks are free to move inside the plasma.

The theoretical treatment of the QGP was found to be exceedingly difficult since QCD can be treated by perturbative calculations only in the case of weak coupling between the color charges, i.e. at small distances or high momentum transfers. The non-perturbative part of QCD so far can only be studied by the computational techniques of Lattice QCD, that places quarks and gluons on a lattice and simulates their interactions.
The phase structure of the QCD is not yet fully understood. A sketch of the phase diagram of strongly interacting matter is shown in figure 1.2. Reliable lattice calculations exist only for net baryon free matter in which a 2-nd order phase transition or crossover at $T_c \approx 160 MeV$ is predicted. Recent calculations [3, 4, 5, 6] based on different models reveal the possibility of a 1-st order phase transition at large baryon chemical potentials. The existence of a tricritical point separating regions of 1-st and 2-nd order transitions has been predicted. Possible signatures of the transition in heavy-ion collisions are discussed in [7, 8].

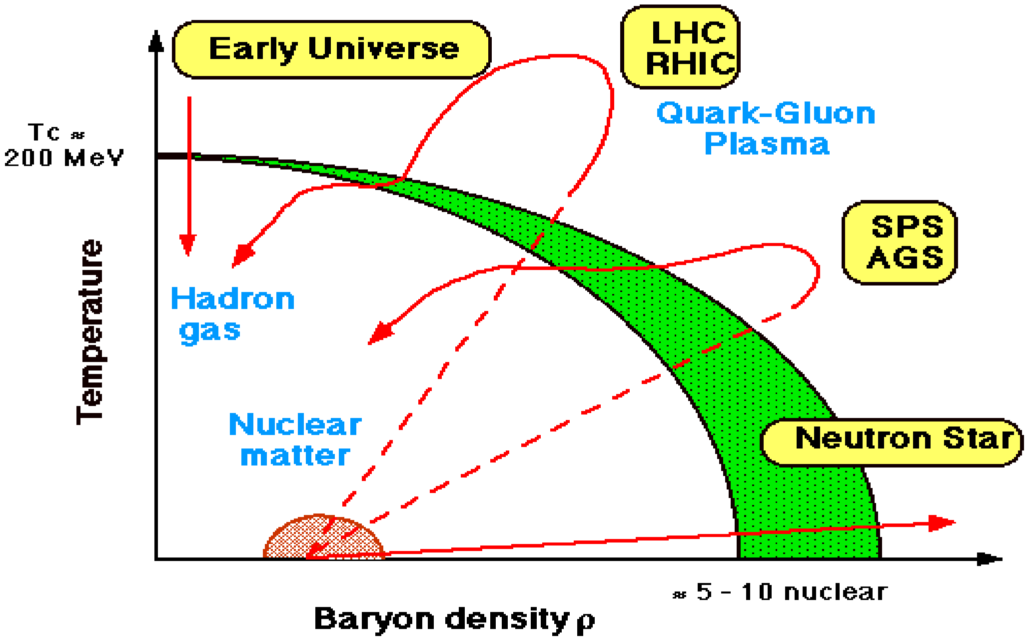

Figure 1.2 The phase diagram of nuclear matter. The lines describe different scenarios in which a QGP could have been created.

Due to the confinement of color charges, only colorless, hadronic final states can be observed experimentally. Therefore QGP properties can be studied only indirectly through the final hadron distributions or by penetrating electromagnetic probes. The experimental evidence collected so far suggests that the necessary conditions for a deconfined phase are indeed reached in heavy ion collisions at the highest energies available now. The CERN[1]-SPS[2] accelerator facility provides a ^{208}Pb-beam with a beam energy of 158 $GeV/nucleon$, which corresponds to a center of mass energy of 18 $GeV/nucleon-pair$. The energy density reached in these collisions has been estimated to be about 3 GeV/fm^3 [9] which is to be compared to the nuclear ground state energy density of 0.15 GeV/fm^3. The freeze out temperature of the hadronic particle abundances ("chemical freeze out") can be estimated within thermodynamical models [10, 11] and was found to be about 180 MeV. An extensive summary of the experimental evidence, indicating that the initial conditions for a deconfined partonic phase have been reached in heavy ion collision is presented in [12].

---

[1]Centre Européenne pour la Recherche Nucléaire, Genève
[2]Super Proton Synchrotron

1.2 Event-by-Event Fluctuations

One of the difficulties of the search for the Quark Gluon Plasma is the insensitivity of inclusive observables to the phase transition itself. It was realized however, that event-by-event fluctuations could provide a direct probe of the existence and nature of the phase transition [13]. One expects that the fluctuation patterns are altered in the vicinity of the QCD phase transition [14, 15]. This conjecture is supported by recent calculations in an effective model of strong interactions [16, 17], which suggest that near a tricritical point in the QCD phase diagram the event-by-event fluctuation pattern in transverse momentum should change significantly.

A precise measurement of event-by-event fluctuation of the average transverse momentum allows for a test of the hypothesis of thermal equilibrium [18] and the extraction of thermodynamical properties of the system in a model comparison. Model studies [19] have shown that non-equilibrium models of nuclear collisions based on initial state scattering can be tested by measurements of transverse momentum fluctuations. Transverse momentum fluctuations have been analyzed in the framework of many of the commonly used microscopic models of nuclear collisions [20, 21, 22], focusing in particular on the question of how the fluctuations change when going from nucleon-nucleon to nucleus-nucleus collisions.

It has been suggested that for a thermodynamical picture of the strongly interacting system formed in the collision the strength of fluctuations is directly related to fundamental properties of the system like the specific heat [23, 24] and the compressibility of matter [25]. A detailed discussion of transverse momentum fluctuations in a resonance gas model can be found in [17].

So far one of the most prominent indications for a change in the particle production mechanism due to the collective nature of heavy ion collisions is the relative enhancement of strangeness production with respect to pions compared to elementary nucleon-nucleon collisions.

From the K/π ratio defined here as $< K^+ + K^- > / < \pi^+ + \pi^- >$, an estimate can be made [28, 29] of the overall freeze out ratio of strange to non-strange quarks in the final state. Defining a strangeness suppression factor λ_s

$$\lambda_s = \frac{2 \cdot (s + \overline{s})}{(u + \overline{u} + d + \overline{d})} \tag{1.1}$$

a value of $\lambda_s = 0.34 \pm 0.05$ was found in light ion (S+S) collisions at SPS energy [26, 27] corresponding to a K/π ratio of about 0.14 at midrapidity. This compares to a value of $\lambda_s = 0.17 \pm 0.03$ for nucleon+nucleon collisions [28, 29] at the same energy per nucleon, which results in the often quoted strangeness enhancement by a factor of about 2.

To motivate the study of event-by-event fluctuations of the K/π ratio it was argued that for events that have gone through a QGP phase λ_s ideally should approach unity due to the equal population of up, down and strange quarks.

Taking into account the presence of u,d valence quarks and the finite s-quark mass a value of $\lambda_s \leq 0.65$ can potentially be reached. Thus "plasma candidate" events might exhibit a fourfold enhancement of the K/π ratio compared to nucleon-nucleon collsions. However if the initial conditions of the collision are close to the phase boundary the transition to a QGP phase need not occur in every heavy ion reaction due to the finite extent and short life-time of the system. Thus events exhibiting the critical behaviour of a QGP phase transition might be lost in an inclusive analysis, whereas they might form a high K/π tail or shoulder in the histogram of an eventwise determination of that ratio. Alternatively, if a transition occured in almost every event, and the free enthalpy difference between the two phases were high, it was suggested by Mekjian and Kapusta [30] that a marked overheating-supercooling fluctuation might set in about the critical temperature T_c, to be reflected in a broadening of the event-by-event K/π distribution as the K/π ratio increases with T.

The availability of a Pb beam at the CERN-SPS and the resulting central Pb+Pb collisions with an expected multiplicity of over 1000 charged particles allowed for the first time to measure the K/π ratio on an event-by-event basis with the hope to distinguish "plasma events" from the normal data, or more generally study the event-by-event fluctuations in this observable to investigate the dynamics of heavy ion collisions.

Experimentally however this measurement features the challenging task of covering a large fraction of phase space with a detector capable of particle identification. One of the prime design considerations of the NA49-Experiment was to allow for excellent particle identification over a wide region of phase space in order to provide a statistically significant measurement of the chemical composition of the particle source on an event-by-event basis.

In this thesis we will show that the detector setup of the NA49 experiment is indeed capable of a high precision measurement of the strangeness content of single Pb+Pb collisions. The first measurement of event-by-event flavor fluctuations in heavy ion collisions will be presented. We will show in particular that the experimental eventwise K/π distribution puts extraordinarily narrow constraints on the existence of any large scale fluctuation of the K/π ratio, thus practically ruling out a pre-critical fluctuation as well as an "exotic event" shoulder. In fact the observed fluctuation of about 3% can be ascribed solely to the statistical sampling of kaons and pions from a fixed thermal equilibrium hadron plus resonance gas at $T = 180 MeV$. If this state results from the hadronization mechanism of a preceeding partonic phase [12] the hadronisation has to occur uniformly, in every central Pb+Pb collision, and exhibit no large enthalpy jump.

2 The NA49-Experiment

2.1 The Experimental Setup

The opportunity to study heavy-ion collisions of ^{208}Pb-ions at $158 GeV$/nucleon with an expected multiplicity of about 1800 charged hadrons gave rise to the idea of an *event-by-event* analysis of the hadronic final state of these reactions. In electron-positron collider experiments this method has been successfully used to isolate single events showing interesting collective features from millions of irrelevant ones. The NA49-Detector system was conceived with the goal in mind to gather as much information per event as possible to enable an event-by-event analysis of many different observables. The prime prerequisite for such an analysis is large phase space coverage including particle identification. For a fixed target experiment at the CERN-SPS uniform acceptance and satifactory rapidity coverage put serious and demanding constraints on the detector setup to be chosen.

The detector concept of NA49 features a wide acceptance magnetic spectrometer consisting of two superconducting magnets of $9Tm$ bending power and four large volume Time Projection Chambers (TPC) used for momentum measurement by tracking the particle trajectory and for particle identification by measuring the specific ionization. In addition to the tracking system four time-of-flight walls provide further particle identification capability and calorimeters are employed for measurement of transverse energy production and for triggering purposes.

A complete description of the experimental setup can be found in [31]. Fig. 2.1 gives a schematic overview of NA49-detector system. In this chapter the parts of the detector system relevant to this thesis will be described in more detail.

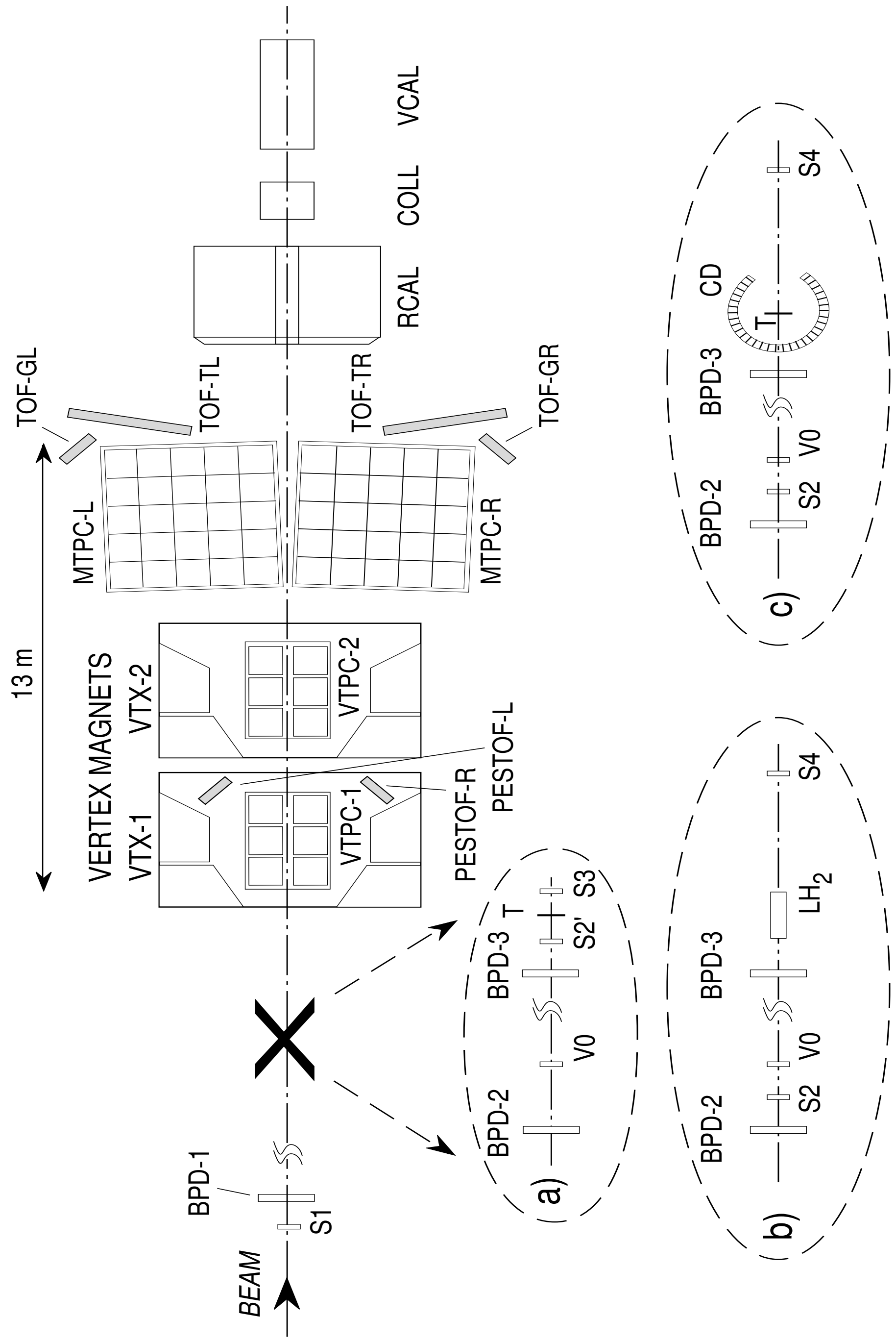

Figure 2.1 Setup of NA49-Experiment with different beam definitions and target arrangements for a) Pb+Pb, b) p+p, c)p+A collisions. The target position is at the front face of the first Vertex Magnet (VTX-1).

2.2 The Tracking System

The need for a large acceptance, low mass occupation along the particle trajectories and precise three-dimensional imaging made the Time Projection Chamber the natural selection. The tracking ability of this detector concept in a high track density environment has been demonstrated by NA35 and NA36 [32, 33] at CERN, EOS [34] at LBL[1] and E810 [35] at AGS[2]. Since the TPC is often used in particle physics and has been described frequently in literature (e.g. [36, 37]) only a short introduction to the basic properties will be given here. Also the operation principles of drift chambers and proportional counters has already been discussed to great detail ([37, 38, 43, 44]). A more detailed description of the NA49 TPCs can be found in [45] and [46].
A charged particle traversing the gas filled detector volume, ionizes the atoms by Coulomb interaction with the electrons of the gas molecules. A drift field of about 100 V/cm transports the free electrons produced along the particles trajectory with a constant velocity towards the proportional chamber readout of the detector. There the electrons are accelerated in the high electric field around the *sense*-wires and amplified by gas-multiplication by a factor of about 10^4. The signals are picked up on the segmented cathode plane.

The NA49-Time Projection Chambers

Design and dimensions of the NA49 TPCs are defined by the strong forward focusing of the particle trajectories due to the fixed-target kinematics at SPS energies and magnetic aperture of the existing magnets. The particle emission angle in the range of $100 mrad$ at central rapidity and the large transverse momentum kick of 1.5 GeV/c provided by the magnetic fields suggested the detector setup illustrated in Fig.2.1. One vertex-chamber (VTPC) is positioned inside each of the two magnets and two large main-chambers (MTPC) are positioned left and right of beam outside the magnetic field downstream of the magnets.

Mechanical Construction

Fig.2.2 shows the mechanical setup of one of the Vertex-TPCs. The backbone of each TPC is an aluminum support plate to which all the components are fixed and which also defines the geometric position of the detector. The support plates give a reference plane

---
[1] Lawrence Berkeley Laboratory, Berkeley, USA
[2] Alternating Gradient Sychrotron at Brookhaven National Laboratory, Brookhaven USA

for the TPC readout of $\pm 50\mu m$ in case of the VTPCs and $\pm 150\mu m$ for the MTPCs. Table 2.1 gives a summary of the overall geometrical dimensions of the TPC systems.

dimensions [mm]	VTPC-1	VTPC-2	MTPC-L/R
width	2000	2000	3900
length	2500	2500	3900
height	980	980	1800
drift length	666	666	1117
pad length	16, 28	28	40
pad width	3.5	3.5	3.6, 5.5
pad angles	12–55°	3–20°	0°, 15°

Table 2.1 Geometrical dimensions of the TPC system

The field cages and the gas envelopes are carried by the support plates which also house the readout proportional chambers. The field cage defining the active volume of the TPCs consists of aluminized mylar strips of $25\mu m$ thickness and $12.7mm$ width suspended on ceramic tubes placed at the corners of the support frame. The strips are positioned with a $2mm$ distance between the strip edges. Each strip layer is set to a fixed potential by a resistor chain connecting the HV-plane (about $13kV$) with ground potential in order to ensure a homogenous drift field.
The field-cage is enclosed in a gas-envelope. This envelope consists of a double layer of $125\mu m$ mylar foil glued to a double frame system made of $6mm$ thick fiberglass-epoxy. The thin $(1-2cm)$ gas volume between the two foils is flushed with Nitrogen and serves as high voltage protection and also ensures a minimum of Oxygen diffusing into the sensitive volume.

Choice of Gases

The large particle multiplicities produced in central heavy ion collisions lead to extreme track densities of up to 0.6 particles per cm^2 in the plane orthogonal to the beam direction. In order to make pattern recognition of close tracks possible the spatial extension of the electron cloud drifting in the gas volume, that is mainly given by diffusion, has to be minimized accordingly. Essentially gases with low transverse and longitudinal diffusion coefficients have to be chosen. This is especially important since the MTPCs are operated outside the magnetic field so one can not rely on cluster focusing $E \times B$-effects to compensate the diffusion of the drifting electron clouds [44]. Fig. 2.3 illustrates the properties of different gas mixtures investigated. A parametrisation of the

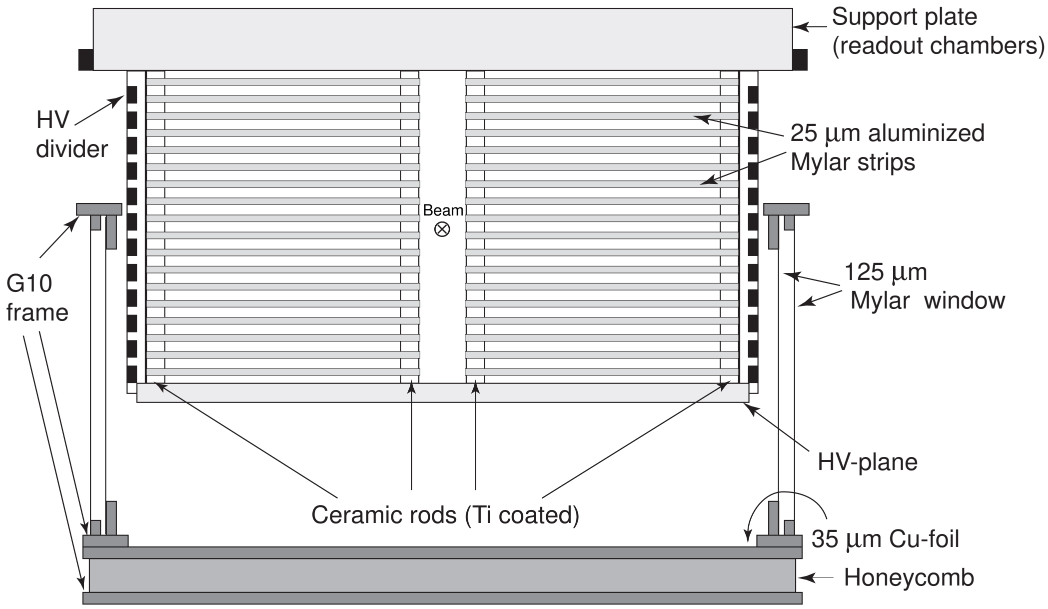

Figure 2.2 Schematic drawing of the assembly of one of the VTPCs showing the support plate housing the readout chambers, the two field cages on both sides of the beam, and the gas box.

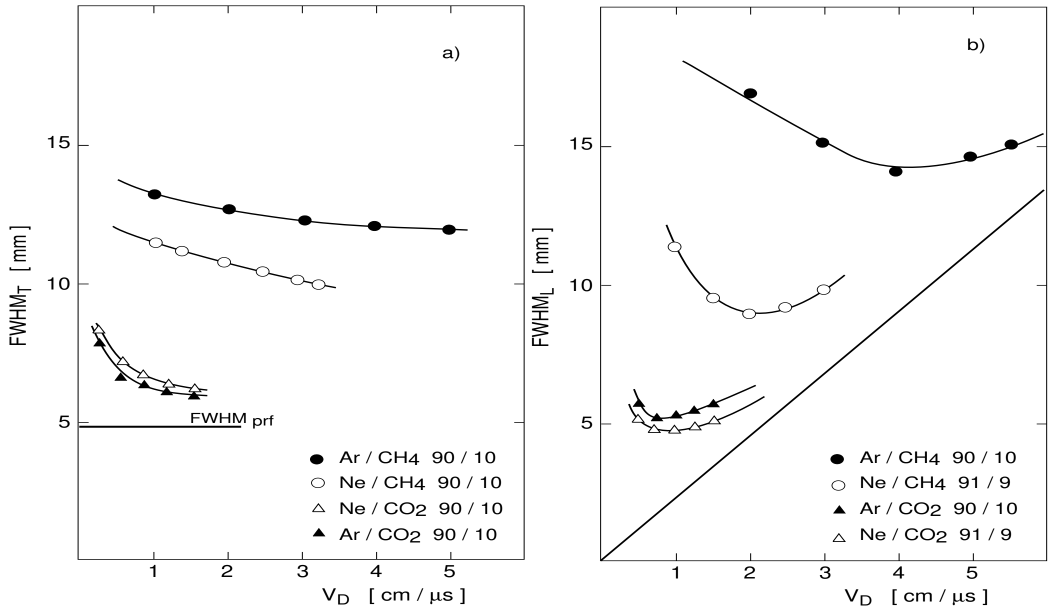

Figure 2.3 FWHM of charge distribution at $60cm$ drift length for different gas mixtures a) in transverse (bending plane) and b) in longitudinal (drift) direction. The limits are given by the pad response function and the electronics shaping time, are also indicated.

expected cluster width can be given by the following equation.

$$\sigma_x^2 = \sigma_{PRF}^2 + D_x^2 \cdot s + \frac{(l \cdot tan\alpha)^2}{12}, \tag{2.1}$$

σ_{PRF}	:	Sigma of the Pad Response Function.
D_x	:	Diffusion coefficient in transverse direction
s	:	Drift length
α	:	Track angle relative to the pads
l	:	Pad length

The width of the Pad Response Function (PRF) is a measure of the spatial extension of the signal induced on the cathode plane by a single electron. In the case of the MTPCs it is assumed to be of Gaussian shape, depending on the center of gravity of the charge distribution x and the position x_i of the i-th neighbouring pad:

$$P_i = C \cdot exp[-\frac{(x - x_i)^2}{2\sigma^2}]. \tag{2.2}$$

The influence of the angle α was minimized by rotating the pads to match the expected average particle trajectory. The width of clusters in drift direction σ_y can be parametrized by:

$$\sigma_y^2 = (T_{shaper} \cdot v_{drift}) + D_y^2 \cdot s + \frac{(l \cdot tan\lambda)^2}{12}, \tag{2.3}$$

T_{shaper}	:	Shaping time of the readout electronics
D_y	:	Diffusion coefficient in drift direction
s	:	Drift length
v_{drift}	:	Drift velocity
λ	:	Track angle relative to the readout plane
l	:	Pad length

The pad response function has to be replaced by the shaping time of the readout electronics. In analogy to α the angle λ reflects the angle between the particles trajectory and the readout plane. The final choice of gas was $Ne/CO_2(90/10)$ for the VTPCs and $Ar/CH_4/CO_2(90/5/5)$ for the MTPCs. The diffusion coefficients D_x,D_y have been measured to be 220 μm/$\sqrt{\text{cm}}$ and 270 μm/$\sqrt{\text{cm}}$ respectively, for the two gases, in both transverse and longitudinal direction. A detailed discussion of the drift processes of electrons in gases can be found in [44].
Drift fields of 200 V/cm (175 V/cm) correspond to drift velocities of 1.4 cm/μs (2.4 cm/μs) in the two types of detectors. In this range, drift velocities are unsaturated, i.e. they

change almost linearly with electric field. The exact measurement and control of drift velocity and its correction for pressure and temperature variations therefore becomes a key issue.
Another peculiarity of gas mixtures containing CO_2 is a relatively strong electron attachment in the presence of oxygen, which is more than one order of magnitude bigger than in the standard mixtures containing CH_4. We have measured attachment coefficients of 240 (120) per microsecond and atmosphere of oxygen, for the two gases quoted above revealing a linear dependence on the CO_2–content. This leads to attachment charge losses of 1.2% (0.6%) per ppm of Oxygen over the 50 μs drift time in the TPCs. Severe constraints on gas purity and leak rate have obviously to be imposed.
Attachment due to water contamination could not be observed up to water contents of several 100 *ppm*. The dependence of drift velocity on the water content is also relatively low, it has been measured to be -2% per 100 *ppm* H_2O.

The Readout Chambers

Due to the high track densities, pattern recognition of the charge information from the sense wires must fail because of multiple hits of single wires. Tracking and energy loss measurement therefore have to rely on the pad readout only. Fig. 2.4 gives a sketch of the readout units used in the NA49-TPCs. Seen from the drift space, a gating grid is followed by a Frisch grid closing the proportional chamber volume made up by 20 μm sense wires interspaced with 125 μm field (zero potential) wires. The signals are picked up by the back cathode plane which is subdivided into pads. Their dimensions are given in table 2.2.

dimensions [mm]	VTPC-1	VTPC-2	MTPC-L/R	wire material
pad/sense wire dist.	3	2	2, 3	
sense wire diam.	0.02	0.02	0.02	W-Re (gold plated)
sense wire spacing	4	4	4	
field wire diam.	0.125	0.125	0.125	Cu-Be (gold plated)
field wire spacing	4	4	4	
Frisch grid wire diam.	0.075	0.075	0.075	Cu-Be
Frisch grid wire spacing	1	1	1	
gating grid wire diam.	0.075	0.075	0.075	Cu-Be
gating grid wire spacing	1	1	2	

Table 2.2 Wire dimensions of the TPC readout chambers

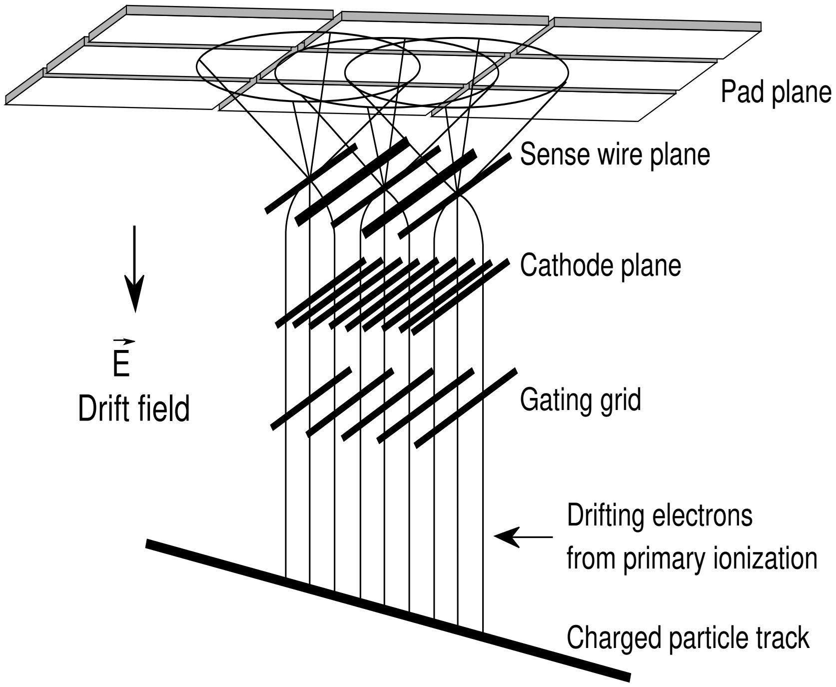

Figure 2.4 Schematic layout of the TPC readout chambers. Note that the drift is vertically upwards

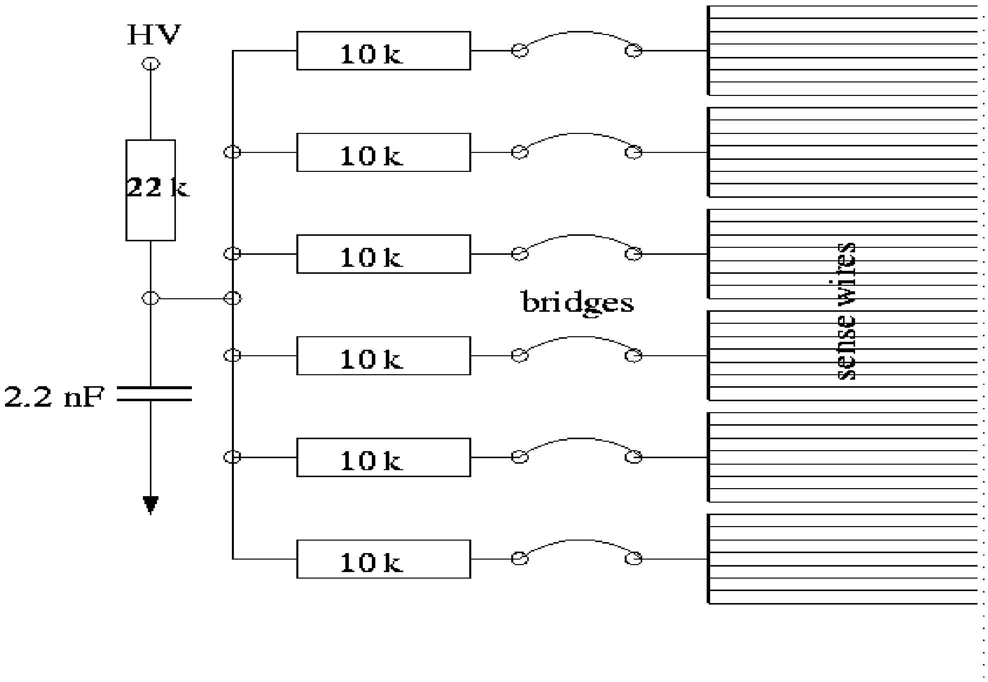

Figure 2.5 Sketch of the HV-supply of the sense wires

The sense wires of the proportional chamber are set to a potential of $\sim 1200V$. Fig. 2.5 shows a sketch of the high voltage supply of the sense wires. Note that the wires are divided into groups. Each group of 6 wires is connected by a common resistor to the high voltage supply.

The Front-End Electronics

The TPC readout system comprises a total of 182000 pads. The corresponding electronics system represents a complexity and channel density that can only be handled by making use of VLSI[1] full custom technology.
The design follows a readout structure first developed for the EOS experiment [34] and also adopted by the STAR collaboration [42]. Its function is based on a low event recording rate of 10-30 per SPS burst and on the absence of higher level trigger decisions requiring fast intermediate buffering. Efficient minimization of the number of components and a high degree of multiplexing are thereby possible even keeping in mind the very large raw data volume of 100 Mbyte per event. A detailed description of the electronics can be found in [41].
The complete front-end electronics is grouped on 32 channel cards which are connected to the corresponding pads on the back plane of the readout chambers. The main components are highly integrated into two types of custom designed chips: a 16 channel preamplifier/shaper and a 16 channel analog storage/analog-to-digital converter, both realized in CMOS technology [39].
The analog pad signal is time-sampled to 512 time buckets over the maximum drift time of 50 μs and stored in a Switched Capacitor Array (SCA) [40] which can be regarded as a series of 512 capacitors with a sample and hold circuit for each capacitor. After the readout cycle, the stored charges are digitized by the front-end electronics using a Wilkinson type ADC.

The typical pulse shape from a laser track in a MTPC is presented in Fig. 2.6. The signal shows a Gaussian shape, with a short-term undershoot of about 5% affecting the base line up to about 1 μs (corresponding to a space dimension of several cm) in the neighbourhood of each track (Fig. 2.6a). At larger times, the signal is followed by a complex overshoot/undershoot structure of the level of less than 0.5% (Fig. 2.6b). These features are connected to the principle of pad readout and are not taken out by the shaping stage since the necessary long time constants cannot be realized in VLSI techniques. As practically no positive ions arrive at the pad plane, the time integral over the signal has to be zero. Hence a negative undershoot occurs which starts at about 5 μs and continues beyond the TPC open time. In high track density environments,

[1] Very Large Scale Integration

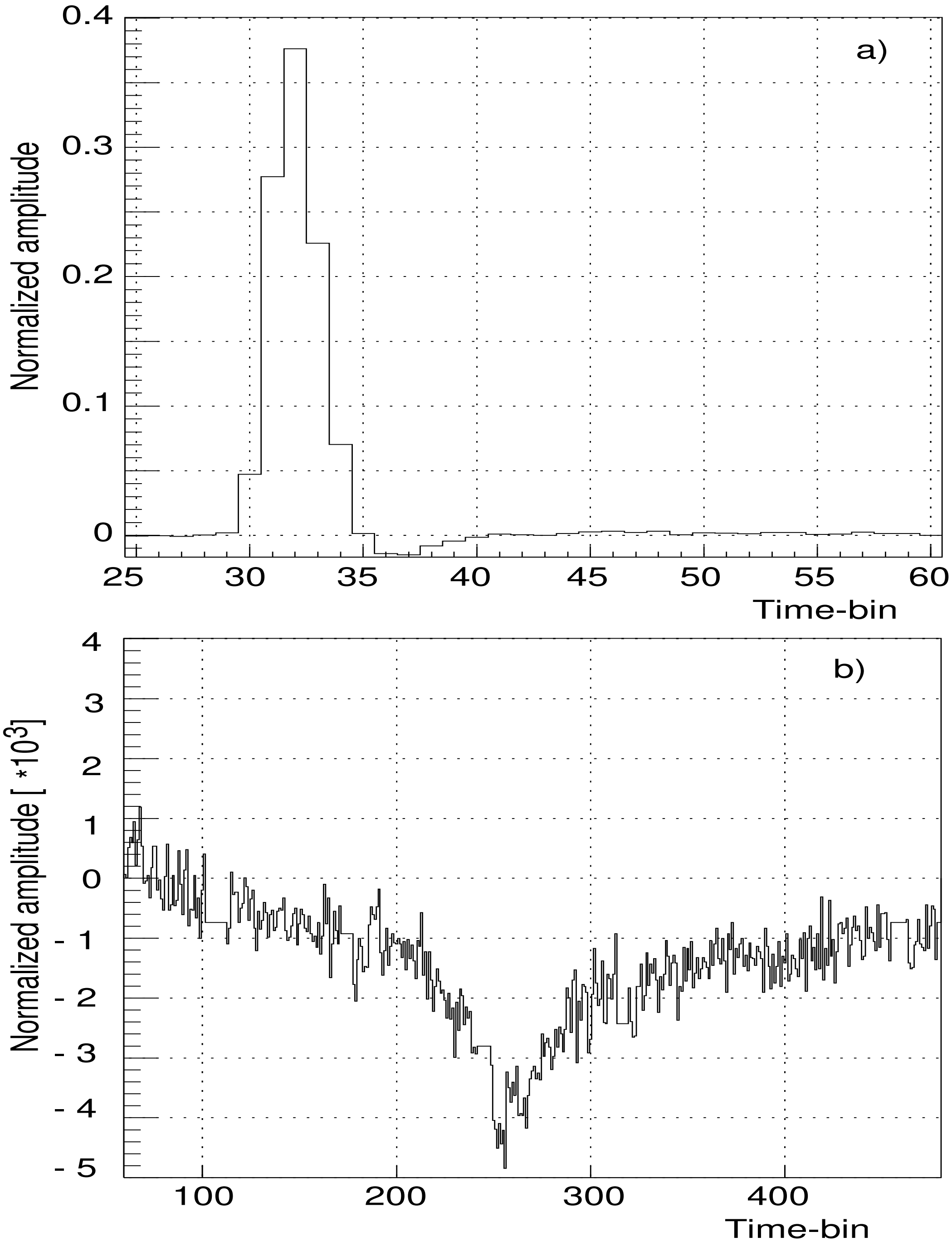

Figure 2.6 Time response of NA49 electronics a) for times up to $3\mu s$ b) for later drift times $5-50\mu s$. Note the difference in the vertical scales.

this undershoot results in a baseline shift due to tail superposition which looks like an effective charge loss as function of drift distance. In central Pb+Pb collisions this effect may reach several percent of the mean pulse height, thus affecting the quality of dE/dx determination. The off-line corrections developed in the framework of this thesis in order to correct for this effect will be introduced in chapter 4.4.
Another observation, again depending on track density, concerns changes of both channel gain and base line offset, which depends on the input charge load on each chip. This has to do with the difficulty of proper channel decoupling in a high component density VLSI environment. As a result, the apparent channel gain can vary by up to 10% depending on the pattern of the input charges on each chip, and on the chip position on the front-end cards. This precludes the possibility of performing electronics calibration using pulsing of the field wires, as in this case all channels of a full readout module are loaded simultaneously. Alternative methods of gain calibration had to be developed for the analysis presented in this thesis (see chapter 4.3).
The charge integrating stage of the preamplifier has a 12 bit dynamic range. In some instances this capacitor can saturate in the high track density areas of the detector leading to an abrupt loss of charge measurement for times beyond the saturation point on the affected channel.

Data Acquisition and Storage

The digitized information is transferred by flat ribbon cables to Control and Transfer boards also located on the TPC support plates. Here data are multiplexed and sent to the counting house on fibre optical links.
Receiver boards (3072 channels per board) mounted in a VME crate system perform digital data processing tasks including pedestal calculation and subtraction, zero suppression, noise rejection and event buffering, using Motorola DSP 96000 processors. In this stage the data volume is compressed to less than 10% of its raw volume such that one complete event corresponds to about 8 Mbyte of data for central Pb+Pb interactions. This is achieved by only recording data-pixels if two consecutive time bins of a given channel are above a fixed threshold and thus rejecting all time bins containing noise or zero information. In a high track-density environment this fixed threshold cut turned out to be problematic, because electronics deficiencies and properties of the readout chambers can lead to apparent baseline shifts for the charge measurement. Applying a fixed threshold cut to data with a changing baseline leads to systematic effects in the ionisation measurement. The methods developed to correct for this effect will be discussed in chapter 4.5.
The event rate is 25-30 per SPS burst (4.8 s for Pb-beam, 2.37 s for p-beam). After online data compression the events are written to a SONY DIR-1000M 19 mm tape

recorder which can operate at a transfer rate up to 16 MByte/s.

The Laser System

In order to assure the correct evaluation of all TPC operating parameters we need an internal reference.The NA49 Laser System was designed to provide well defined reference data inside the detector to gain information about its performance. This system is based on a pulsed Nd-YAG laser equipped with 2 frequency doublers and delivering a power of $4mJ$ per pulse at a wavelength of 266 nm. The laser beam can be directed with an automatic steering system towards any one of the four TPCs. There it is split and directed vertically down into the ceramic support tubes placed in the corners of the field cages. Auxiliary ceramic tubes inside these columns carry 6 beam splitters at 45 degree angle which reflect the UV light, through quartz windows, into the TPC drift volume. The auxiliary tubes can rotate in steps of 3 degrees driven by a pneumatic precision stepping mechanism. Beam positions are recorded and stabilized via position sensitive laser diodes (PSD) and autocollimation using steering with stepping motors and piezoelectric tripods. The schematic layout of one laser beam system is shown in Fig. 2.7a. Laser beams in up to 200 precisely defined positions can thus be produced, spanning the entire TPC volume.
The laser system has been successfully used in the study of tracking performance and all kinds of track distortions. In particular, it has been indispensible for the control of the large $E \times B$ distortions due to a inhomogenous magnetic field, and their correction. Residual distributions with respect to straight-line fits in horizontal coordinates are shown in Fig. 2.7 b, c, without and with the calculated $E \times B$ corrections. It has also given valuabale input to the understanding of the systematic effects of the ionization measurement, by providing a defined charge deposition in order to study the response of the readout electronics.

2.3 The Trigger System

The NA49 detector is located in the H2 beam line of the North experimental hall of the SPS. This line transports a fraction of the extracted heavy ion beam or a variety of secondary beams produced from primary protons to the experiment. A set of upstream scintillation or Čerenkov counters and beam position detectors, see Fig. 2.1, provides precise timing reference, charge and position measurement of the incoming beam particles.
In order to select events at a trigger level of a few percent of central interactions, the energy flux remaining in forward direction is measured by a Veto Calorimeter (VCAL

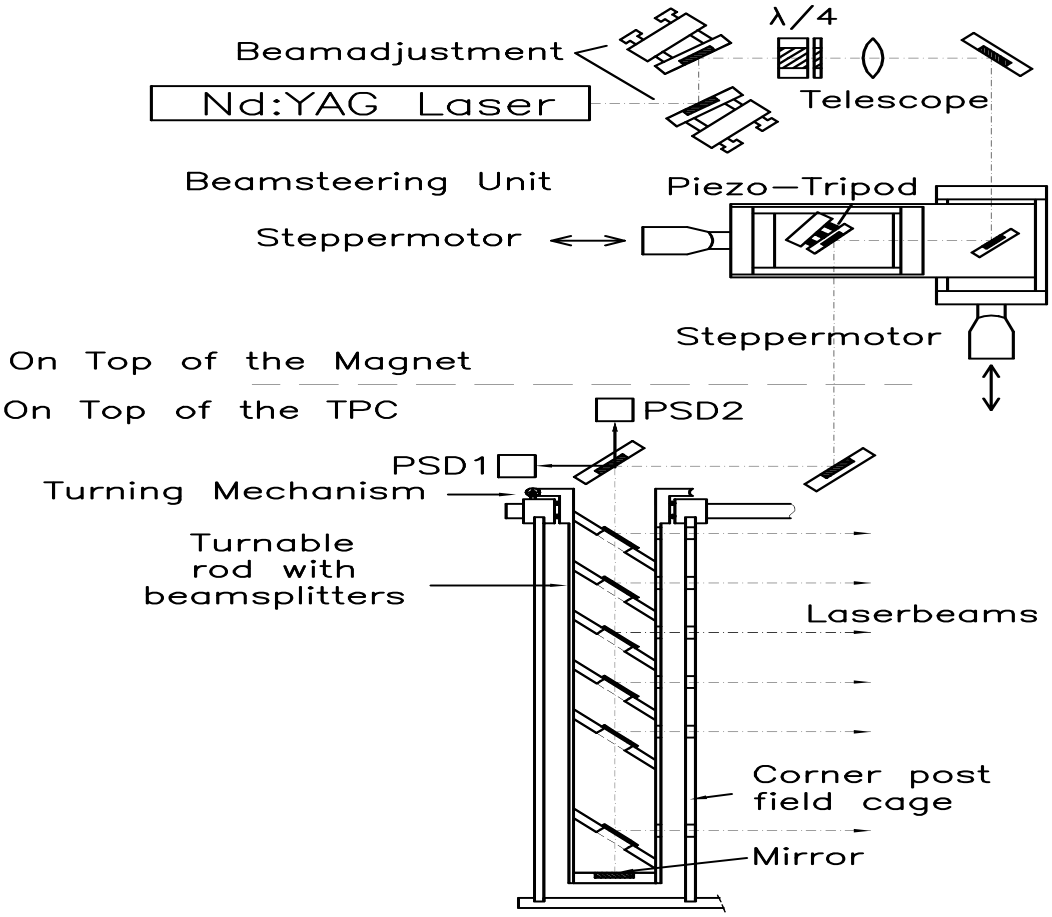

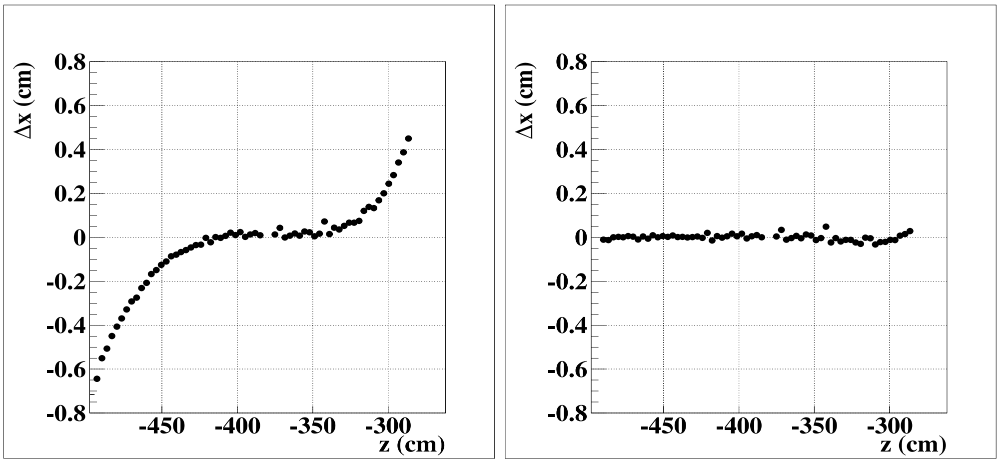

Figure 2.7 Optical layout of the Laser system of one TPC (Top Panel).
Residual distribution with respect to a linear fit to laser tracks in the bending plane without (Lower Left Panel) and with (Lower Right Panel) $E \times B$ correction.

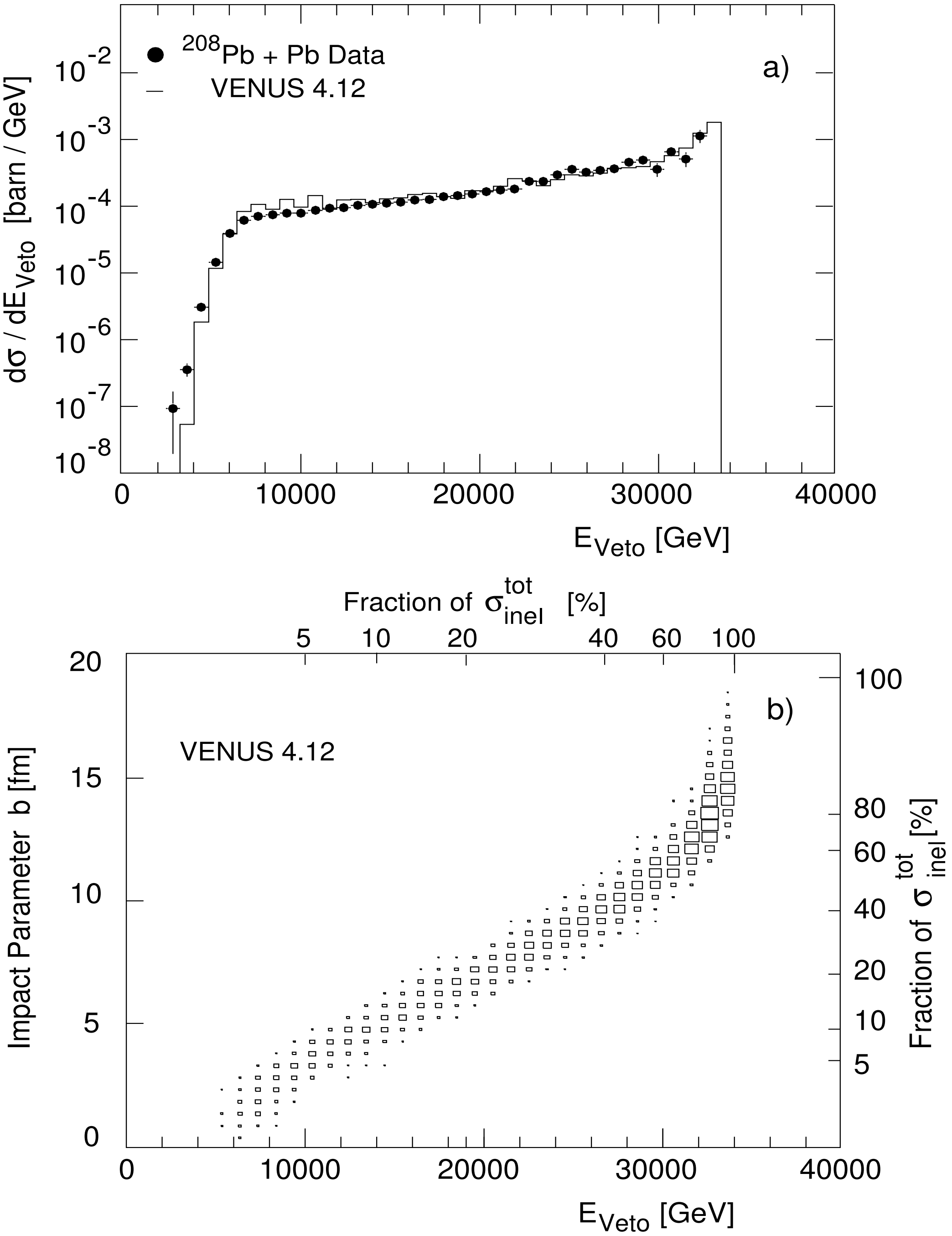

Figure 2.8 Energy spectrum of Veto Calorimeter in Pb+Pb interactions.

in Fig. 2.1) placed about 20m downstream from the target behind a collimator. The opening of the collimator is adjusted such that beam particles, projectile fragments and spectator neutrons and protons can reach the calorimeter.
The Veto Calorimeter, constructed originally for the NA5 experiment [54], consists of a lead/scintillator section of 16 radiation lengths followed by an iron/scintillator section of 7.5 interaction lengths.
The energy resolution can be parametrized by $\sigma(E)/E = 1.0/\sqrt{(E(\mathrm{GeV}))}$. Fig. 2.8a displays the energy spectrum observed in Pb+Pb collisions at 158 AGeV [55]. Discriminating the analog energy sum signal thus allows a selection on the centrality of the observed collision. A typical threshold setting at $E_{veto} \leq 10$ TeV corresponds to about 5% of the Pb+Pb interaction cross section and an impact parameter below 3.5 fm as illustrated in Fig. 2.8b.

2.4 Coordinate Systems, Variables and Definitions

Coordinate Systems

The *NA49 coordinate system* in which the particles trajectories and momenta are measured (see Fig. 2.9) is defined by the beam axis and the drift direction of electrons in the drift field of the TPCs. The nominal beam axis represents the z-axis of the coordinate system, the y-axis is defined by the drift direction. The x-axis is chosen perpendicular and also represents the bending direction of the magnetic field in a right handed coordinate system.
The raw data of the TPCs however is coded in the hardware coordinate system, defined by the layout of the detectors and the data acquisition system. The segmented cathode planes of the TPCs are parallel to the x-z plane, thus each pad corresponds to a x-z coordinate. Its position within detector setup is decoded by TPC number, sector number, pad-row number and position within a pad-row. The pad-rows are ordered along the z-axis, pads along the x-axis. The drift time of signals in a given channel is subdivided in 512 time bins, thus the time bin number corresponds to the y-coordinate. Table 2.3 gives summary of the number of pads, pad-rows and sectors per TPC.

	VTPC-1	VTPC-2	MTPC
number of sectors	6	6	25
number of pad-rows	72	72	90
pad-rows per sector	24	24	18
pads per pad-row	192	192	192 (HR) 128 (SR)

Table 2.3 some numbers concerning the readout planes of the TPC system.

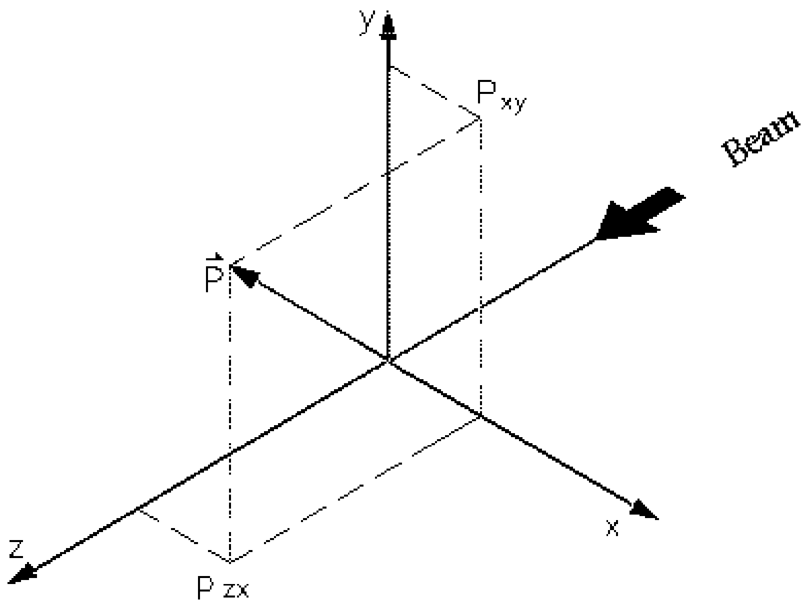

Figure 2.9 The NA49 Coordinate System.

Fig. 2.10 gives a sketch of location and numbering of the sectors in the NA49-Setup.
A detailed description of the algorithms used for transformation from the hardware to the NA49 coordinate system can be found in [56][57][58].
To make the understanding of the later chapters easier it is necessary to establish some terminology first:

- Pad planes. Plane in pad and time direction at a fixed pad-row.

- Time planes. Plane in pad-row and pad direction at a fixed time bin.

- Sector rows. Consecutive sectors in z direction.

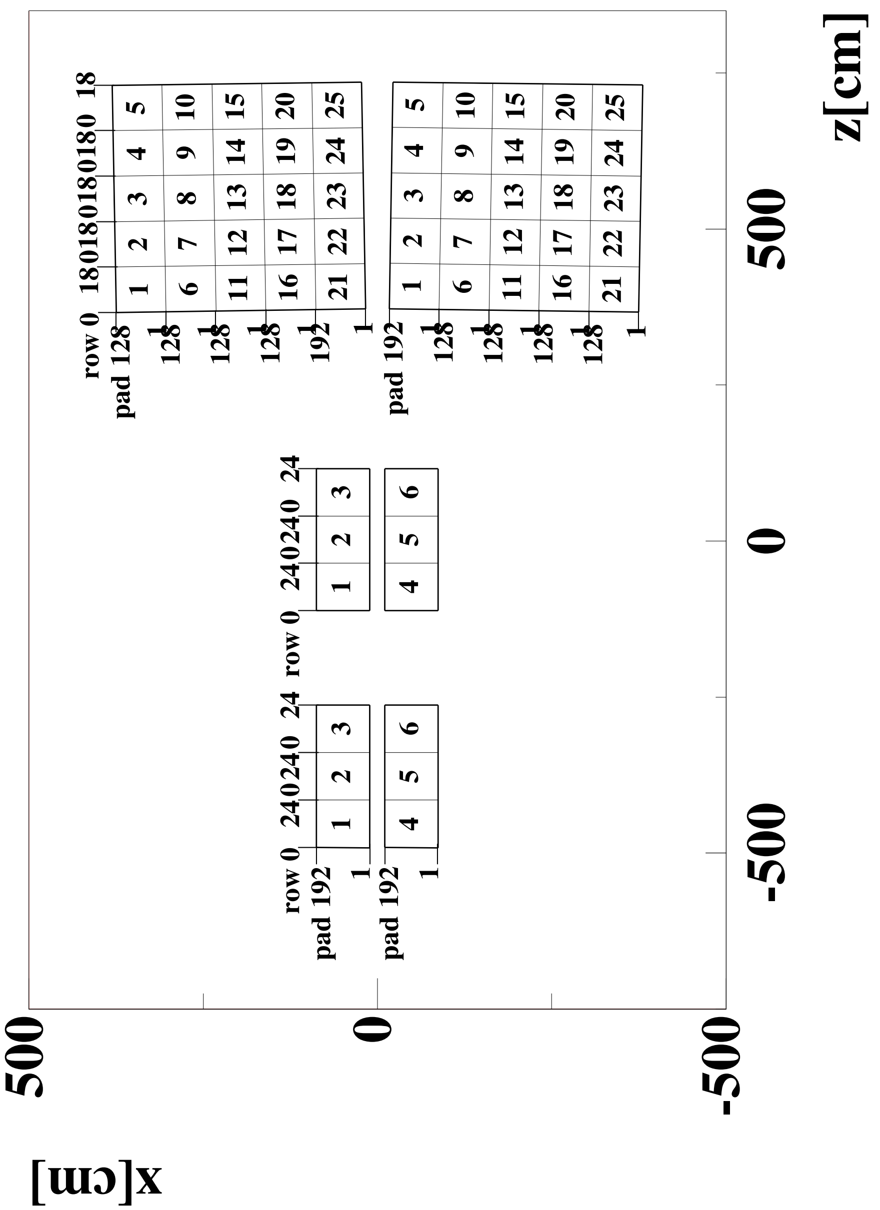

Figure 2.10 Numbering conventions of pads, pad-rows and sectors of the NA49 TPCs.

Choice of Variables

The phase space of the particles produced in a heavy ion collision is defined by the three components of the particles momenta p_x, p_y, p_z with p_z being the momentum component in beam direction. Owing to the azimuthal symmetry of central events the momentum components perpendicular to the beam axis are substituted by the **transverse momentum** p_T (equ. 2.4) and the azimuthal angle Φ.(equ. 2.5):

$$p_T = \sqrt{p_x^2 + p_y^2} \tag{2.4}$$

$$\Phi = \arctan p_y/p_x \tag{2.5}$$

The transverse momentum is invariant under Lorenz transformations in beam direction, e.g. transformations from the laboratory frame to the center of mass frame of the collision. This is not the case for the momentum component p_z in the beam direction. Thus for this degree of freedom a different variable, i.e. **rapidity** y is chosen which allows for a simpler transformation behaviour.

$$y = \tanh^{-1}\beta \quad \text{with} \quad \beta = v_z/c \tag{2.6}$$

Rapidity, as defined in equation 2.6, is a measure for the longitudinal velocity of a particle. A longitudinal Lorenz transformation is represented by a constant shift along the rapidity axis. Given the mass m and the total energy E of a particle,

$$E = \sqrt{p_x^2 + p_y^2 + p_z^2 + m^2} \tag{2.7}$$

the rapidity can also be expressed as:

$$y = \frac{1}{2} \cdot ln\left(\frac{E + p_z}{E - p_z}\right). \tag{2.8}$$

3 Analysis of TPC-Data

Starting from the raw data recorded by the data acquisition the NA49 reconstruction software faces the challenging task of reconstructing the trajectories of over 1000 charged particles by evaluating charge pixels measured by the TPC tracking devices. In order to make maximum use of the available information it is necessary to combine the data measured by the four local TPCs and treat the whole NA49 setup as one "global" detector system. The analysis software providing the unification of the detector system will thus be refered to as the "Global Tracking Chain".
This approach serves a twofold purpose: it combines the superior momentum determination of the vertex TPCs inside the magnetic field with the excellent particle identification capabilities of the large volume main TPCs and it also facilitates the pattern recognition by extrapolating tracks well separated in one detector to the high track density region of another.

3.1 The Global Tracking Scheme

The NA49 global tracking is based on a strategy of data reduction by first translating the hits in the detector into space points and then connecting these by pattern recognition algorithms. The space points are generated by identifying continous regions of charge pixels above threshold, so called "clusters", which are then connected to form "tracks". The algorithms used are set up to search for tracks originating from the vertex first, because they offer the best constraints for momentum reconstruction and are thus easiest to find. Removing the easy and well defined tracks from the sample leaves a moderate multiplicity of special cases. The order of the pattern recognition steps are given by the general properties of the different detectors.
The MTPCs have a simple track model (straight-lines) which facilitates pattern recognition, but only tracks originating from the vertex can be assigned a momentum that defines a unique trajectory, due to the absence of a magnetic field in the detector.

The VTPCs on the other hand have a good momentum resolution independent of the vertex because of the direct measurement of the track curvature, but suffer from a high track density and a complex track model of a helix distorted by inhomogenities in the magnetic field.
Combining these constraints with the idea to get predictions from the well defined tracks in one TPC into another part of the detector results in the procedure as follows:

- Cluster search in all four detectors.
- Straight tracks are reconstructed in the MTPCs.
- Vertex tracks are identified in the MTPC track sample and get a momentum assigned.
- MTPC vertex tracks are extrapolated to VTPC2 and clusters are collected along these predictions.
- Clusters from tracks in MTPC with predicted but not identified match in VTPC2 or from MTPC tracks which could not be extrapolated are set free.
- All remaining tracks are reconstructed in VTPC2.
- New VTPC2 tracks are extrapolated to MTPC and clusters are collected along these predictions.
- VTPC2 and MTPC tracks are extrapolated to VTPC1 and clusters are collected along these predictions.
- Clusters from tracks in MTPC with predicted but not identified match in VTPC1 are set free.
- All remaining tracks are reconstructed in VTPC1.
- New VTPC1 tracks are extrapolated to MTPC and clusters are collected along these predictions.
- All remaining (also special kink) tracks are searched in MTPCs.

This rather complicated approach subsequently identifies the clean and easy patterns and removes them from the sample to make the more complicated patterns emerge which then can be identified reliably. At the same time it provides a matching between the detectors.

The Software Packages

The main algorithms of this tracking scheme are listed below. The parts relevant to the analysis presented in this thesis will be described in more detail in the later chapters.

- clusterfinder (DIPT)
- local trackers (MTRAC, PATREC)
- momentum fitting (MTRAC, R3D)
- track extrapolation and matching (MPAT)
- helper clients (distortion clients, dE/dx clients, etc.)

The Cluster Finder

The cluster finder generates space points from the charge pixels in the TPC. The zero-suppressed raw data of all TPCs is expanded pad-row wise and searched for connected areas of charge in the pad-time plane. The cluster finder employs a so called chain code, i.e. for each pixel above threshold, the 4 next neighbours are added to a list if they are above threshold and are not already in the list. This list is followed until no more new pixels are found. The selected connected areas are then searched for maxima using a converging center-of-gravity algorithm which effectively "walks uphill". The found maxima define the cluster positions that are handed over to the tracking algorithms. Two merged clusters resulting in a single connected area of measured charge can only be resolved into two space points if at least two distinct maxima can be identified and are separated in the pad-time plane by a minimal distance of 3 pixels.

The Local Tracking

The local tracking in the different TPCs is performed by rather simple follow-your-nose trackers that step through the pad-rows and collect points fitting the given track model. In the MTPCs (no magnetic field) a straight line model is applicable. In case of the VTPCs inside the magnets the tracking relies on a helix model. Due to inhomogenities of the magnetic field a helix model does not fit the actually observed tracks in the outer regions of the detector very well, which made compromises in the choice of tracking tolerances necessary. In combination with the global tracking scheme which takes out most of the vertex tracks before the local VTPC-tracking is invoked this simple track model was found to give reliable results. Tracks found in the local tracking step will be called "local tracks" in the following chapters.

The Track Matching

The philosophy of how to combine the information of the local trackers is to provide - starting from an identified local track in one TPC - pseudo-points in the other TPCs traversed by this track. This is achieved by extrapolating this track over the whole length of the experiment, using the TRKSTEP package [60]. The resulting pseudo-points can then be used to collect points along the predicted road and thus create tracks. This method - especially in regions of high track densities - is much easier and faster than a follow-your-nose tracking approach. In the VTPCs these pseudo-points are provided every 4 cm, in the field-free MTPCs 2 points at entry and exit suffice. The tracks generated in the track matching step will be referred to as "global tracks". This approach relies on a precise knowledge of the detector geometry and alignment. Detailed information on the method and precision of detector alignment can be found in [31][56][57][58].

3.2 The Quality Assurance

Correlation measurements in a high track density environment demand a very robust tracking algorithm. As it turned out in previous analysis (e.g. [59]) a big source of systematic errors in any correlation measurement is the multiple detection of a single particle in different parts of the detector system. A close inspection of the NA49 data reconstruction software revealed that a non-negligible number of tracks in each event were found to be split into two or more parts due to inefficiencies in the pattern recognition algorithm. The splitting of tracks leads to track pairs that are close in momentum space. Fig. 3.1 shows the 4-momentum difference Q_{inv} of track pairs within single events with and without split track recognition.

$$Q_{inv} = \sqrt{(E_1 - E_2)^2 - (\mathbf{p}_1 - \mathbf{p}_2)^2} \tag{3.1}$$

The unphysical enhancement of track pairs in the vicinity of $Q_{inv} = 0$ fakes an effect of correlated particle production. The following chapter describes the methods developed within the framework of this thesis of merging or rejecting split tracks in order to protect correlation measurements from artefacts caused by the pattern recognition.
To identify and merge split tracks and evaluate the quality of a given track three measures are calculated:

- The number of potential points.
- The average geometrical distance to the closest of all other tracks.
- The 4-momentum difference Q_{inv} (as defined in equation 3.1) to the closest of all others tracks.

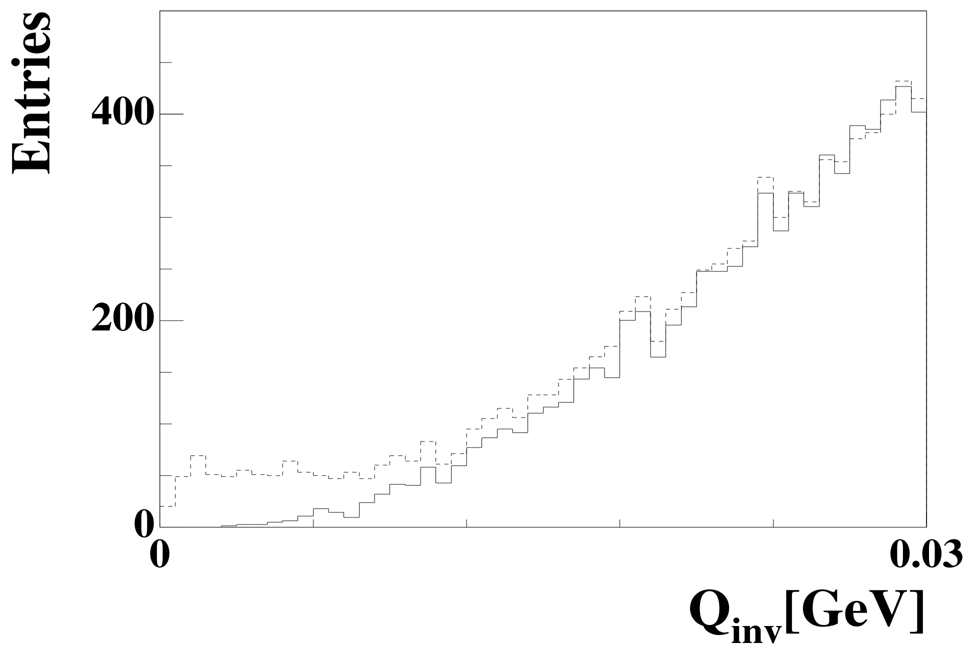

Figure 3.1 Q_{inv} Distributions for a track sample without split track recognition (dashed line) and for a track sample after merging of recognised splits and rejection of bad tracks (solid line).

The number of potential points is calculated by extrapolating each track to the z-coordinates of the padplanes of all TPCs and checking if the calculated x-y coordinates lie within the active volume of the detector. Fig. 3.2 shows the distribution of found and potential points in a sample of 10 central Pb+Pb events. The spikes in the potential point distribution reflect the number of pad-rows in the different TPCs, 72 for the vertex-TPCs, 90 for the main-TPCs and 162 for the combination of vertex-TPC 2 and the main-TPC. The shift of the found point distribution to lower numbers is due to the finite cluster finding efficiency. This effect is most prominent in vertex-TPC 1 only tracks, which have on average 45 potential and 25 found points.

Split Track Recognition

To identify split tracks it is necessary to test the hypothesis that two tracks are pieces of a single particle trajectory for every possible track pair of a given event. In central Pb+Pb events this results in a huge number of combinations and thus long computing time. Facing the task of reconstructing on the order of 10^6 events, computing time is a key issue in the choice of algorithms. Keeping this in mind the split track recognition program consists of a multi step process of reducing the number of combinations and

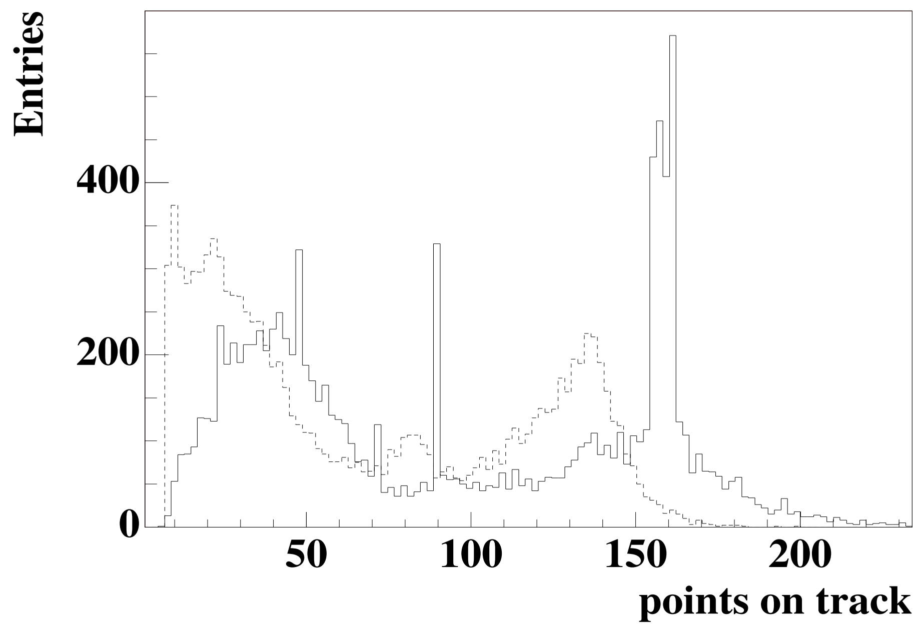

Figure 3.2 Number of found points (dashed line) and potential points (solid line) of global tracks

identifying split candidates first and then testing the candidates with more time consuming algorithms.

The following checks are performed to identify split candidates. Their order is given by the computing time:

1. More than 10 found points per track.

2. Both tracks must have a momentum assigned.

3. Both tracks must have the same charge sign.

4. the ratio of the sum of the found points on both tracks and the sum of their potential points must be smaller than 0.5.

5. Small 4-momentum difference Q_{inv} (typically $< 50 MeV$). The top panel of Fig. 3.3 shows the found to potential point ratio plotted against the Q_{inv} of the given track pair without the quality assurance client. The split track candidates show up in the lower half of the plot at small Q_{inv}.

6. The tracks must not overlap (i.e. have points on the same pad-row).

7. The track pair must be geometrically close. This is checked by extrapolating both tracks to the center of gravity of the z-coordinates of their combined points and by calculating the distance of the extrapolated trajectories in the pad-time plane.

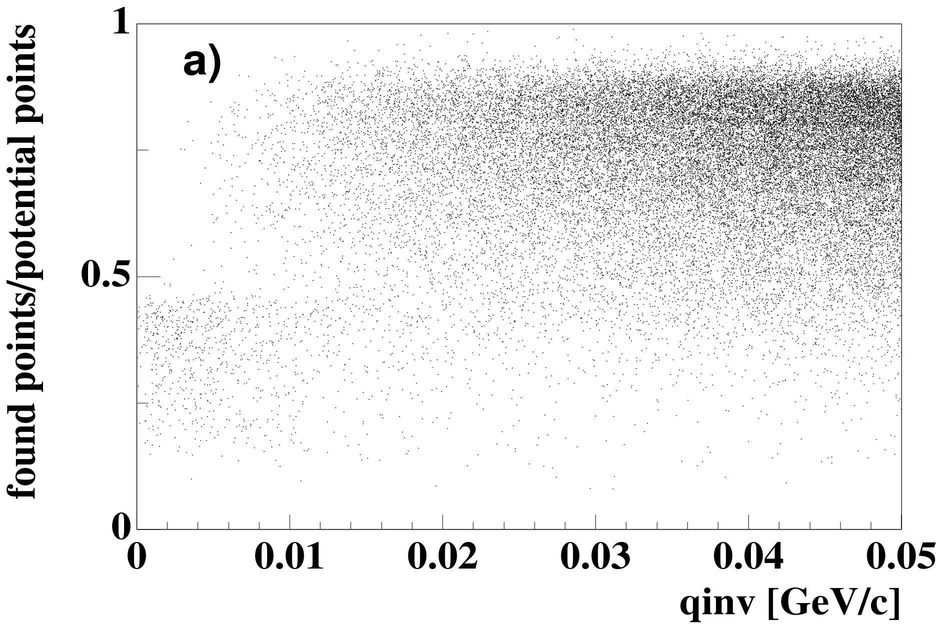

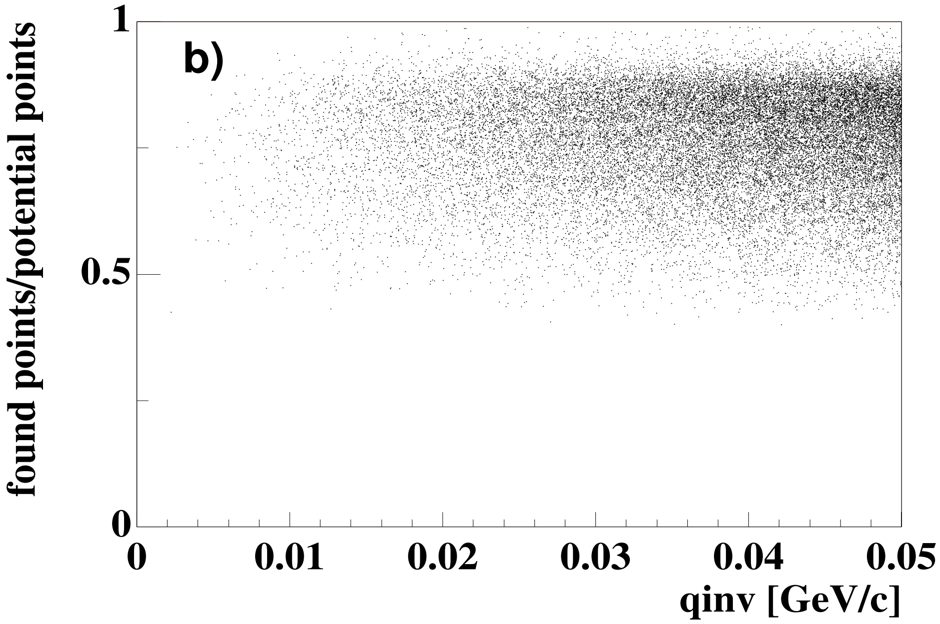

Figure 3.3 Sum of found points divided by the sum of potential points for a given track pair plotted against the four-momentum difference qinv. a) without split track recognition. b) with split track recognition.

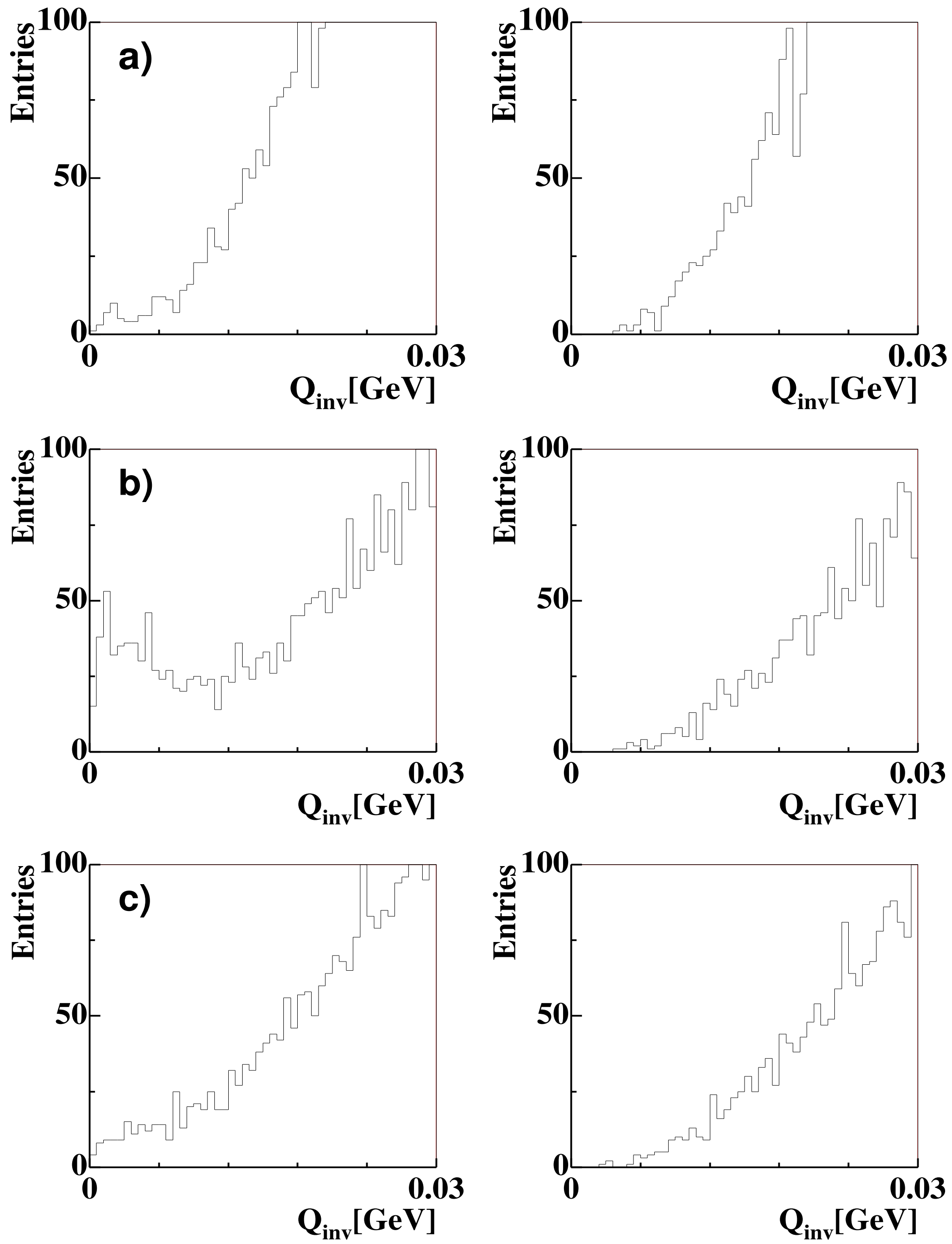

Figure 3.4 Q_{inv} distributions for different track samples taken from 100 central Pb+Pb events.
Left column: track sample without split track recognition.
Right column: Track sample after merging of recognised splits and rejection of bad tracks.
a) combinations of track pairs seen only in the same sub detector (local tracks)
b) combinations of tracks seen in vertex-TPC 1 and vertex-TPC 2.
c) combinations of tracks seen in only one vertex-TPC and a main-TPC.

The split track candidates are then tested by combining the points of the tracks and performing a momentum fit for the joined track. Then the average deviation of the points belonging to the input tracks from the trajectory fitted to the combined track is calculated. Only tracks for which the deviations of the points is consistent with the spatial resolution of the detector are merged. The bottom panel of Fig. 3.3 shows the found to potential point ratio plotted against the Q_{inv} after the track merging routines have been applied and bad tracks (see below) have been rejected. The fraction of merged tracks is given in table 3.1.
The top panel of Fig. 3.6 shows typical examples of split tracks. The Q_{inv} distributions for the corresponding track samples are shown in Fig. 3.4 The main reasons for split tracks are:

- The need for long extrapolation distances (cases 4 and 6, Q_{inv} distribution c.).

- Short tracks that have to be matched in areas of large uncertainties in the cluster position. Along the edges of the VTPCs the magnetic field is not parallel to the drift field, which results in large $E \times B$ distortions/corrections and less precision in the cluster position. In these regions the tracks also have a large crossing angle relative to the pads, which causes the cluster shape to deviate from the Gaussian shape assumed in the cluster finder and also results in a uncertainty of the cluster position (case 3, Q_{inv} distribution b.).

- In regions of low cluster finding efficiency like in the vertex-TPC 1 due to large track angles relative to the pads it can happen that too many consecutive clusters are missed, resulting in a gap which cannot be bridged by the pattern recognition algorithms (case 2, Q_{inv} distribution a.).

- High local track density can lead to the follow-your-nose tracker picking up points from a different track or points formed from noise clusters. The assignment of wrong clusters will then spoil the prediction in the next pad-row and cause the tracker to miss the rest of the track (case 5, Q_{inv} distribution a.).

The extrapolation routine used for the calculation of the potential points allows to identify two further classes of tracks that need to be excluded from the track sample:

- Spiral Tracks:
  In the extrapolation algorithm used for the potential point calculation tracks that reach a 90° angle with respect to the beam direction during the extrapolation back to the vertex are recognized. These tracks are often due to low momentum particles (mostly delta electrons) spiraling in the magnetic field of the VTPCs that are partially tracked by the pattern recognition. They get marked and will not be included in the data-analysis. Some typical examples of tracks identified as spirals are shown in the bottom panel of Fig. 3.6.

- Tracks without momentum:
  In some cases the momentum reconstruction algorithm fails and a track does not get a proper momentum assigned. Possible reasons for this are multiple scattering or kinks in the track due to the decays of the particle within the detector. Also the pick up of noise clusters or clusters belonging to a different track by the pattern recognition can cause the momentum reconstruction to fail. Conversions of γ-particles in the material of the detector housing into e^+e^--pairs is a further source of tracks that cannot be fitted. These tracks are especially frequent in the MTPCs.

The bottom panel of Fig. 3.7 shows the distribution of tracks without momentum in the detector system for a single central Pb+Pb event. As a reference the top panel of this figure shows the distribution of good vertex tracks, illustrating the track density in the different regions of the detector system.
Note that the need of reducing combinatorics for the split track recognition makes us heavily rely on the momentum assignment to the track pieces. If a piece does not get a momentum assigned it is not possible to merge the track. This is also problematic in the case of very short track pieces, because the uncertainty in the momentum assignment is a function of the number of points on track. The efficiency of merging short tracks is less than 100%. The short track pieces can be rejected by requiring a track to have more then 50% of its potential points found. Fig. 3.5 shows the ratio of found points and potential points on vertex tracks.

Table 3.1 gives a summary of the frequency of the special cases described above oc-

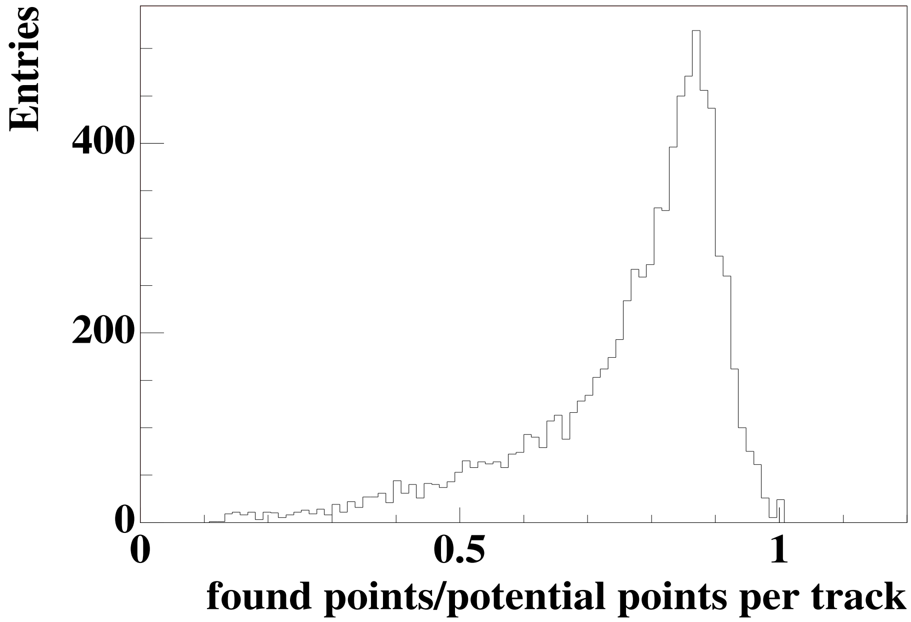

Figure 3.5 Ratio of found points to potential points of vertex tracks. An ideal detector would give a delta function at 1.

curring in central Pb+Pb events. Tracks identified as spurious by the measures of the quality assurance client have to be excluded from the track sample used for data analysis and have to be accounted for in the evaluation of the tracking efficiency.

selection	number/event	fraction
all	1678.4	100%
good	1248.1	74.36%
split	44.4	2.65%
spirals	25.2	1.50%
w/o momentum	360.7	21.49%

Table 3.1 Number of tracks found per event (central Pb+Pb) in the different track categories defined by the quality assurance client.

The evaluation of tracking efficiency is done differentially in small phase space bins because the effects described above may vary strongly in phase space. A detailed description of evaluation of tracking efficiency can be found in [62]. The analysis presented in the following chapters is restricted to tracks visible in the MTPCs because of the need of particle identification. For these tracks the tracking efficiency was found to be $95-100\%$ and since only ratios of particles will be considered no correction for the small inefficiency was done.

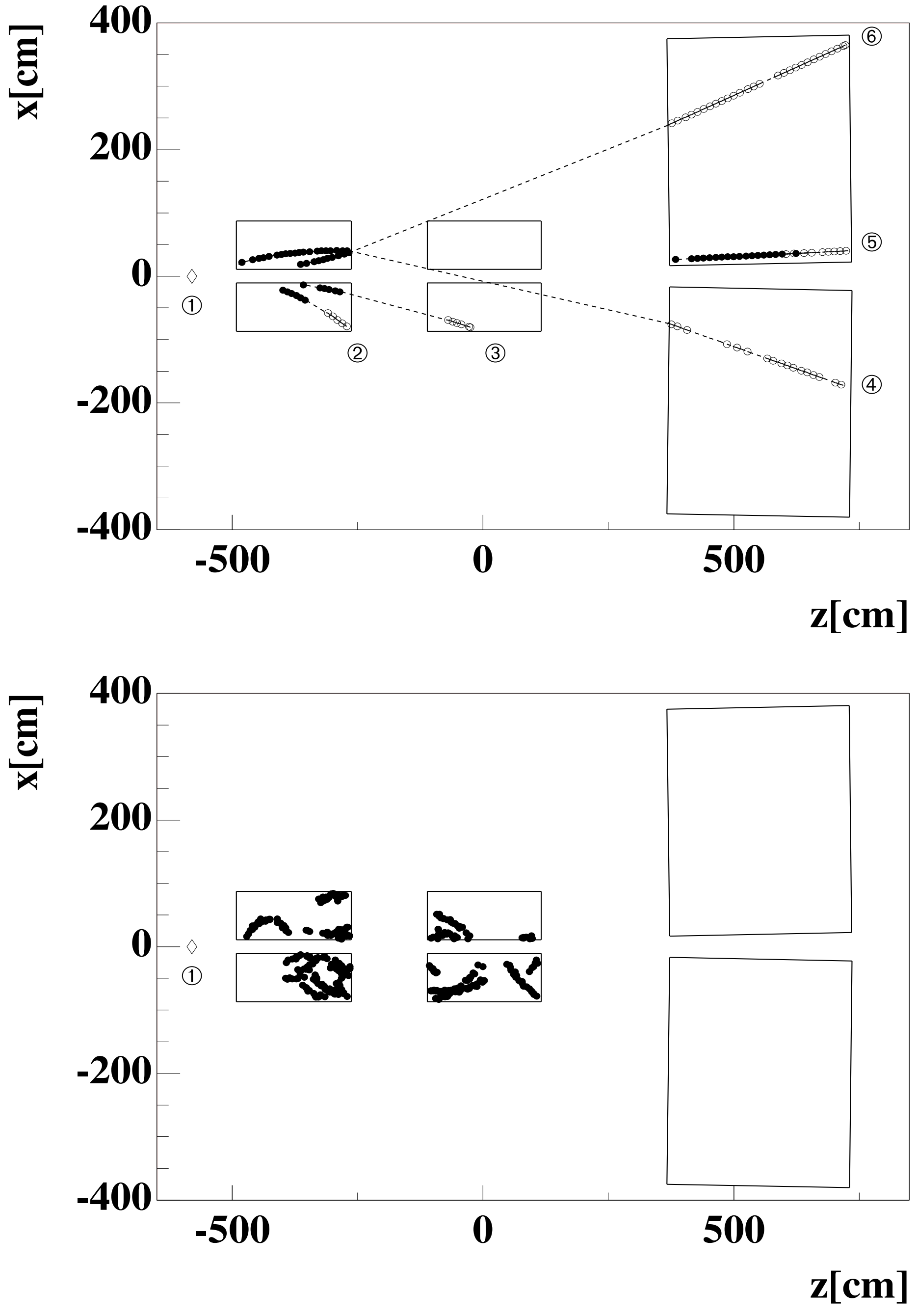

Figure 3.6 Track classes as identified by the quality assurance client.
Top panel: Split tracks.
Bottom panel: Spiral tracks.
1 indicates the target position.
The different cases of split tracks 2-6 are discussed in chapter 3.1.

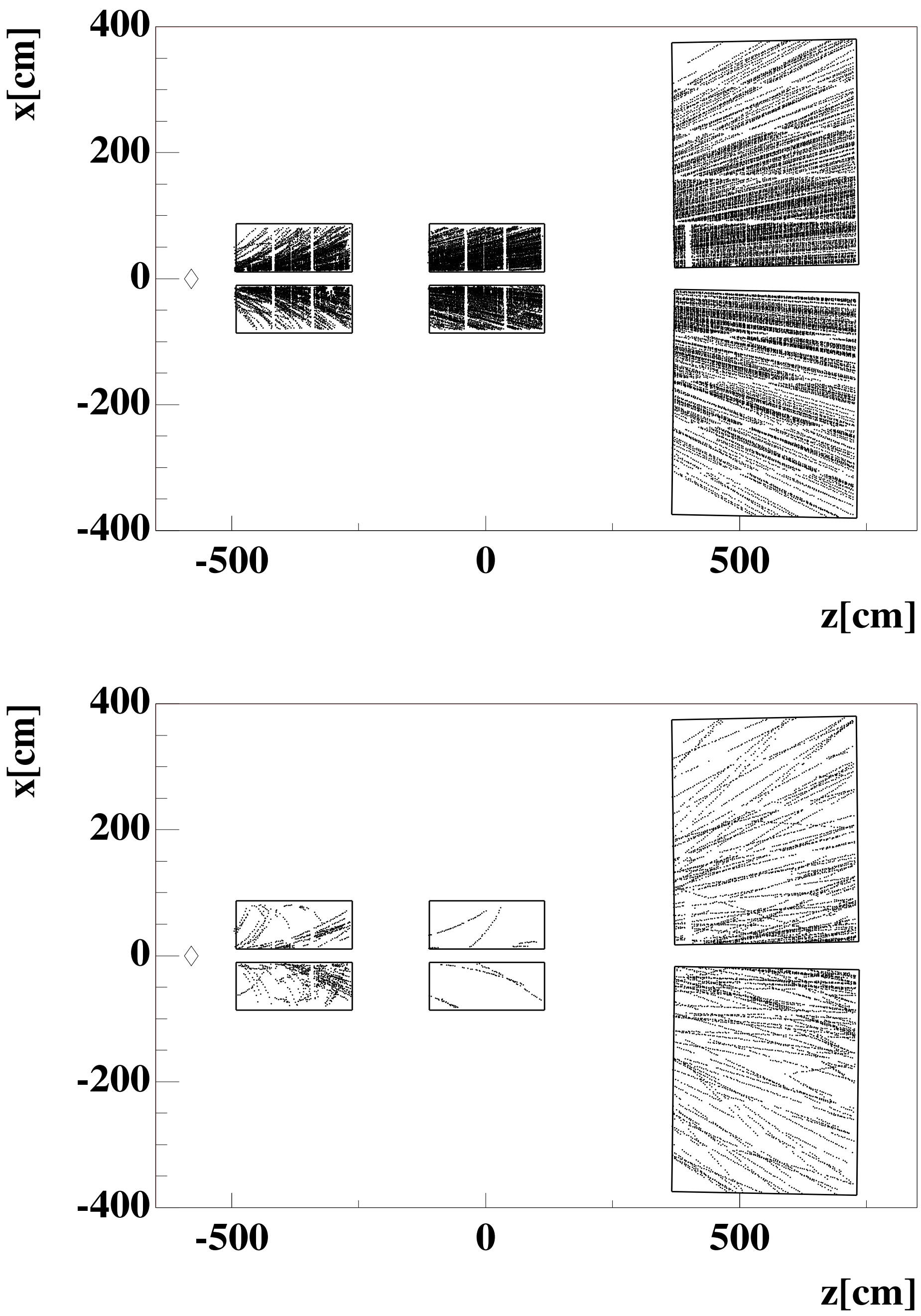

Figure 3.7 The top panel shows the geometrical distribution of vertex tracks of a single event that have enough points in the MTPC to be used for particle identification.
In the bottom panel the tracks of the same event are shown that fail the cuts ensuring track quality. This track sample consists mostly of tracks that can not be assigned to the main vertex and γ-conversions only visible in the MTPC.

4 Particle Identification

Given the laboratory momentum and the charge of a particle measured by the reconstruction of its trajectory in the magnetic field we need to determine its mass in order to identify the particle species. In the following chapter the mass determination by measurement of the specific ionization in the tracking detectors will be discussed.

4.1 The Bethe-Bloch Formula

A charged particle traversing the active volume of the detector ionizes the chamber gas by Coulomb interaction with the electrons of the gas molecules. Thus the particles leave a trace of free electrons and ions along their trajectory. The specific ionization of a charged particle is only a function of its velocity and its charge. In a magnetic spectrometer one measures the particle momentum through the curvature of its track in the magnetic field. An additional measurement of the ionization, i.e. the particles velocity, opens the possibility of determining the particle species. The relation between momentum p and velocity v involves the mass m:

$$v = \frac{c^2 p}{E} = \frac{c^2 p}{\sqrt{p^2c^2 + m^2c^4}} \tag{4.1}$$

where c is the velocity of light.
The mean differential energy loss dE per unit path length dx the particle suffers by ionization was first calculated by Bethe and Bloch for particles heavier than electrons ([63],[64]). Under the assumption of a cylindric electric field surrounding the incident particle, the momentum transfer on an electron by the transverse component of the electric field can be calculated. Integration over all energies lost to the individual atoms

of the medium then yields the so called **Bethe-Bloch Formula** (4.2):

$$\left\langle -\frac{dE}{dx} \right\rangle = \frac{4\pi N e^4}{mc^2\beta^2} z^2 \left(ln \frac{2mc^2\beta^2}{I(1-\beta^2)} - \beta^2 \right) . \tag{4.2}$$

With:

mc^2	:	rest energy of the electron
z	:	charge of incident particle
N	:	number density of electrons in the matter traversed
e	:	elementary charge
β	:	v/c of the incident particle
c	:	velocity of light
I	:	mean exitation potential

At non-relativistic energies, dE/dx is dominated by the overall $1/\beta^2$ factor and decreases with increasing velocity until about $v \approx 0.96c$, where a minimum is reached. Particles at this point are referred to as *minimum ionizing* particles. As the energy increases beyond this point, the term $1/\beta^2$ becomes almost constant and dE/dx rises due to the logarithmic dependence of 4.2.
Later it has been found that the relativistic rise would not continue to indefinitly large velocities ($\beta \to 1$). This fact was attributed to a coherent polarization of the surrounding atoms which thus shield the field of the travelling particle. Fermi [53] calculated a corresponding correction term $\delta(\beta)$ which is added to 4.2:

$$\left\langle -\frac{dE}{dx} \right\rangle = \frac{4\pi N e^4}{mc^2\beta^2} z^2 \left(ln \frac{2mc^2\beta^2}{I(1-\beta^2)} - \beta^2 - \delta(\beta) \right) . \tag{4.3}$$

Further it has to be taken into account that for the case of gas drift chambers equation 4.3 cannot describe the energy loss, because high energy transfers will result in an electron that is knocked out of the atom and will form a separate track. The ionization of this track can usually not be attributed to the first track. To reflect this a maximum momentum or energy transfer, the so called "cut-off"energy E_{max} has to be introduced into the calculation [49]. Energy transfers larger than the "cut-off"energy will not be regarded in the calculation. This then yields a measure called restricted energy loss:

$$\left\langle -\frac{dE}{dx} \right\rangle_{restricted} = \frac{4\pi N e^4}{mc^2\beta^2} z^2 \left(ln \sqrt{\frac{2mc^2 E_{max}\beta^2}{I(1-\beta^2)}} - \beta^2 - \delta(\beta) \right) . \tag{4.4}$$

In the limit $\beta \to 1$ the velocity dependence vanishes and the restricted energy loss reaches the *"Fermi plateau"*. This equation now also holds for electrons.
Since the analysis presented in the later chapters relies heavily on predictions of the

specific ionization of a particle given the measured momentum and a mass hypothesis it is necessary to measure and parametrize the shape of the Bethe-Bloch function as precisely as possible. The measurement is described in sections 4.2 and 4.3. As parametrization of the $\delta(\beta)$ term we use a description that was introduced by Sternheimer and Peierls[50]:

$$\begin{array}{lcll} \delta & = & 0 & \text{for} \quad X < X_0 \\ \delta & = & 2ln(10)(X - X_A) + a(X_1 - X)^m & \text{for} \quad X_0 < X < X_1 \\ \delta & = & 2ln(10)(X - X_A) & \text{for} \quad X_1 < X \end{array} \tag{4.5}$$

where $X = log_{10}(\beta\gamma)$. The exponent m was found to be 3 for all materials, the quantities X_A and a depend on the absorbing material. X_0 and X_1 result from the boundary condition that 4.4 should be a smooth function at $X = X_0$ and $X = X_1$. Instead of calculating the parameters from first principles, it was shown by Ambrus [51] that this model can also be fitted to experimental data by considering the parameters depending on the absorbing material as free fit parameters:

$$\left\langle -\frac{dE}{dx} \right\rangle_{restricted} = E_0 \frac{1}{\beta^2} \left(K + ln(\gamma^2) - \beta^2 - \delta(\beta, X_A, a) \right) \tag{4.6}$$

with $\delta(\beta, X_A, a)$ defined by eq.4.5. E_0, K, X_A and a are now the free parameters to be fitted to the data. E_0 contains all constant factors of the Bethe-Bloch-equation and determines the normalization of the curve. K adjusts the shape of the curve around the minimum. Also the parameters X_A and a calculated by Sternheimer and Peierls from properties of the medium are now fitted to the data, with X_A giving the magnitude of the relativistic rise and modelling the shape of the transition from the logarithmic rise to the plateau region. X_0 and X_1 can be calculated as follows:

$$\begin{array}{lcl} X_0 & = & X_A - \frac{1}{3}\sqrt{\frac{2ln(10)}{3a}} \\ X_1 & = & X_A + \frac{2}{3}\sqrt{\frac{2ln(10)}{3a}} \end{array}$$

Fig. 4.1 shows the shape of the Bethe-Bloch function parametrized by this method for different particle species plotted against their laboratory momentum.

4.2 dE/dx - Measurement

In a TPC usually the amount of ionization of the chamber gas by the charged particles is measured but not the energy loss. However one assumes a proportionality of these

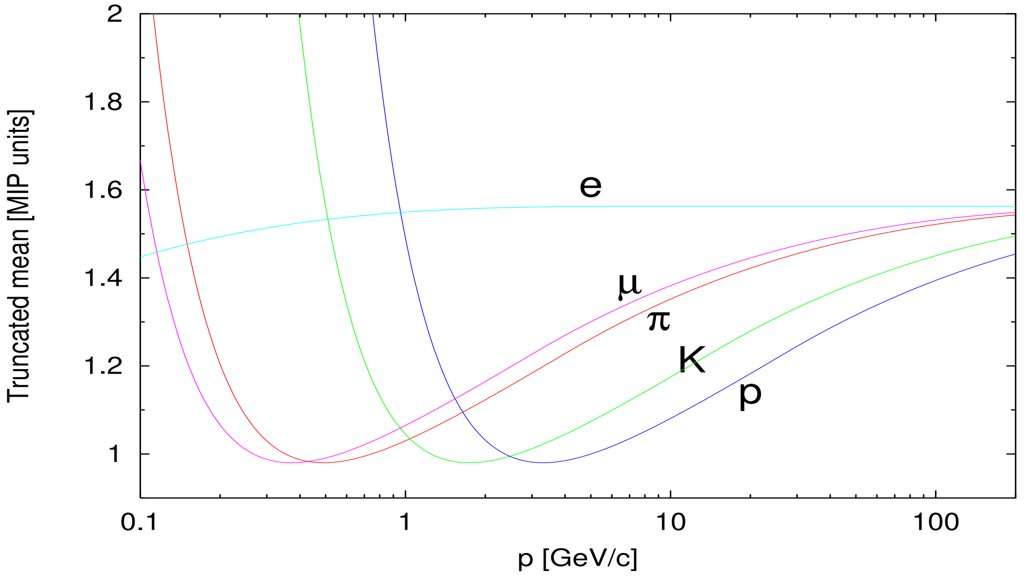

Figure 4.1 Bethe-Bloch functions for different particles. The transformation from $dE/dx(\beta\gamma) \rightarrow dE/dx(p)$ with $\beta\gamma = p/mc$ results in the separation of the different particle species according to their mass. The truncated mean is given in units of the ionization of a minimum ionizing particle [MIP].

measures and thus these measures will be treated as equivalent in the following chapters. Concerning the measurement of dE/dx one has to keep in mind that the energy loss of a particle is not a Gaussian distribution around its most probable value, but in the case of thin absorbers like gas layers in the TPC it follows a distribution that was calculated by Landau [52]:

$$f(\lambda) = \frac{1}{\sqrt{2\pi}} e^{-\frac{1}{2}(\lambda + e^{-\lambda})} \tag{4.7}$$

λ here denotes the deviation from the most probable energy loss $(\Delta)_{mp}$: normalized to the mean energy loss $\langle \Delta E \rangle$.

$$\lambda = \frac{\Delta E - (\Delta)_{mp}}{\langle \Delta E \rangle} \tag{4.8}$$

The tail to high energy losses accounts for the possibility of large energy tranfers by hard collisions with electrons of the gas molecules (δ-electrons). Fig. 4.2 shows a Landau distribution as it is observed in the main-TPCs.

To get a precise measurement of the ionization, it is sampled in small steps along the particle trajectory (e.g. on each pad-row of the TPC). The ionization is then estimated by an appropriate averaging procedure of the statistically independent samples.

Due to the tail of the energy loss distribution its characterization is not straight forward. A simple averaging of the samples is of course possible, but is, due to the large fluctuations of the ionization, not very precise. In case of a limited number of samples the precision can be increased by the *truncated mean* method. By rejecting the 35% highest samples of the ionization-distribution the asymmetric part of the Landau distribution is

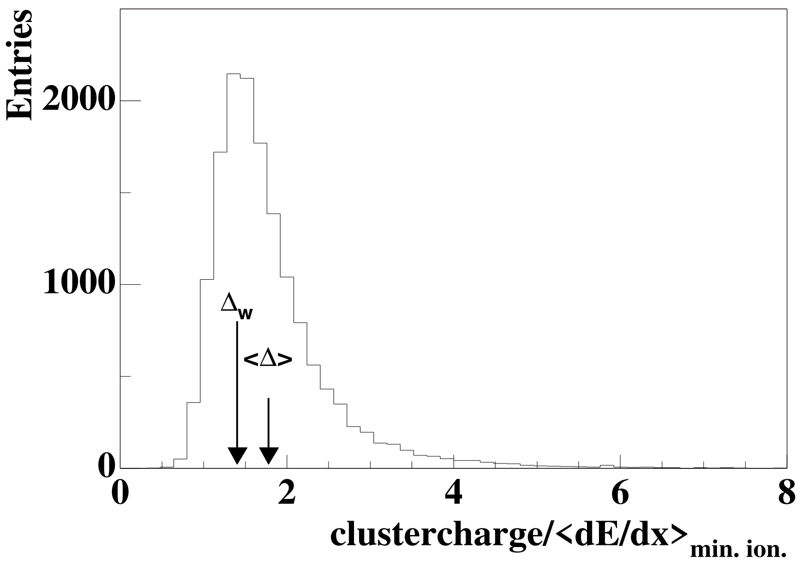

Figure 4.2 Energy loss distribution for particles (mostly π^-) of momentum $p \approx 8.5GeV/c$. The shape reflects a Landau-distribution of the energy loss in a thin absorber. The mean energy loss $\langle\Delta\rangle$ is shifted to high values and the most probable value Δ_w is indicated at the maximum of the distribution.

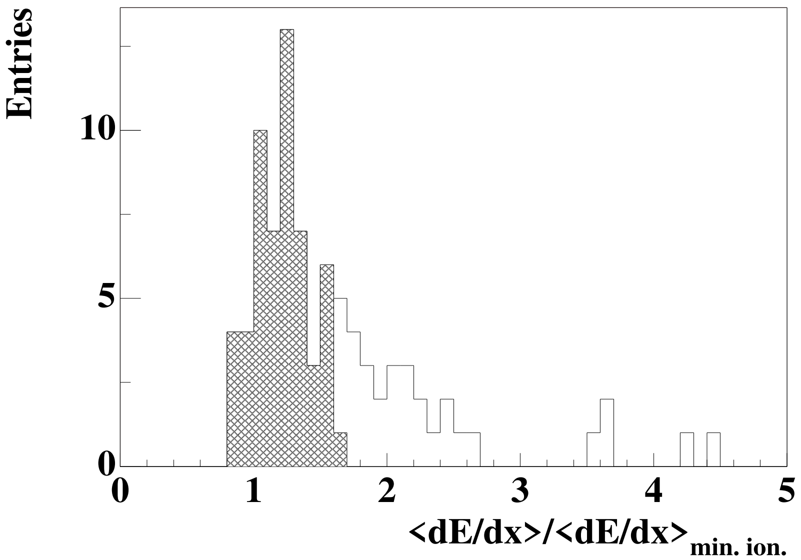

Figure 4.3 Distribution of ionization samples on one track. The shaded area illustrates the samples used for the calculation of the mean after truncation.

split from the Gaussian part. The most probable value of the Landau distribution can then be estimated by the mean of the Gaussian distribution remaining after truncation. Fig. 4.3 shows an example of the *truncated mean* procedure applied to a track consisting of 88 independent samples of the particles' ionization of the chamber gas. The shaded area represents the samples used for calculating the mean after truncation.

4.3 Calibration of the Ionization Measurement

The precision measurement of the specific energy loss and its use for particle identification was one of the principal goals of the NA49 tracking system. Due to the fixed target setup the momentum distribution of reconstructed tracks varies from a few hundred MeV/c up to 100 GeV/c. This measurement spans the full range of the energy loss function from the sub-relativistic $1/\beta^2$ dependence for kaons and protons through minimum ionization into the relativistic rise and up to the Fermi-plateau for pions and electrons. In order to achieve a good separation of the different particle species over the full range of measured momenta it is important to precisely calibrate the ionization measurement and to understand all systematic effects of the detector response.
The first part of the calibration procedure deals with the electronics and gas gain. This calibration is done in two steps. First the single channel electronics gains within each sector are calibrated by releasing a known number of electrons into the TPC drift space. Injection of radioactive ^{83}Kr gas can serve this purpose. This method has been developed by the ALEPH collaboration [65]. The second step is the relative calibration of the different sectors. This information cannot be obtained precisely enough from the krypton calibration since the sense wire voltages of the readout modules is different from the data taking modes in the krypton measurement. The energy deposition of a krypton decay is an order of magnitude higher than that of a minimum ionizing particle. A detailed description of the NA49 krypton calibration can be found in [31] and [46]. A novel method of inter-sector calibration has been developed in the framework of this thesis and will be presented in the following section.

Inter-Sector Calibration

A precise relative calibration of the response of each sector has been found to be the key ingredient for an optimal particle identification by the measurement of the specific ionization. This is due to the strong correlation between particle momenta and the positions of the various readout sectors, as illustrated in Fig. 4.4a. As a consequence a sector of a given TPC measures particles of a certain momentum range and thus probes only a limited range of the energy loss function, as shown in Fig.4.4b. A misalignment of the sector gains will result in a distorted shape of the energy loss function as illustrated in Fig. 4.5 which shows the ionization as a function of the particle momenta for uncalibrated MTPCs (top panel) compared to the calibrated MTPCs (bottom panel). The origin of the distorted shape shown for the uncalibrated TPCs is the choice of gas amplification in the readout chambers according to the dynamical range of the preamplifier/shaper units. A value of 75 ADC-counts for the mean maximum ADC value of clusters measured in a given sector type was found to be a good compromise between signal to noise ratio and use of the dynamical range. The top panel of Fig. 4.6 shows the mean maximum ADC values for the different sector types as measured with the gain settings of the '96 data taking period. Combining this with the average number of pads per cluster of ~ 3.5 for the standard resolution sectors and ~ 4.5 for the high resolution sectors one obtains the ionization distribution shown in Fig. 4.5.

Earlier attempts of inter-sector calibration in separate data taking runs (e.g. [46]) often failed to yield consistent results due to the operation of the detector system under different conditions in the calibration run compared to real data taking modes.
The new approach developed for the analysis presented in this thesis relies on particle data measured in production runs only. The philosophy is to first measure the shape of the Bethe-Bloch function and parametrize it as seen by the detectors and then adjust the sector gains so that the observed average energy loss of the measured particles matches the parametrization.

The measured ionization I_i of a given particle species i at a fixed value of total momentum p is determined by the gain A of the TPC-sectors it traverses and the Bethe-Bloch function which at a fixed momentum depends on the mass of the particle species i:

$$I_i = A \cdot \left\langle -\frac{dE}{dx} \right\rangle (m_i) \tag{4.9}$$

Looking at the ratio $r_{i,j}$ of the ionization measured for different particle species i, j at the same value of total momentum one sees that the sector gains cancel, since particles of the same momentum pass the same geometrical regions of the detector:

$$r_{i,j} = \frac{I_i}{I_j} = \frac{A \cdot \left\langle -\frac{dE}{dx} \right\rangle (m_i)}{A \cdot \left\langle -\frac{dE}{dx} \right\rangle (m_j)} \tag{4.10}$$

The value of the ratio will depend only on the shape of the Bethe-Bloch function. By measuring the ratio $r_{i,j}$ for all possible combinations of particle species over a large range of total momentum it is possible to measure the shape of the Bethe-Bloch function. Fig. 4.7 shows the ratios $r_{i,j}$ for electrons, kaons and protons relative to the ionization measured for pions as a function of total momentum. The values are obtained by unfolding dE/dx spectra generated from uncalibrated data in bins of total momentum. By calculating the corresponding ratios $r_{i,j}$ from the parametrization of the Bethe-Bloch function

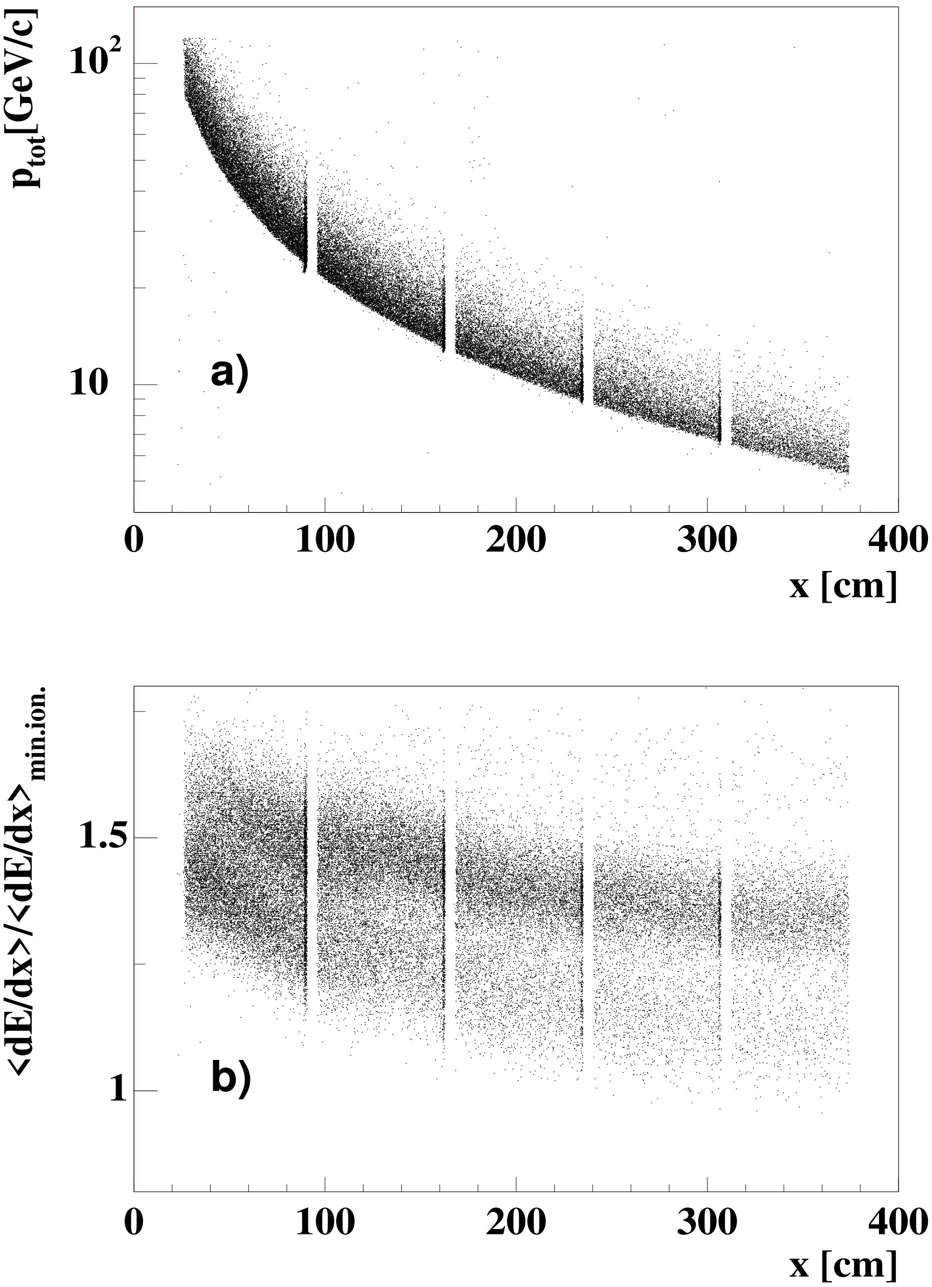

Figure 4.4 a) Dependence of momentum p_{tot} of a given track on the position x in the bending plane. The value of the x-coordinate is given by the position of the endpoint of the track in the MTPC.
b) Dependence of the measured ionization on the position x in the bending plane.
The gaps in the distributions reflect the gaps between the sectors of the main-TPC.

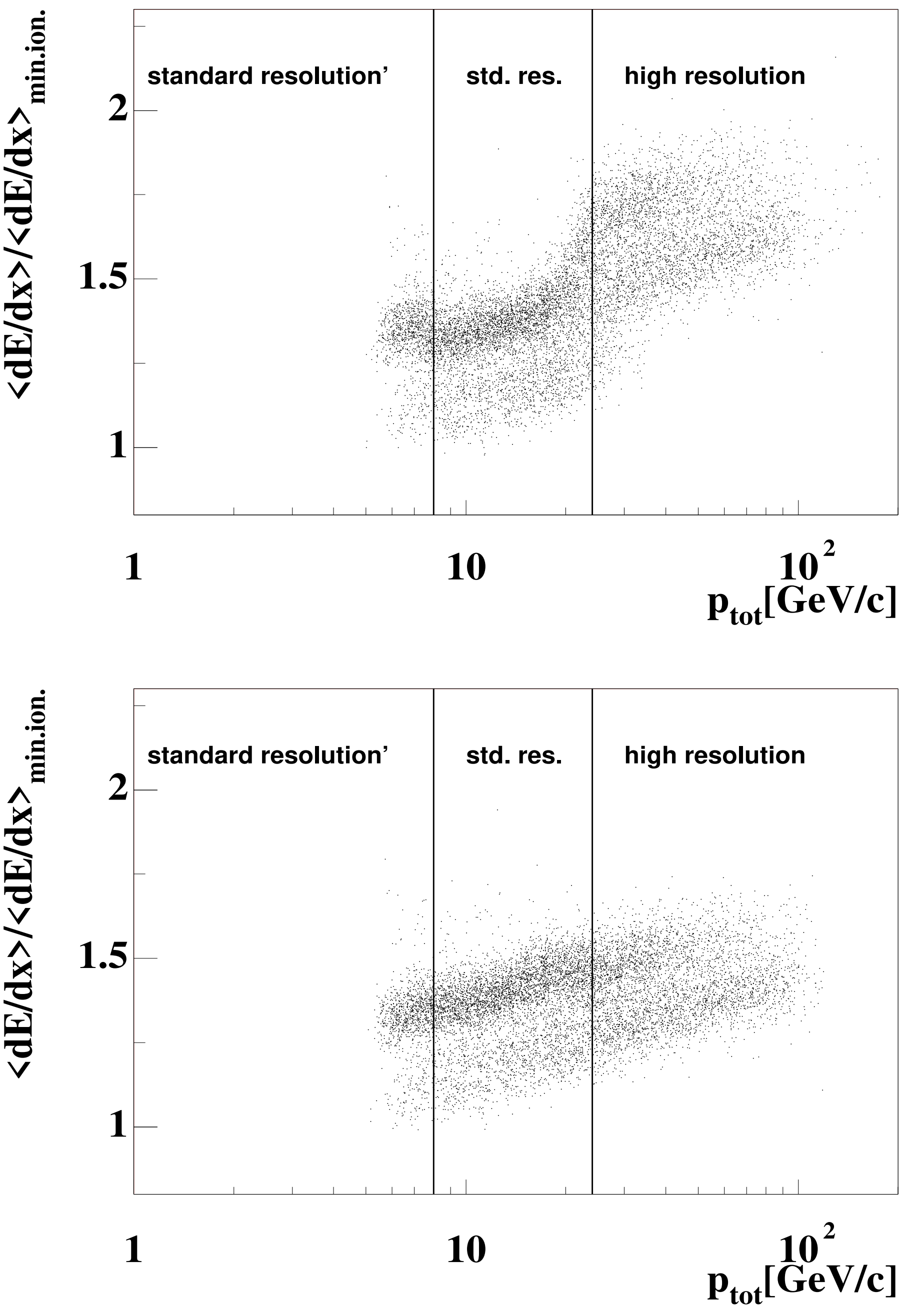

Figure 4.5 Ionization measurement plotted against the particles momentum for the uncalibrated TPCs (top panel) and the calibrated TPCs (bottom panel). The horizontal lines indicate the momentum ranges seen by the different sector types.

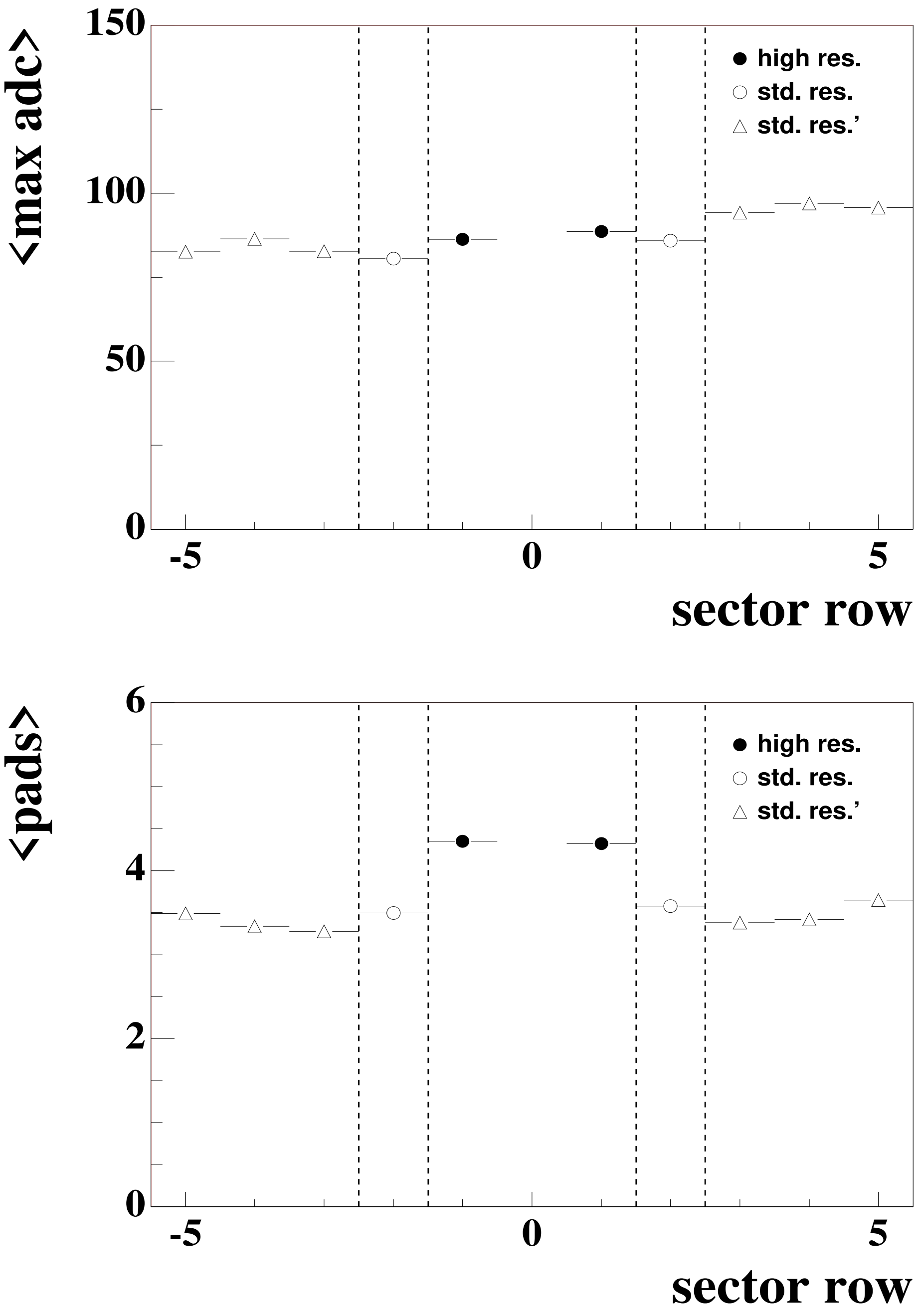

Figure 4.6 Properties of the clusters measured in the different sector types. The sector rows are numbered counting from the beamline. The innermost sectors (row -1,1) are of high resolution type (192 pads per pad-row). The outer sectors are of standard resolution (row -2,2) and standard resolution' type (row -5 - -3 and 3 - 5) consisting of 128 pads per pad-row each. Top panel: Mean maximum ADC per cluster. Bottom panel: Mean number of pads per cluster.

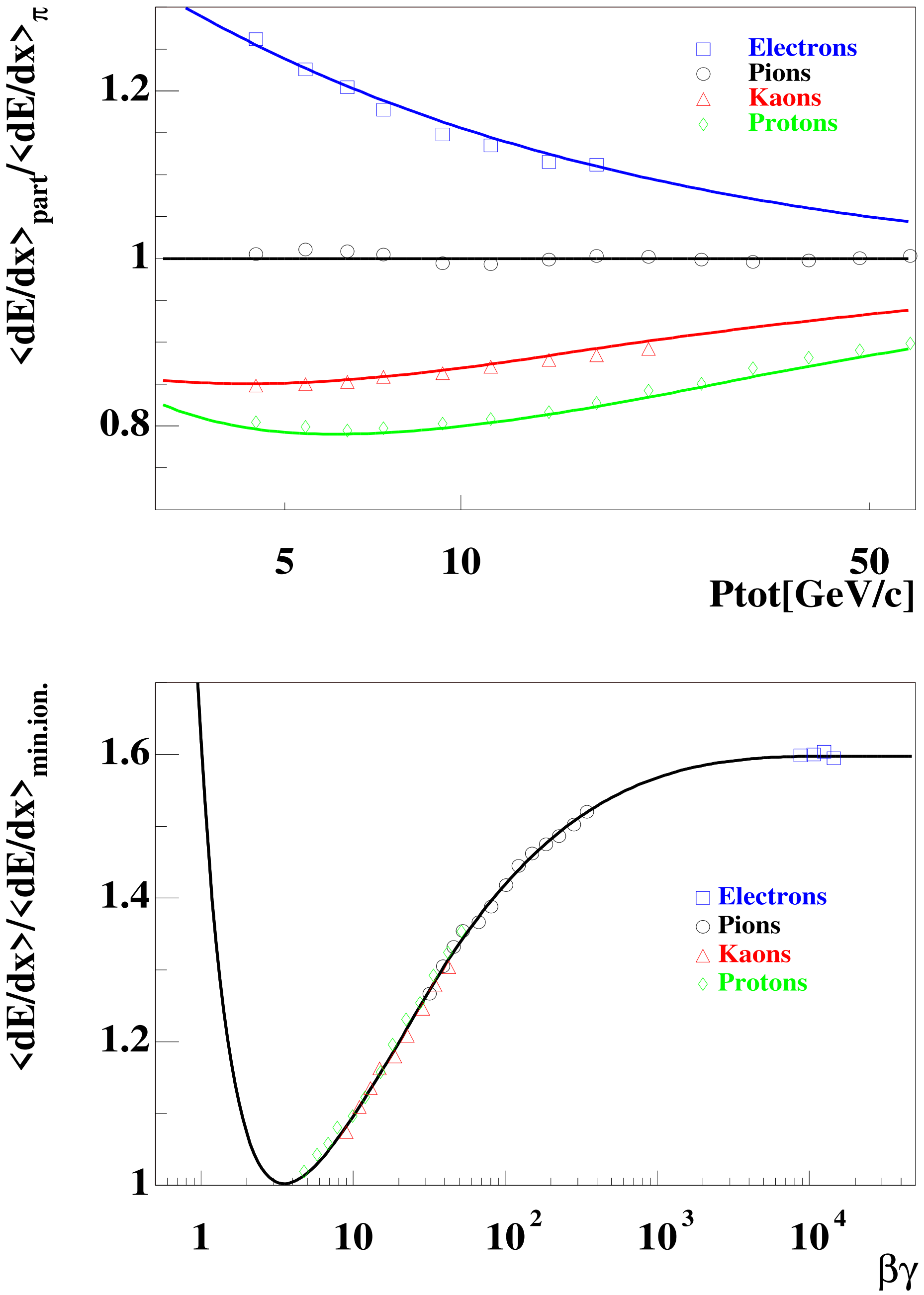

Figure 4.7 a) Measured ionization of a particle relative to the ionization of a pion as function of total momentum p. The lines represent the parametrization of the Bethe-Bloch function, the symbols are measured data.
b) Data points of the upper panel as a function of $\beta\gamma$.

given in equation 4.6 it is possible to fit the parameters of the equation to the data. The fit is indicated in Fig. 4.7 by the solid lines.
Once the shape of the Bethe-Bloch function is known the sector gains A_{sec} can be derived by measuring the ionization of the pions $I_{\pi,meas.}$ separately for each given sector and comparing it with the value predicted by the Bethe-Bloch function for the tracks crossing this sector:

$$A_{sec} = \frac{I_{\pi,meas.}}{\left\langle \frac{dE}{dx} \right\rangle_{param.} (\pi)} \tag{4.11}$$

The ionization of the pions $I_{\pi,meas.}$ traversing a given sector is calculated by selecting tracks that can be identified as pions as illustrated in Fig. 4.8a and calculating the *truncated mean* for their clusters collected in this sector. The dependence on the momentum of the selected particles is taken out by scaling the cluster charge by a factor derived from the prediction of the Bethe-Bloch parametrization. The *truncated mean* calculated from the selected clusters thus immediately yields the gain factor A_{sec} of the sector in question. Fig. 4.8b shows an example of such a Landau-distribution for a given sector.

Pad Crossing Angle

The correction for the pad crossing angle takes into account the different path length of a particle sampled on a given pad-row. The longer the path length the more ionization will be sampled. The corrected ionization (I_{corr}) is calculated from the measured ionization (I_{meas}) by a purely geometrical correction depending only on the track angles λ(dip angle) and ϕ (bending plane angle):

$$I_{corr} = I_{meas} \cdot \cos\lambda \cdot \cos\phi \tag{4.12}$$

In general this correction method is only true for a Gaussian energy loss distribution, but in case of the small track angles observed in the MTPC it will also hold for a Landau distribution.

Gas Gain

The gas gain in the proportional wire chamber depends on the pressure and temperature of the chamber gas. Since the detector system is located in a climatized environment which allows to keep the temperature stable within $\pm 0.1°$, the gas gain should depend on atmospheric pressure only. The pressure is monitored continously and is stored on tape together with the TPC data. Since the dependence of the observed ionization on the

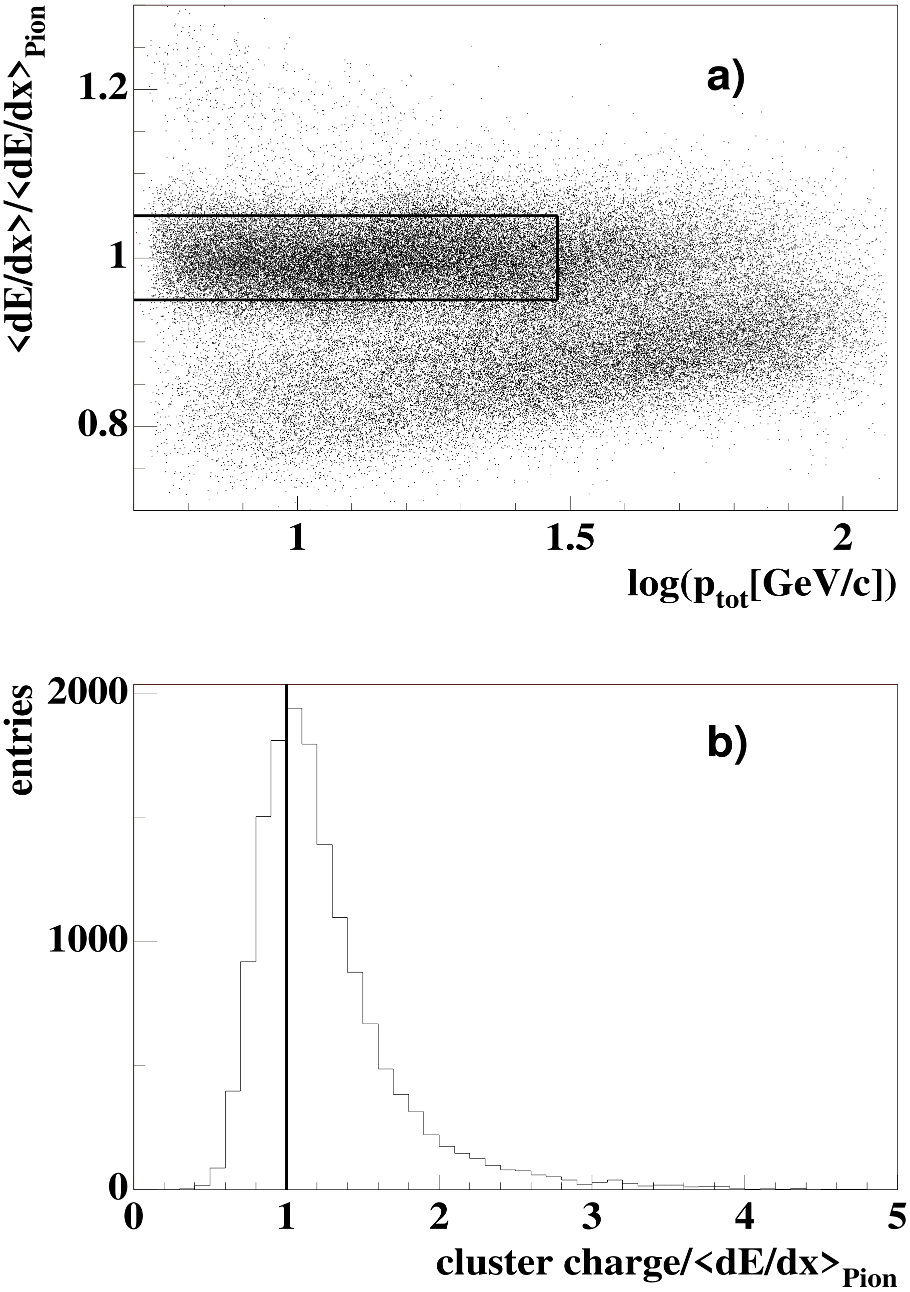

Figure 4.8 a) Selection of pion tracks used for inter-sector calibration.
b) Example charge distribution for clusters on identified pion tracks within one sector.

pressure changes with the exact gas composition, it is determined experimentally. The parameters p_1 and p_2 of function 4.13 are determined and used to normalize the ionization measurement to an atmospheric pressure of 970 $mbar$. A more detailed description of this method can be found in [46].

$$\begin{aligned}
p_1 &= 0.00328 \\
p_2 &= 0.0061 \\
p_{base} &= 970 mbar \\
\Delta p &= p_{meas} - p_{base} \\
I_{corr} &= \frac{I_{meas}}{1 - p_1 \cdot \Delta p + {p_2}^2 \cdot \Delta p^2}
\end{aligned} \tag{4.13}$$

4.4 Correction of Track Density Effects

Earlier analysis of central Pb+Pb events (e.g. [46]) revealed that the particle identification capabilities of the NA49 TPCs in a high track density environment did not meet the performance expected from the design parameters of the detectors. The observed deficiencies are summarized in Fig. 4.9, illustrating the ionisation measurement in the high track density region of the MTPCs. The observed charge loss with drift length (top panel) shows a much steeper slope (up to $20\%/m$) than the value of about $9\%/m$ expected from electron attachment and the threshold cut for the zero-suppression (see below). Also a deviation from linear behaviour can be observed around the mid plane of the detector, where the track density is highest. The resolution of the ionization measurement (middle panel) does not reach the value of 3.7% achievable with 90 independent samples of the particles ionization and exhibits a strong dependence on track density. Further a pronounced dependence on the event multiplicity is observed (bottom panel).

Since the determination of the event-by-event K/π ratio has to rely on an absolute stability of the ionization measurement a series of corrections had to be developed in the framework of this thesis in order to remove the track density dependence. The corrections can be subdivided into four different categories.

- Electronic Effects. The overshoot/undershoot structure of readout-electronics response causes a steeper drift length dependence in case of subsequent hits in one electronics channel.

- Hardware Effects. A close inspection of the raw-data revealed a crosstalk effect via the sense wires of the readout chambers. The correction of this effect is most important, since it causes the multiplicity dependence and the deteriorated resolution of the ionization measurement at high track density.

- Drift Length Dependence. In order to avoid systematic dependences of the ionization measurement it is necessary to understand the cause of the variations of the charge loss with drift distance. The corresponding steepness and nonlinearity can be attributed to an interplay of a baseline shift caused by the electronic and hardware effects and the threshold cut of the zero-suppression.

- Cluster Deconvolution. The determination of cluster charge of partially overlapping clusters is a major cause of uncertainties in the ionization measurement in a high track density environment. A cluster fitting algorithm based on the known track parameters after the pattern recognition step of the data reconstruction was introduced to allow for a proper treatment of close or crossing tracks.

In the following section the correction algorithms will be described. The relative magnitude of the different corrections and the particle identification capabilities of the calibrated TPCs will be discussed in section 4.5

Electronic Effects

The apparent baseline shift caused by the response of the readout-electronics introduced in chapter 2.2 was found to have a sizeable effect on the quality of the dE/dx determination. Due to the high track density in central Pb+Pb events single electronic channels will record several hits. The charge of each hit will be measured relative to a baseline which is lowered by earlier hits. This affects the pulse height of a given hit, but also the effective threshold cut for clusters measured at long drift distances.
The electronic response is measured by averaging over a large number of laser events, where the ionization and position of the laser tracks are kept constant [47]. The baseline position in time bins following a given signal can thus be measured with good accuracy even though the raw data is only stored with integer precision. Fig. 4.10 shows the normalized baseline shift caused by a signal of 250 $ADCcounts$ in the MTPC high resolution sectors. Due to the direct measurement in the detector this baseline shape also contains features related to the pad readout of the detector. The short term undershoot/overshoot structure of the shaper response is followed by an 0.2% undershoot. The latter can be related to the fact that practically no positive ions arrive at the pad plane which requires the time integral over the signal to be zero. Also the absorption of

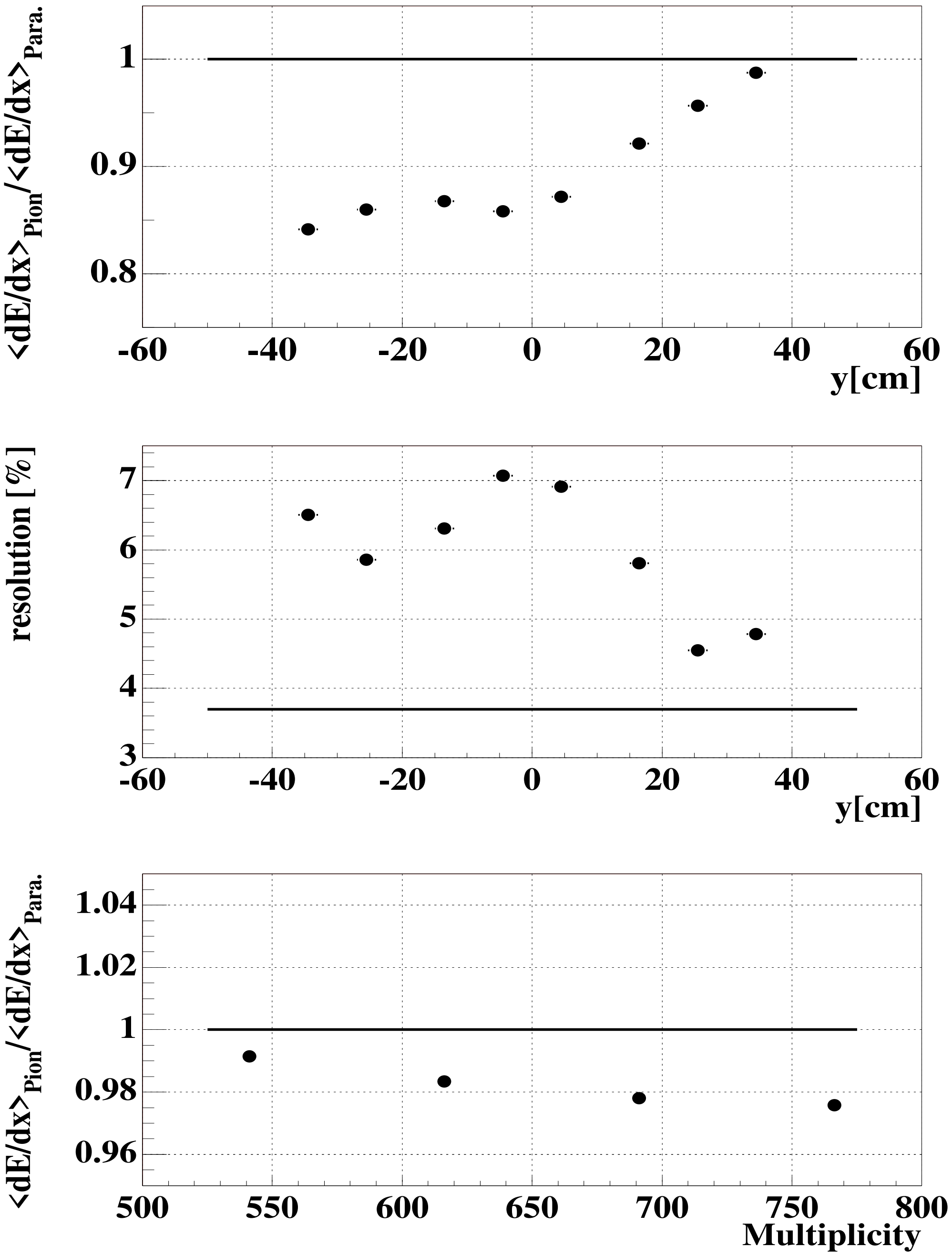

Figure 4.9 Influence of high track density on the ionization measurement.
Top Panel: Drift length dependence of the ionization measurement.
Middle Panel: Drift length dependence of the resolution.
Bottom Panel: Multiplicity dependence of the ionization measurement.
The horizontal lines drawn in the plots indicate the behaviour of an "ideal" detector.

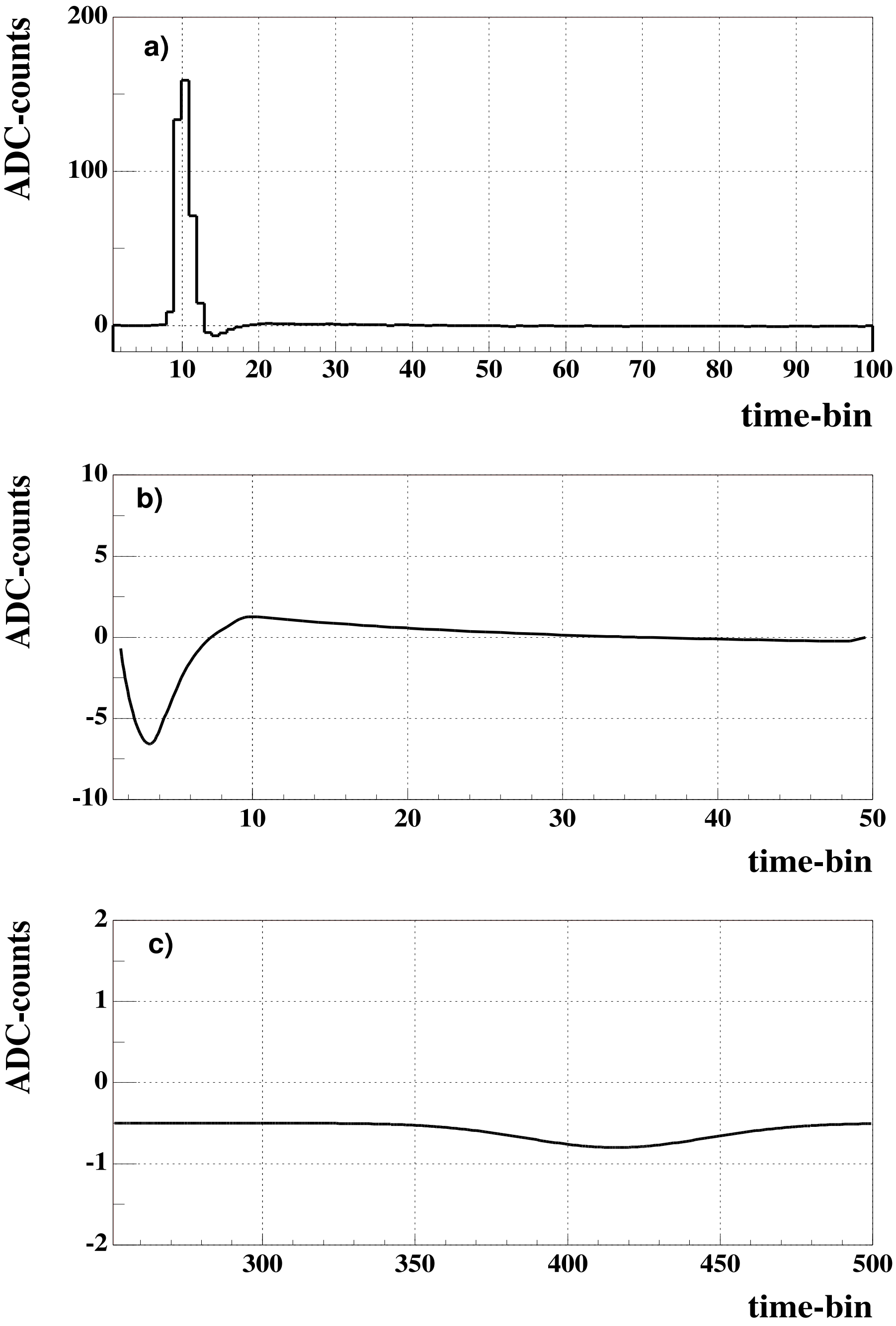

Figure 4.10 Electronics response to a signal of 250 *ADC counts* generated by a laser track.
a) Input Signal.
b) Zoom on the shortterm features caused by the signal shaping unit.
c) Zoom on the long range features consisting of a 0.2% baseline drop and a signal of negative polarity caused by the arrival of positive ions at the field wires.

the positive ions at the field wires can be seen as a signal of negative polarity at time bin 430.
The necessary correction is done separately for each pad, i.e. each electronics channel. A given channel samples 512 time bins spanning the drift range of the TPC. From the charge value recorded in each time bin the baseline shift for all following time bins is calculated by folding this time bin with the measured electronics response. Thus it is possible to restore the actual baseline and calculate the true pulse heights. Panel a) of Fig. 4.11 shows an example of signals recorded in a readout channel of the MTPC high resolution sector. Folding the measured signals with the electronics response the baseline shift shown in panel b) of the figure can be calculated. Panel c) shows the signal after adding the calculated baseline to the recorded signals.
Applying this correction does not improve the resolution significantly, but it accounts for a charge loss of up to $3\%/m$ depending on track density due to the loss of pulse height (see section 4.5).
There are also gain changes in individual amplifiers which are traced to the total charge load of the VLSI shape/preamp chips. Analyzing the laser data it was found that the charge in a given pad-time pixel is reduced by an amount corresponding to 0.7% of the total input charge of the chip (16 pad-channels). This is also corrected for while unpacking the raw data during the off-line reconstruction. The effect of this correction however is negligibly small and will not be discussed here.

Hardware Effects

The most relevant correction of the charge measurement in TPCs in a high track density environment was found to be a basic property of the wire chamber itself. To understand the nature of this effect one has to keep in mind that what is measured in case of a wire chamber with pad readout is the image charge induced on the pads by the positive ions remaining behind in the avalanche of the gas amplification process. The current drawn to the pads by the capacitive coupling of the space charge of the ions is measured by charge sensitive amplifiers and then processed by the signal shaping units.
The arrival of electrons on the sense wire at the end of the gas amplification process leads to an effective change of the sense wire voltage on the time scale of $< 100ns$ (1 time bin). The potential is restored by the high voltage supply through a RC network (Fig. 2.5) with time constant of about $5\mu s$ (50 time bins). Note that each RC network feeds 6 sense wires (one wire group). All wires within one wire group thus will be at equal potential.
Due the capacitive coupling to the pads, discharging and charging of the wires induces a bipolar signal on all pads facing the wire group in which the original signal deposited

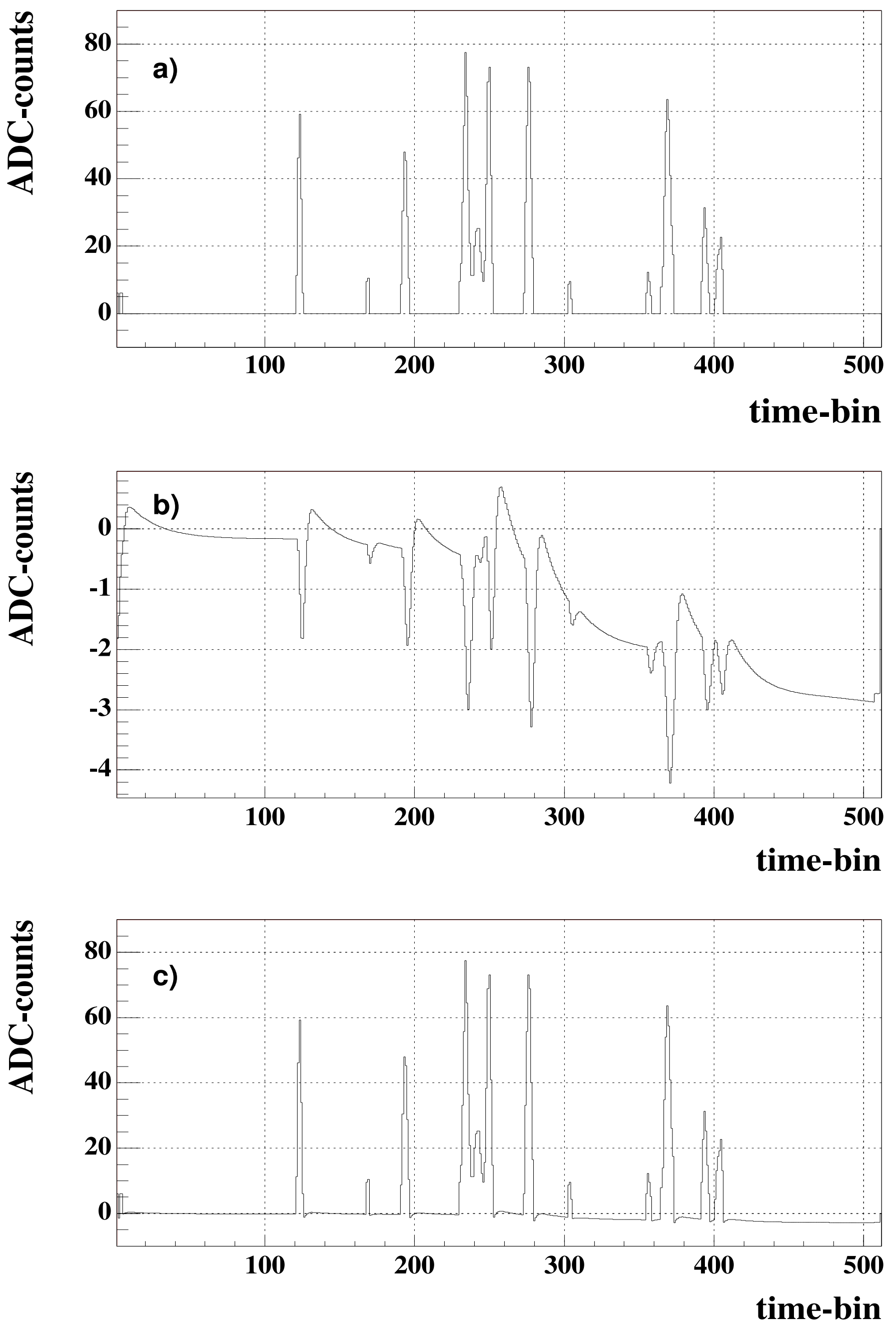

Figure 4.11 Baseline position calculated from input signal by folding the signal with the measured electronics response.
a) Input Signal.
b) Baseline shift calculated from input signal.
c) Signal corrected for baseline shift.

the electrons. In the MTPCs 3 pad-rows face the same wire group. Since this effect spreads over a whole pad-row it will be referred to as "lateral crosstalk".

The fast rise time of the discharging process causes a simultaneous undershoot. Fig.

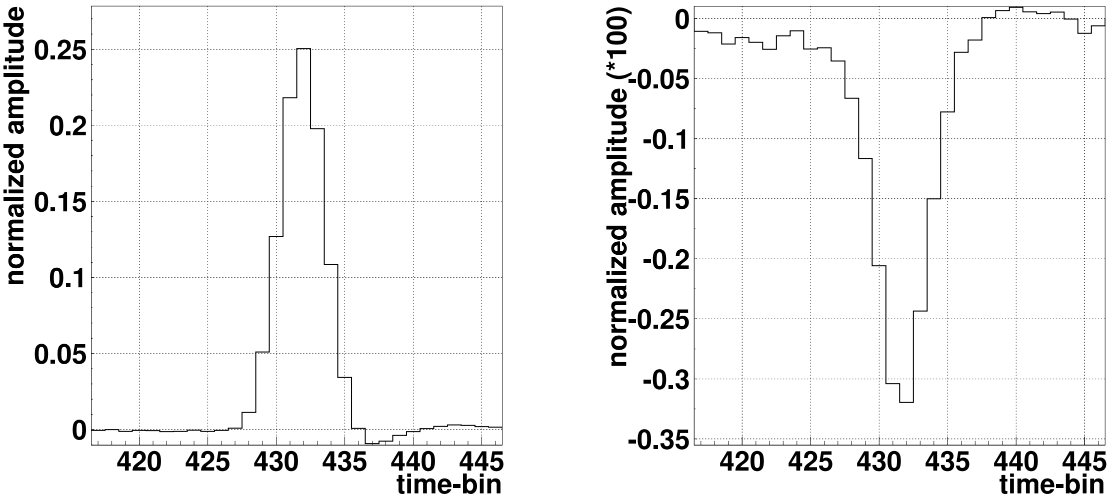

Figure 4.12 Left panel: Signal of a laser track crossing a randomly chosen pad-row where the signals of the 6 contributing pads are summed and normalized to the integral charge. Right panel: signal on a single distant pad of the same pad-row in the same time region using the same normalization (1 time bin = 100 ns).

4.12 shows a real signal of a laser track (left panel) induced on a pad and the undershoot caused by this signal on pads distant to the signal, but facing the same wire group. This effect causes a reduction of all signals measured in the same time plane by all pads of the three pad-rows facing the same wire group by 0.21% of the total charge measured in this time plane.

The charging of the wire group then leads to an overshoot observed as a long range effective baseline shift, since the time integral of the undershoot/overshoot structure of the signal has to be zero.

The net effect of the capacitive coupling of changes in the sensewire potential to the pads is equivalent to a change of the electronics baseline and will be referred to as such in the following discussion.

The influence of this effect on the data is illustrated in Fig. 4.13. On the left hand side of the figure an example for a signal in a time plane is sketched, while on the right hand side the baseline shift caused by this signal is shown. The baseline shift is given in percent of the total charge deposited in the time plane containing the signal. The time dependence of the charging and decharging of the wire group illustrated in the right hand plot results in a drop of the baseline (1) for all signals within the same time plane as the signal and a rise in the baseline for all following time planes (2).

This effect has also been measured with laser data, but for single hits this effect is so

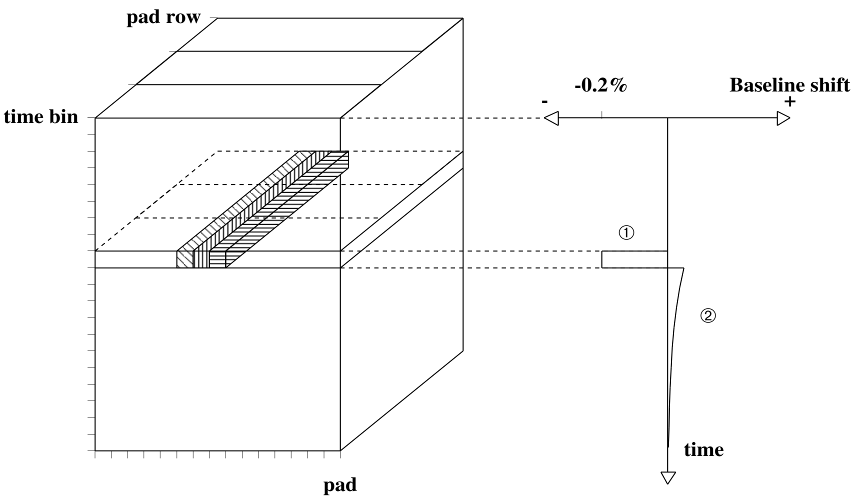

Figure 4.13 Sketch of the baseline shift caused by the lateral crosstalk effect. The left hand side of the figure shows the signal with a given time plane. The right hand side shows the baseline shift resulting from the signal in the time plane of the signal (1) and in the following time planes (2).

small, that only the magnitude of the undershoot can be measured with acceptable precision. The shape and time constant of the overshoot is not accessible with laser-data. Also the time constant as given by the capacity of the wire chamber and the high voltage feed resistor could not provide a precise enough estimate of the overshoot shape. In order to derive the appropriate parameters it is necessary to look at the measured data itself. As will be discussed below the drift dependence of the measured ionization does not show the linear behaviour expected from the nature of the other corrections to be applied. With the assumption that the track density related hardware effects are the cause of the short scale deviations from the linear behaviour we can now "fit" the shape of the overshoot by picking a given shape and testing the linearity of the resulting drift dependence.
The shapes found to yield the best results are illustrated in Fig. 4.14. The MTPC standard resolution sectors can be corrected with a single exponential shape, for the MTPC high resolution sectors a second shorter range exponential has to be added.
The data is corrected by filtering the unpacked raw data of a whole wire group with the derived shape. For this purpose the total charge content of each time plane corresponding to this wire group is calculated. From this value the baseline shift within this and all following time planes can be calculated. The calculated baseline shift then has to be added to each charge pixel. The top panel of Fig. 4.19 shows the magnitude of

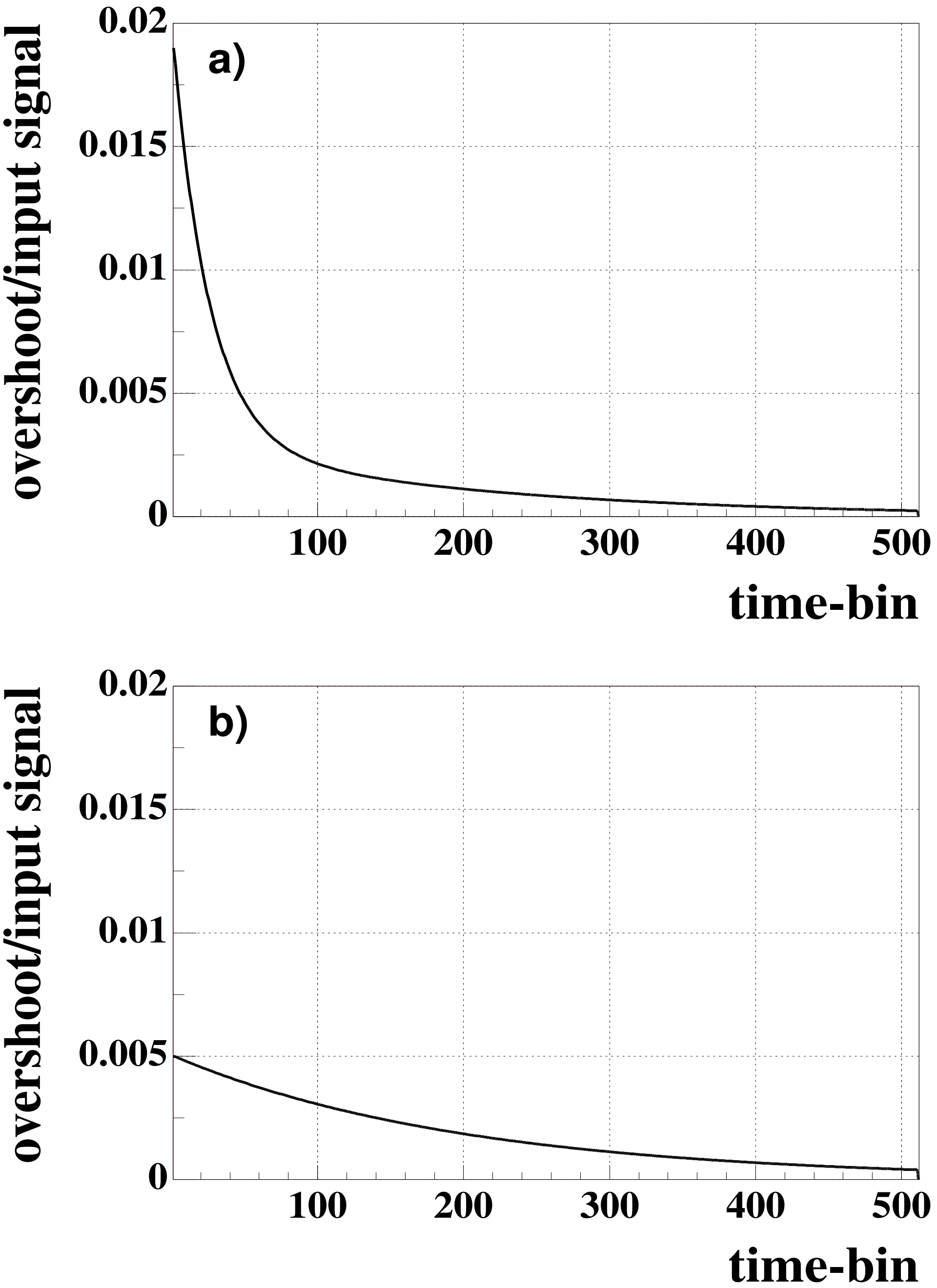

Figure 4.14 Derived overshoot shapes for the hardware correction. a) MTPC high-resolution sectors: A sum of a short and long range exponential is needed to correct the data. b) MTPC standard resolution sectors: A single exponential shape is sufficient for the correction.

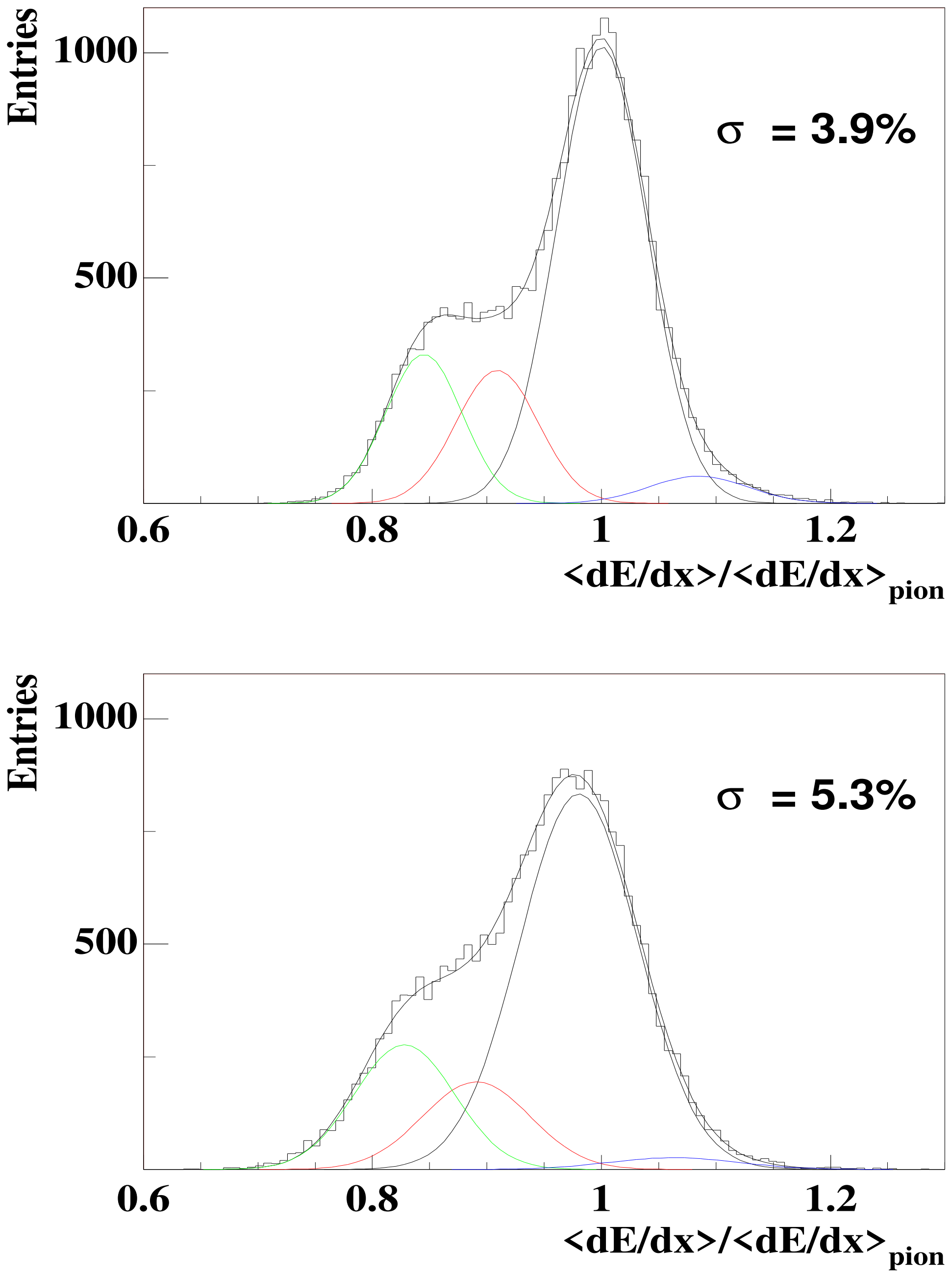

Figure 4.15 Resolution of the ionization measurement with (upper panel) and without (lower panel) the lateral cross talk correction.

the cross talk constants in a single central Pb+Pb event for the MTPC high resolution sectors. The values plotted are the number of ADC counts added to each charge pixel in the corresponding wire group as calculated in the filtering process of the raw data distribution. Taking into account that a cluster in the MTPC consists on average of 30-40 charge pixels this correction can add up to a 10% effect on the total cluster charge (see section 4.5). This effect is the main cause of the multiplicity dependence and the deterioration of resolution in the high track density region.
To illustrate the increase of resolution when applying the lateral cross talk correction Fig. 4.15 shows the dE/dx spectrum for the same momentum bin in the high track density region of the MTPC with (top panel) and without (lower panel) the correction.

Drift Length Dependence

A significant correction has to be introduced due to the observation of a drift length dependence of the measured ionization. A charge loss as a function of drift length is expected from two effects:

- Electron attachment to O_2 molecules contaminating the chamber gas is expected to result in a approximately linear charge loss of about 2% per meter, given the monitored O_2 content.

- The zero suppression threshold cut of 5 ADC counts causes an apparent charge loss, since the clusters widen with drift length due to diffusion. This cut results in a charge loss of typically 7% per meter. An analytical calculation estimating this effect can be found in [66].

Since the charge loss effects are small compared to the total cluster charge it can safely be assumed to be linear in drift distance (see Fig. 4.16).
The charge loss as a function of the drift length of the clusters is measured by selecting tracks of a certain momentum range that lie in the sector type to be studied and by generating separate dE/dx spectra for track ensembles in different drift length intervals. The momentum dependence is taken out by dividing the measured ionization $I_{meas.}$

by the expected ionization predicted for pions dE/dx_π by the parametrization of the Bethe-Bloch equation.

$$I_{scale} = \frac{I_{meas.}}{dE/dx_\pi} \tag{4.14}$$

For pions in the track sample the scaled ionization I_{scale} does not depend on momentum and should be distributed around unity. To derive the drift length dependence four Gaussians are fitted to each I_{scale} spectrum in a given y-bin, one for each particle species, and the fitted position of the pion peak is plotted against the drift length.
The charge loss is corrected for by scaling the measured cluster charge $C_{meas.}$ according to the drift distance $l_{drift}[m]$ with the drift dependence $D_{loss}[\%/m]$ observed in the uncorrected data:

$$C_{corr.} = C_{meas.} \cdot \frac{1}{1 - l_{drift} \cdot D_{loss}/100} \tag{4.15}$$

Fig. 4.16 illustrates the correction of the linear charge loss effects remaining after the

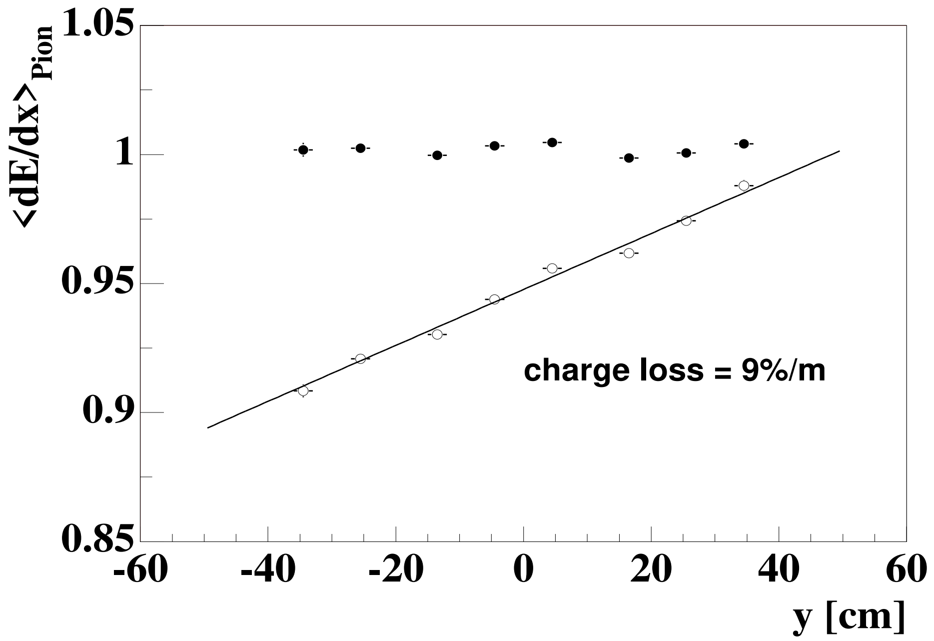

Figure 4.16 Correction of the linear charge loss effect. The open symbols reflect the uncorrected data. A straight-line fit to the uncorrected data shows a charge loss of $9\%/m$. The corrected data is represented by the full symbols.

correction of the electronics and lateral crosstalk effects. The open symbols reflect the uncorrected data fitted with a straight-line. The slope of the straight line corresponds to a charge loss of $9\%/meter$. The full symbols show the corrected data.
The correction of the linear charge loss is done after the hardware and electronics re-

sponse effects are dealt with. The data not corrected for these effects shows a much stronger dependence on drift length than expected. For central Pb+Pb events values of up to 20% were measured compared to the 9% per meter expected from the linear effects described above. The cause of this discrepancy can be understood by the drop of the baseline caused by the electronics and hardware effects. A lower baseline not only leads to a reduced measured pulse height, but also to a higher effective threshold cut for the zero suppression which will cause a steeper drift length dependence. This effect can directly be observed in the data, by measuring the charge loss for events in bins of multiplicity. The magnitude of the baseline drop is related to the event multiplicity.
Fig. 4.17 shows the threshold cut of 5 ADC-counts modified by the average baseline drop calculated by the correction algorithms of the electronics and hardware effects for peripheral Pb+Pb events plotted against the event multiplicity. A direct correlation between multiplicity and drop of baseline can be observed. The contribution of the different effects to the baseline drop is illustrated in Fig. 4.19.
This information can be used to calculate the average baseline drop for each event and to study the charge loss per meter as a function of the effective threshold cut.
Fig. 4.18 shows a linear dependence of the observed charge loss on the effective threshold. The line drawn in the figure is the result of a Monte-Carlo simulation of this effect [48] taking into account a truncated Landau energy loss distribution, the diffusion of the charge cloud in the drift process and the pad response function. The data shows the same trend as predicted by the simulation.
This effect can of course be accounted for in the correction algorithms of the drift length dependence, but, as it will be discussed in the following chapter, the switching from cluster charge determination by summing up charge pixels in the cluster finder to deriving the cluster charge by a fitting algorithm strongly reduces the sensitivity on a varying threshold. The influence of this effect is negligible when employing the cluster fitting procedure.

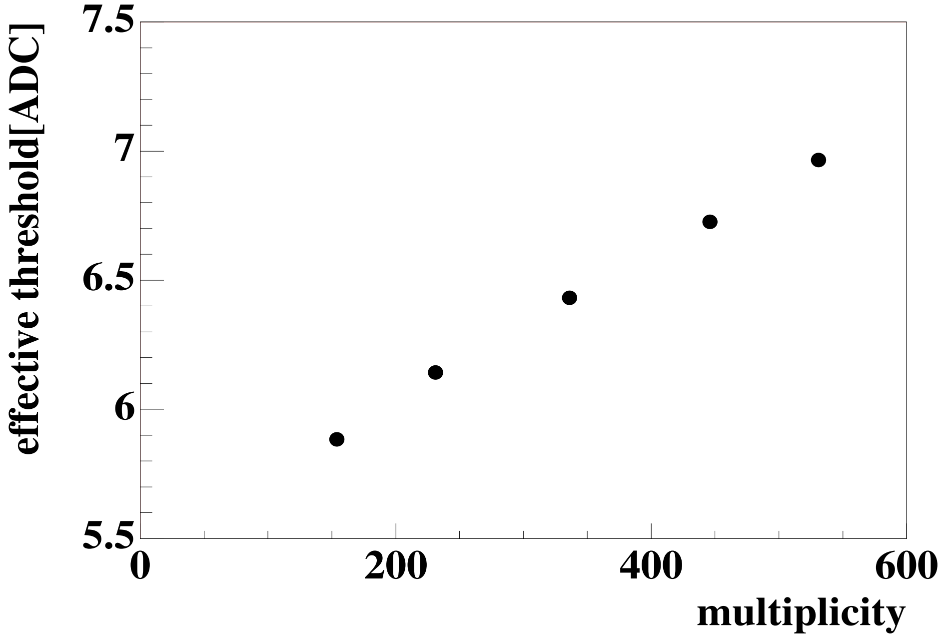

Figure 4.17 Dependence of the effective threshold cut [*ADC counts*] on the event multiplicity. The effective threshold is derived from the baseline shift calculated for the correction of the electronics and hardware effects.

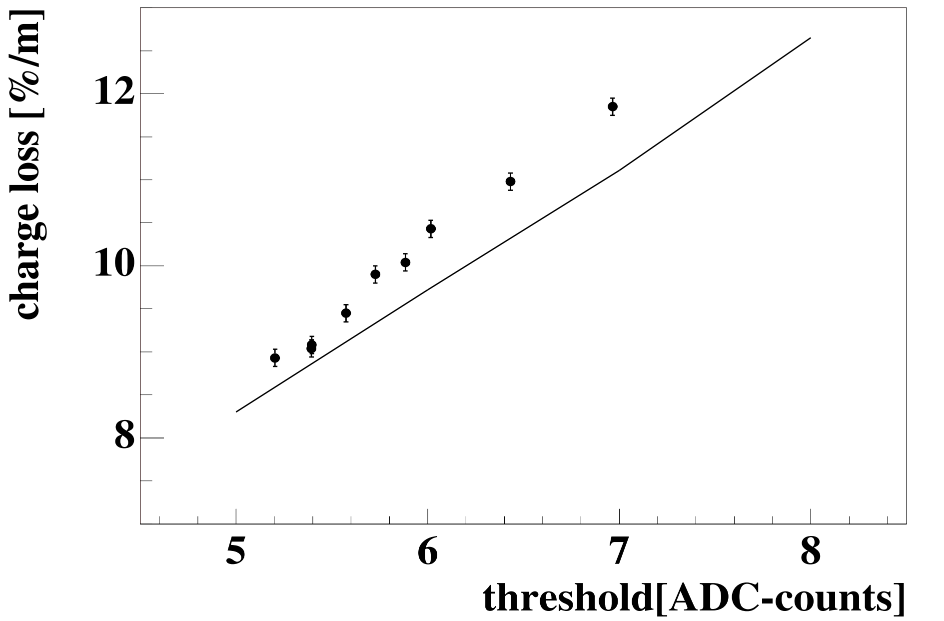

Figure 4.18 Dependence of charge loss [$\%/m$] on effective threshold cut [*ADC counts*]. The symbols represent the data. The line indicates a prediction by a Monte-Carlo simulation.

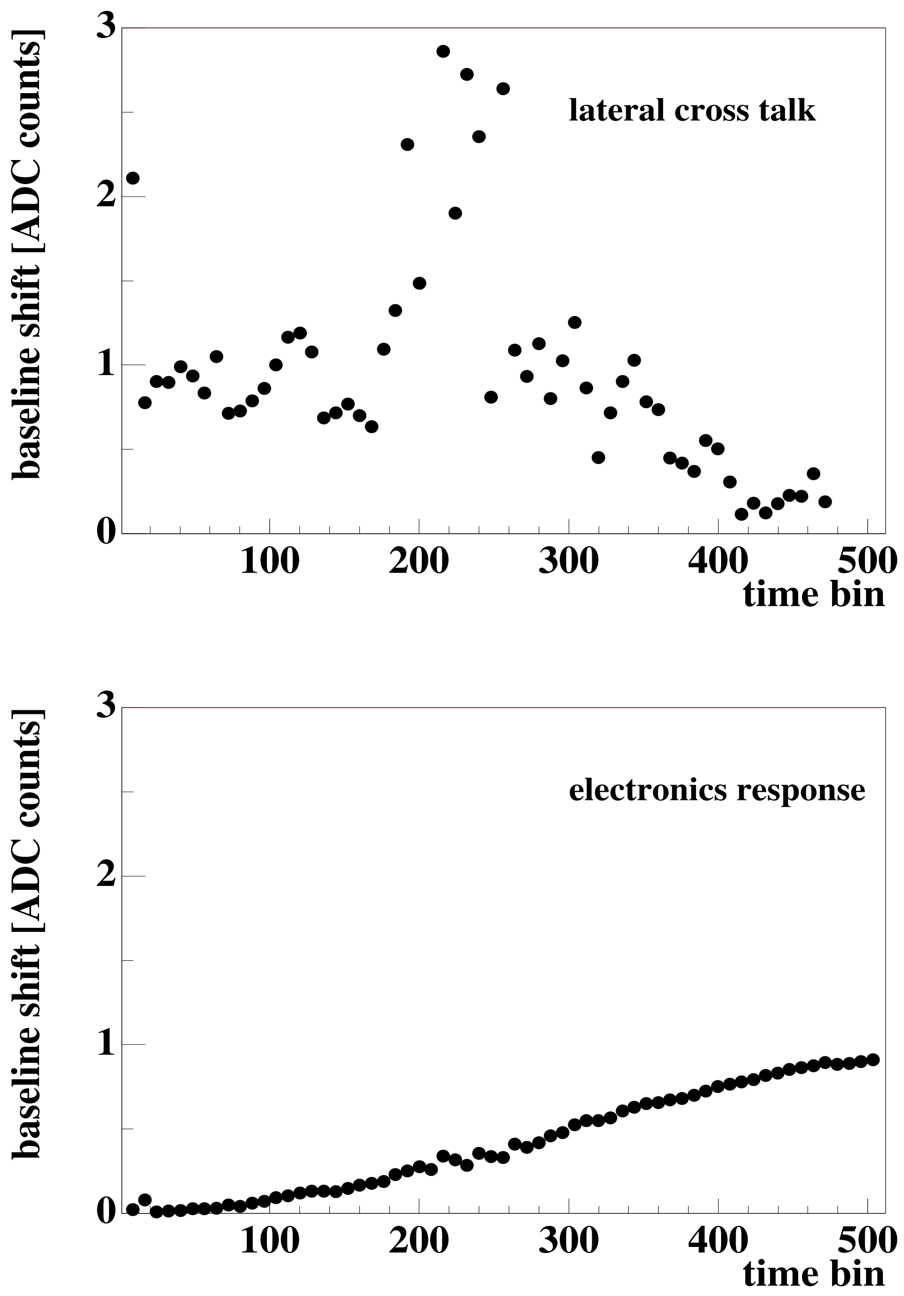

Figure 4.19 Baseline shift due to lateral cross talk and electronics response measured for a single central Pb+Pb event in the MTPC high resolution sectors.
Top panel: Lateral cross talk constants averaged over the wire groups of the high resolution sectors as a function of drift time.
Bottom panel: Average baseline shift in the electronics channels of the high resolution sectors as a function of drift time.

Cluster Deconvolution

The reliability of the ionization measurement depends strongly on the determination of the cluster charge. The straight forward cluster finder approach used for the tracking step showed serious problems when determining the cluster charge in the high track density areas. As soon as clusters start to overlap the distribution of the found charge among the adjacent clusters is not reliable enough without further constraints. If the cluster finder misses a cluster in a continuous charge region produced by more than one track the found charge tends to be distributed among the found clusters. This results in a too high charge measurement, which translates into a tail towards high ionization for the truncated-mean spectra in the high track density regions. In order to obtain a ionization measurement that is stable against track density variations it was necessary to implement a new method of cluster-charge determination. This procedure consists of the following steps:

1. Standard tracking.

2. Compute expected cluster width from track angles and drifth length.

3. Get the positions of potential clusters by extrapolation of tracks to their intersection with the pad planes.

4. Go back to the raw-data and fit the charge distribution by one or more 2-dimensional Gaussians in accordance with the number of tracks passing through the corresponding volume element.

This method allows to unfold partially overlapping tracks and yields a very robust ionization measurement. It also reduces the sensitivity of the charge measurement on the local baseline shifts, since the fit also estimates the charge contained in the tail of a cluster that is usually lost by the threshold cut. Fig. 4.20 shows a comparison of the charge loss as a function of the effective threshold cut for the cluster charge obtained from the summation of charge pixels in the cluster finder (open symbols) and the cluster charge derived by the cluster fitting algorithm. Going back to the raw data once the

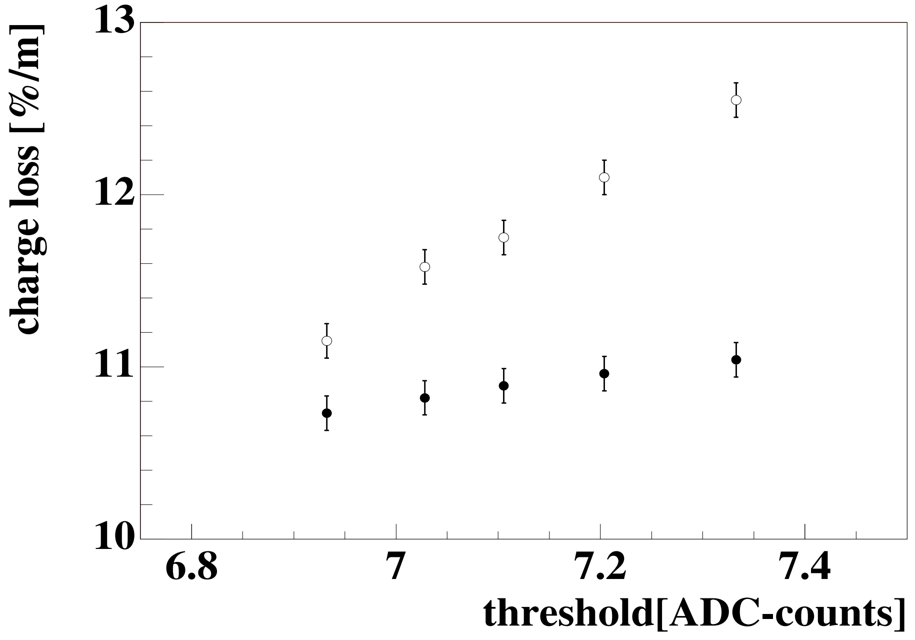

Figure 4.20 Dependence of charge loss [%/m] on effective threshold cut [ADC $counts$]. The open symbols represent the values obtained from the summation of charge pixels in the cluster finder. The full symbols correspond to the value resulting from the cluster charge derived from a fit to the charge distribution of the clusters.

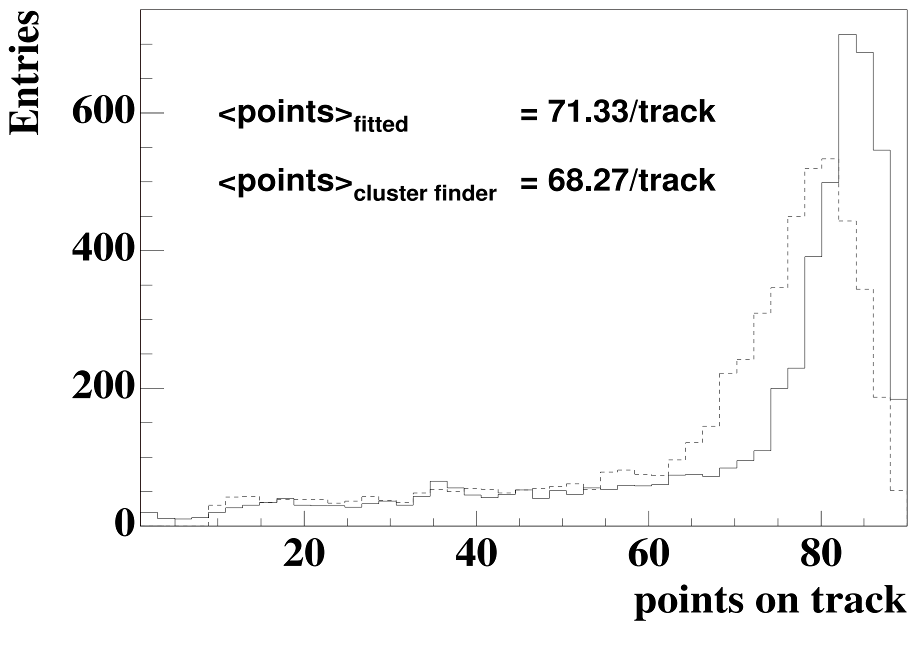

Figure 4.21 Number of points found in the MTPC by the cluster finder (dashed line) and the cluster fitting algorithm (solid line).

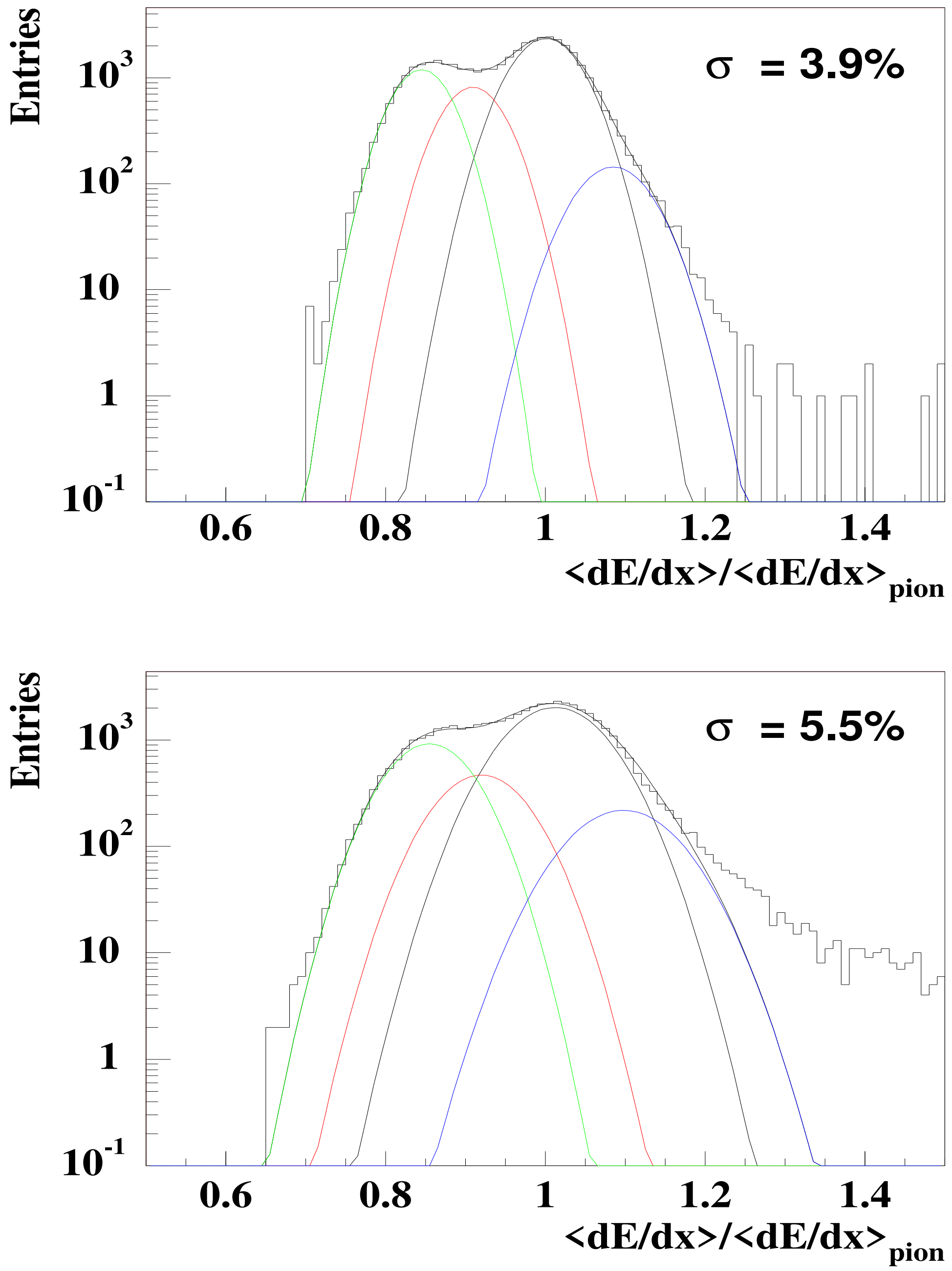

Figure 4.22 Resolution of the ionization measurement with (upper panel) and without (lower panel) the cluster fitting procedure. Note the tail to high ionization values in the lower panel. For this comparison tracks in a total momentum range from 20 to 30 GeV/c with more than 30 points contributing to the ionization measurment were selected.

track parameters are known also increases the clustering efficiency. Fig. 4.21 shows a comparison of the number of points on track found by the cluster finder and fitting algorithm. Fig. 4.22 shows the performance of the cluster fit in comparison to the standard procedure of summing up charge pixels in the high track density region. We can immediately see that the resolution of the ionization measurement is significantly increased from 5.5% to 3.9% and also the tail to high dE/dx values present on the level of a few percent in the cluster finder gets suppressed to the sub per mille level.

4.5 PID-Performance of Calibrated NA49-TPCs

The Drift Dependence

The application of the correction algorithms described above shows that it is possible to explain the previously un-understood influences of high track densities. The interplay of cluster diffusion and the apparent shift of the baseline due to the large amount of charge deposited in the chamber results in the shape of the drift dependence seen in the uncorrected data (Fig. 4.23 top panel, open squares). Applying the corrections shows that it is not only possible to remove the dependence on the drift distance, but also that the resolution of the ionization measurement increases and becomes much less dependent on the drift distance. Fig. 4.23 illustrates the influence of the different corrections in the high track density region of the MTPC. The data shown is based on the cluster charges derived from the fit algorithm. The magnitudes of the different corrections are shown in Fig. 4.24. The observations can be summarized as follows:

- The slope of the drift dependence is determined by the linear charge loss effects (electron attachment and threshold cut of the zero-suppression) and the baseline shift due to the response of the readout electronics.

- The deterioration of the resolution is related to the lateral crosstalk effect, which also accounts for the non-linearity of the drift dependence.

The Track Density Dependence

The dependence of the ionization measurement on the track density was found to be a major cause for systematic uncertainties in measurements of event-by-event observables based on particle identification. The influence of the local track density on the ionization mesurement can be removed by the proper estimation of the local baseline position in

combination with the cluster charge determination by a 2-dimensional Gaussian fit to the charge distribution of the cluster. Fig. 4.26 shows a comparison of the dependence of the ionization measurement on the event multiplicity in the high track density region of the MTPC with (full symbols) and without (open symbols) the corrections developed in the framework of this thesis. The corrected data does not show a significant dependence on multiplicity in the position of the pion peak as well as in the resolution of the measurement.
To further illustrate the track density effects Fig. 4.25 shows the resolution of the ionization measurement as a function of total momentum p_{tot}. The strong forward focussing due to the fixed target setup of the experiment the track density in the MTPCs increases with total momentum. The uncorrected data (open circles) shows a deterioration of the resolution with increasing momentum. The correction of the lateral crosstalk effect significantly reduces this dependence (open triangles). Combining the lateral crosstalk correction with the cluster fit (full circles) shows that it is possible to almost fully eliminate the track density effects.

Separation Power

The identification and correction of systematic errors in the ionization measurement also has a substantial influence on the overall resolution of the particle identification. The ability to distinguish between different particle species is given by the separation power S_{ij} of the detector, defined as the separation between two particle species i, j expressed in terms of standard deviation of the ionization measurement $\sigma_{ion.}$:

$$S_{ij} = \left(1 - \frac{dE/dx_j}{dE/dx_i}\right) \cdot \frac{1}{\sigma_{ion.}}. \tag{4.16}$$

Fig. 4.27 shows a comparison of the separation power between pions and kaons of the uncalibrated and calibrated detector. Aside from removing systematic dependences and making the ionization measurement more stable against track density variations, applying the calibration and corrections introduced above increases the separation power for particle identification by up to a factor of two.

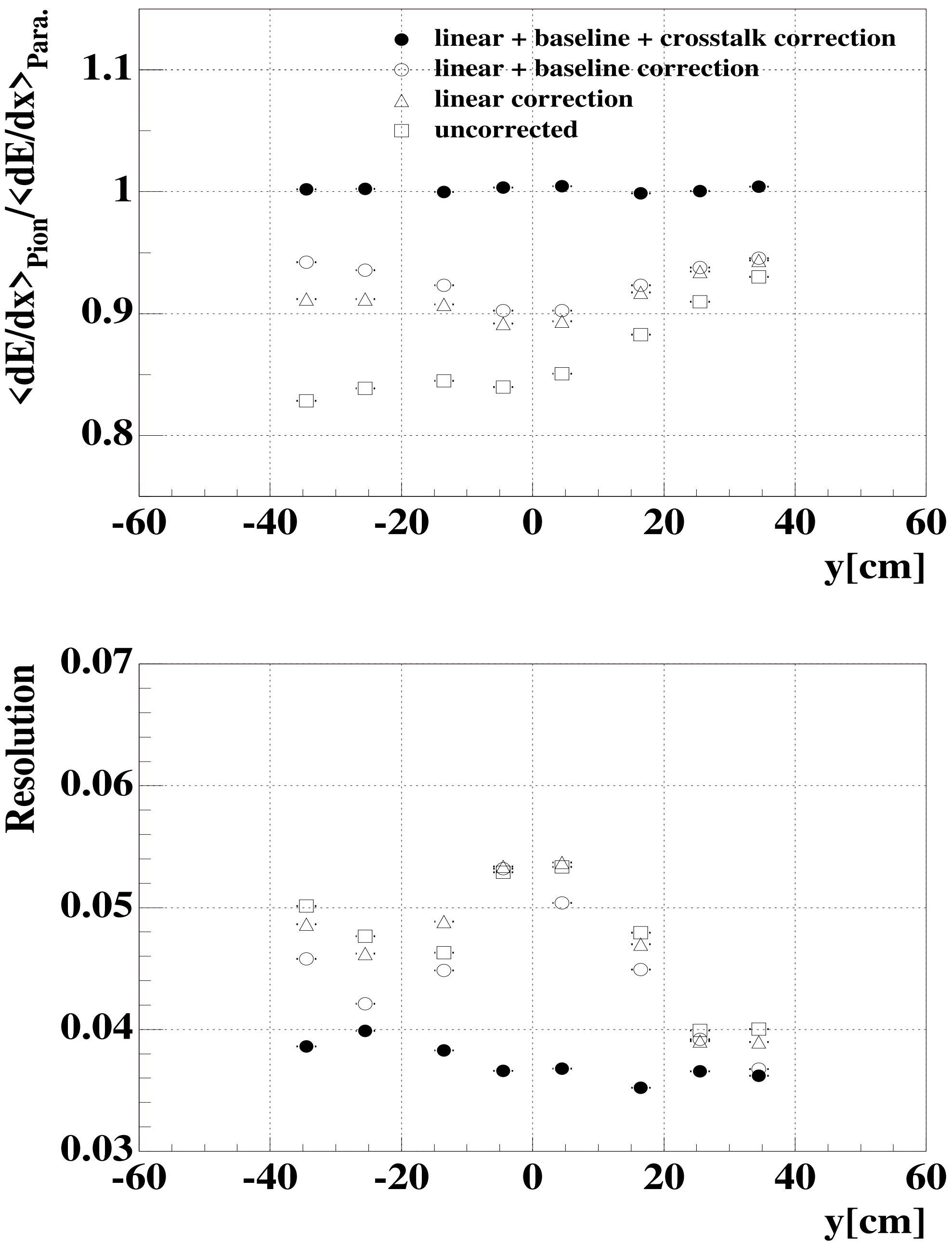

Figure 4.23 Top panel: Driftlength dependence of the ionization measurement after application of the different corrections.
Bottom panel: Resolution achieved by the corrections.

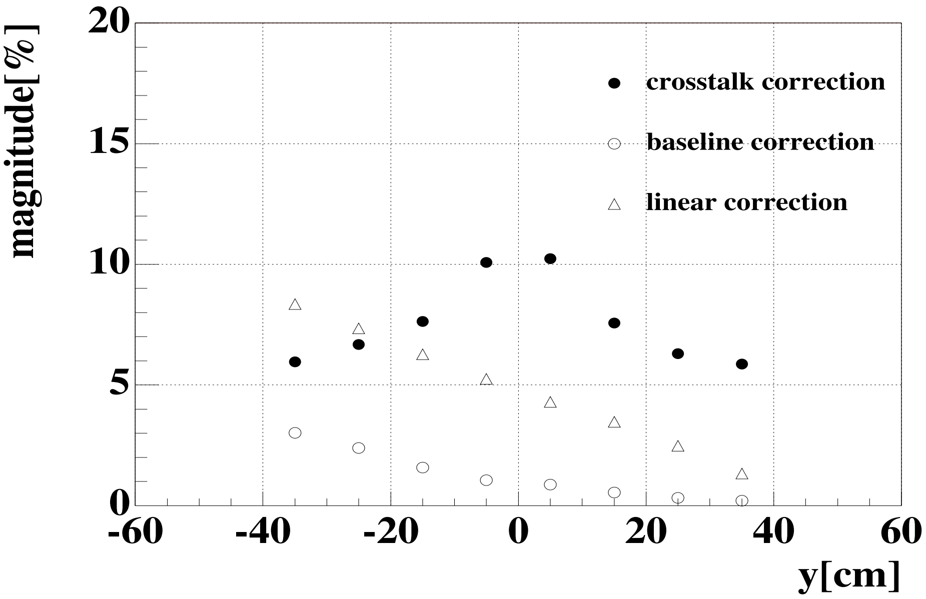

Figure 4.24 Magnitude of the different driftlength dependence corrections in percent.

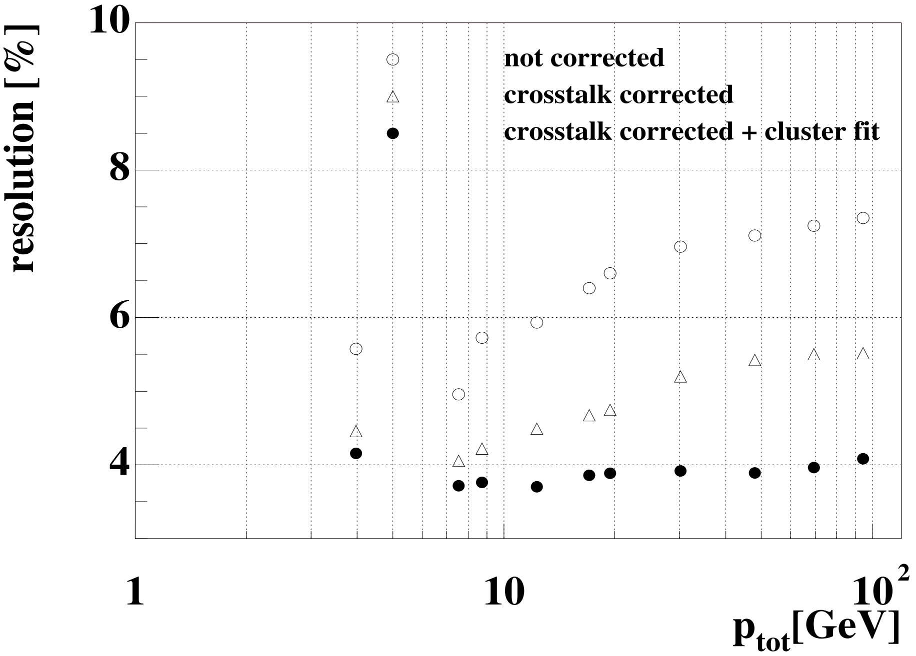

Figure 4.25 Resolution of the ionization measurement as a function of total momentum p_{tot}.
Open circles: Uncorrected data.
Open triangles: Data corrected for lateral crosstalk effect.
Full cirles: Combination of lateral crosstalk correction and cluster fit.

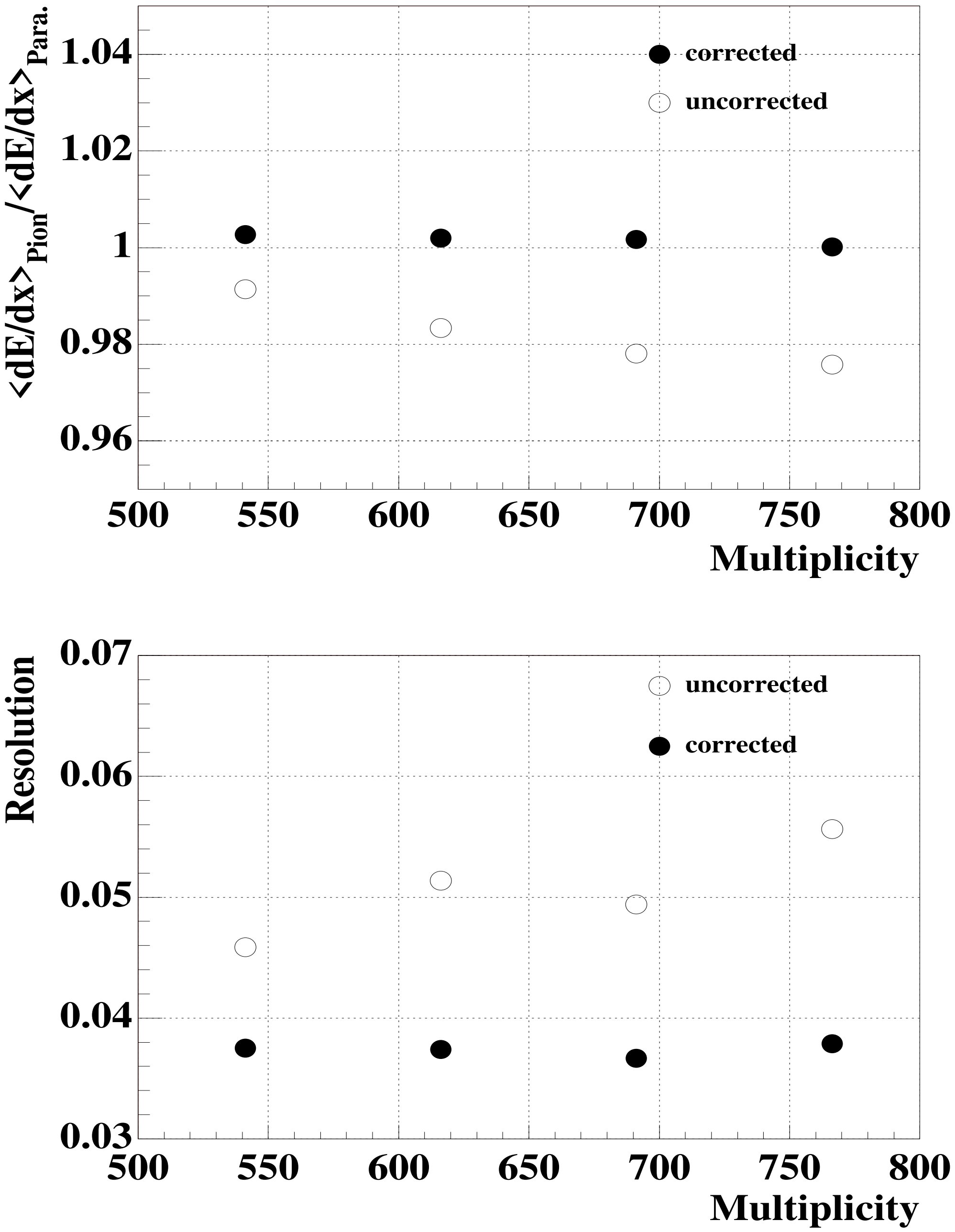

Figure 4.26 Multiplicity dependence of the ionization measurement.

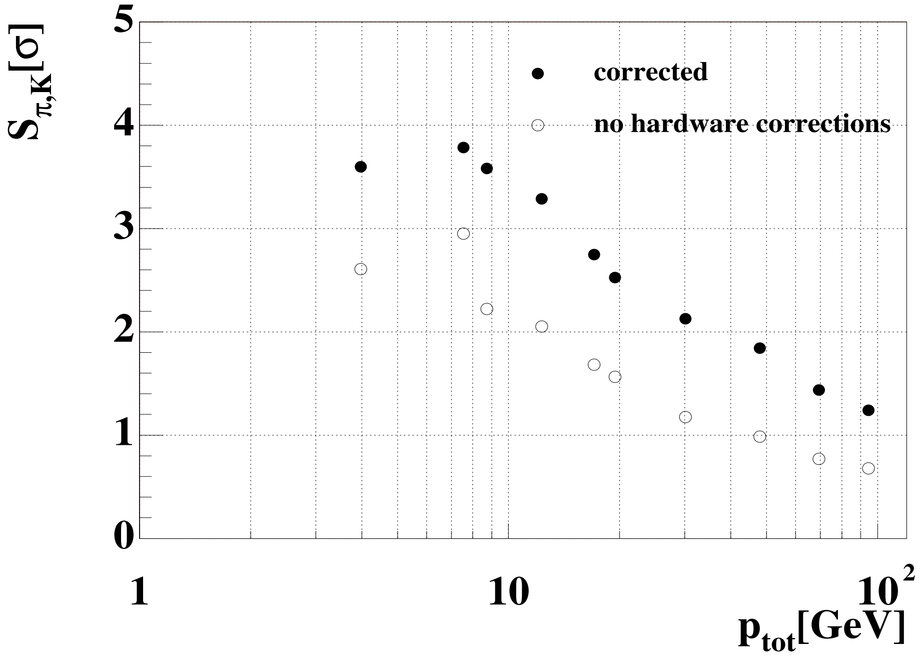

Figure 4.27 Separation of kaons and pions in terms of standard deviations as function of total momentum. The full symbols represent fully calibrated data, the open symbols refer to data without the hardware and baseline corrections.

Time Stability

The analysis of large data sets requires the ionization measurement to be stable over long periods of time. Even stabilising the temperature and precisely measuring and correcting for changes of the atmospheric pressure leaves room for changes in the effective gain of the order of a few percent over longer periods of time. There are a number of possible explanations for this, like changes in the temperature of cabels and power supplies outside the air conditioned area leading to small variations of the high-voltage supply of the readout chambers. A method of creating a time reference and following the changes in gain by looking at the data itself has proven very helpfull. A detailed description of this method can be found in [67]

Within the data set used for this analysis no significant dependence on time after correction was observed, as demonstrated in Fig. 4.28. The line shown in the top panel of this figure is a straight-line fit to the data. The slope of the fit is sufficiently small to assume that no time dependence is left in the dE/dx measurement.

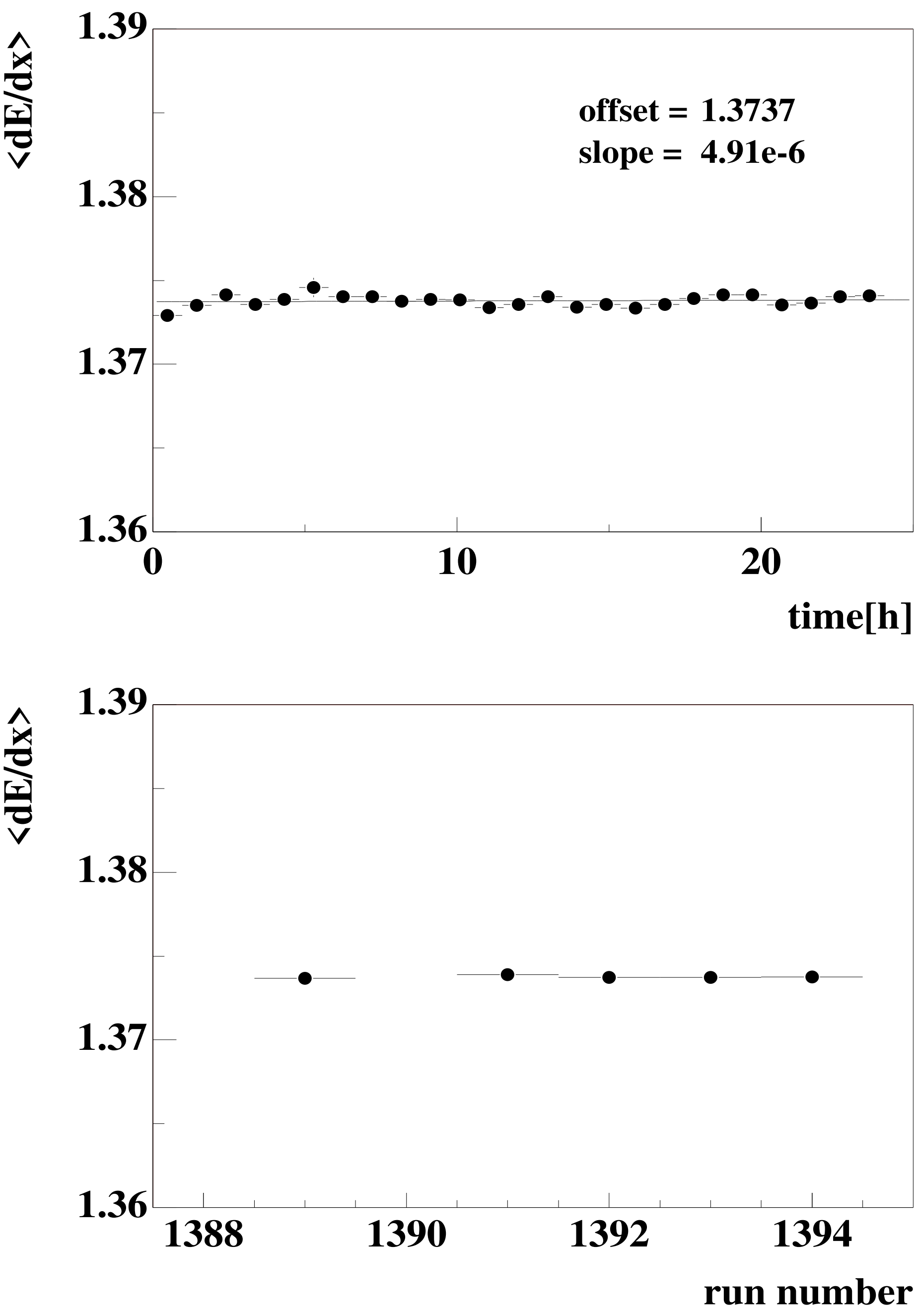

Figure 4.28 Time stability of the dE/dx-measurement.
Top panel: Average dE/dx per event plotted against the time [h] of the event.
Bottom panel: Average dE/dx per event plotted against run number.

5 Statistical Tools for Data Analysis

The particle identification in the NA49-experiment relies on a velocity measurement that in combination with the particle momentum yields information about the particle mass. Due to the finite mass resolution of the procedure it is often impossible to uniquely identify particles. Therefore one has to rely on a statistical treatment of the available information. In the following chapter the statistical tools used in this analysis will be introduced.

5.1 The Maximum-Likelihood Method

The usual way of extracting information from the dE/dx-measurement is to bin the data in phase space and to unfold the dE/dx spectra to extract the particle yields (see for example Fig. 5.1). For the treatment of single events however this approach will fail because binning the approximately 1000 particles in the acceptance of the detector will result in too few entries in the bins to successfully extract information by fitting the dE/dx-spectra. Instead the event-by-event analysis of the K/π-ratio in the NA49-experiment follows the approach of maximum-likelihood parameter estimation from unbinned data proposed in [43] and [68].
Random processes are described by a *probability density* which gives the frequency of occurance for each possible outcome. Formally the outcome of a random process is represented by a random variable x, which ranges over all admissible values in the process. The probability of an outcome x of a random process is given by the probability density

function (**PDF**) $P(x)$. The random variable is then said to be *distributed* as $P(x)$.
In the analysis presented here we measure the momentum vector $\mathbf{p}$ and the specific ionization dE/dx, which now represent the random variables of a sampling process. Adopting the formalism of [68] the PDF $P(\mathbf{p}, dE/dx)$ giving the probability of measuring a particle at a given $\mathbf{p}$ and dE/dx can be written as:

$$P(\mathbf{p}, dE/dx) = \sum_{(m)} r^{(m)}(\mathbf{p}) f_p^{(m)}(dE/dx), \tag{5.1}$$

The index (m) denotes the four relevant charged particle types, i.e. e, π, K and p. The form and value of the dE/dx-PDF $f_p^{(m)}(dE/dx)$ is determined by the detector properties, but also depends on the particle momenta (q.v. section 4.1) as indicated by the index p. The yield of the particle species (m) at $\mathbf{p}$ is given by the momentum PDF $r^{(m)}(\mathbf{p})$. In order to fulfill the normalization condition for P the momentum PDF has to be normalized to 1:

$$\sum_{(m)} \int r^{(m)}(\mathbf{p}) d^3p = 1, \tag{5.2}$$

The goal of this analysis is to estimate the functions $r^{(m)}(\mathbf{p})$, which are distributions of a given particle species (m) in momentum space normalized to the relative particle yields. The functional forms of $r^{(m)}(\mathbf{p})$ (e.g. temperatures of transverse momentum spectra) are determined from the inclusive data sample. The unknown parameters to be estimated are relative particle yields, i.e. the parameters of the relative normalization of the $r^{(m)}(\mathbf{p})$. A given set of normalizations functions we will denote as $\Theta^{(m)}$. The parameters will be extracted by fitting the experimental data points. The PDF for a fixed set of parameters $\Theta^{(m)}$ can now be written as:

$$P(\mathbf{p}, dE/dx|\Theta) = \sum_{(m)} r^{(m)}(\mathbf{p}|\Theta) f_p^{(m)}(dE/dx), \tag{5.3}$$

where $\Theta = \Theta^{(m)}$.
To estimate the parameters Θ the maximum-likelihood method is used. Let us assume a set of data points, X, consisting of n measurements $X = \mathbf{p}_1, dE/dx_1, ...\mathbf{p}_n, dE/dx_n$.

The method then consists of calculating the *likelihood*-function (LF),

$$L(X|\Theta) = \prod_{i=1}^{n} P(\mathbf{p}_i, dE/dx_i|\Theta), \tag{5.4}$$

which can be recognized as the probability of observing the set of measurements X given the PDF for a fixed set of the parameters Θ. Treating the measurements X as constants and the parameters Θ as variables in the LF now allows for choosing as an estimate of parameters Θ a particular $\hat{\Theta}$ which renders L as large as possible. Instead of maximizing $L(X|\Theta)$ it is more convenient for technical reasons to minimize the auxiliary function, $l(X|\Theta)$, defined as:

$$l(X|\Theta) = -\sum_{i=1}^{n} ln[P(\mathbf{p}_i, dE/dx_i|\Theta)]. \tag{5.5}$$

Practically this means the K/π ratio for a given event is estimated by assuming a K/π ratio (i.e. setting the relative yields of the particles by the parameters Θ) in the PDF and calculating the probability of measuring this event. Varying the K/π ratio in the PDF and repeating the probability calculation we can now find a K/π ratio that is "most likely" for the given event. Fig. 5.2 shows the PDF derived from the inclusive data set (top panel) and a set of **p** and dE/dx measurements corresponding to a single event (lower panel). The four bands of boxes represent electrons, pions, kaons and protons in top to bottom order. The size of the boxes at a given **p** and dE/dx bin gives the probability density at this point. The fit is performed by changing the relative normalization of the bands representing the different particle species. The uncertainty of this method of parameter estimation will be discussed in section 5.4.

Determination of the Probability-Density-Function

The PDF to be used for the event-by-event fit of the K/π-ratio is derived by analyzing the inclusive distributions measured in a data set of about 100k events. One problem that arises in the determination of the PDF is that the measured momentum distributions are limited by the acceptance of the detector. As a consequence the momentum distributions are not smooth functions anymore and cannot be parametrized by simple analytical functions. To account for this problem in the analysis presented here a look-up table is used as PDF instead of analytical functions. To create this look-up table the particle sample from about 100k events is broken up in bins in momentum space and for each bin a dE/dx-spectrum is generated. Each of the dE/dx-spectra is then unfolded by fitting the distribution with four Gaussians of the same relative width. Fig. 5.1 shows an example spectrum and the functions fitted to extract the information.

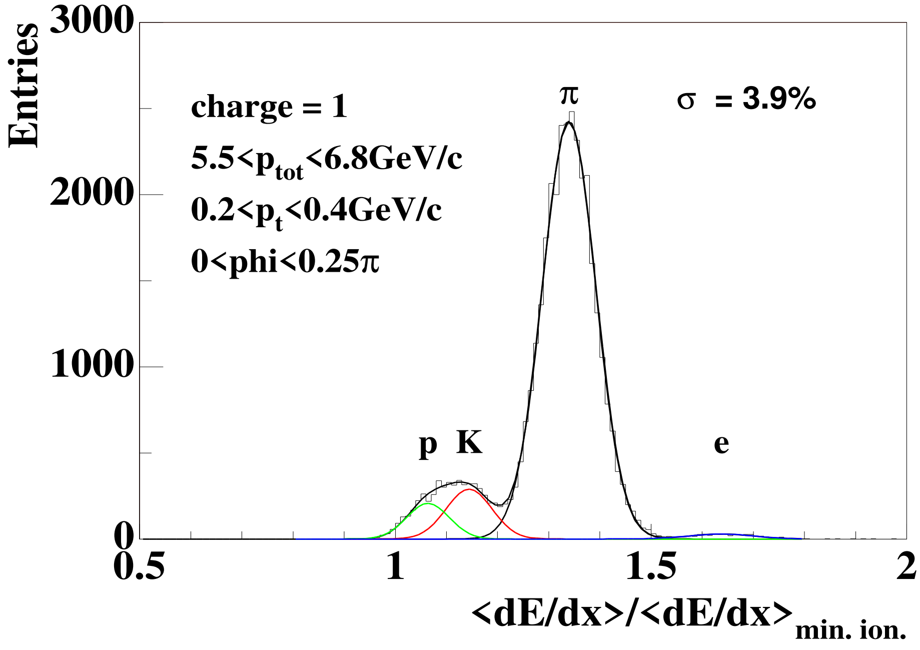

Figure 5.1 Example dE/dx-Spectrum used for generating of the probability density function look-up table.

The fit of each spectrum contains the information on the particle yields in the given bin needed for the momentum PDF and also the dE/dx-resolution and dE/dx-value of the different particle species used as input for the dE/dx-PDF. A proper normalization of the spectra according the equ. 5.2 automatically yields the PDF for the event-by-event K/π-fit. Fig. 5.2 shows the PDF derived from fitting of the dE/dx spectra. For illustration purposes the yield of each particle species is normalized to unity in this figure.

This method was found to be superior to an analytic parametrization of the PDF because the remaining deficiencies of the calibration and also the observed resolution achieved with the detector depend more on the geometric position of a given particle within the detector than on its location in momentum space. These effects are easier taken into account by a fine binning of momentum space and treating the different momentum bins independently than by modelling an analytic function. The parameter range and number of bins used for this analysis is given in table 5.1

variable	range	bins
$charge$	$-1, +1$	2
p_{tot}	$2 - 120GeV/c$	20
p_t	$0 - 2GeV/c$	10
phi	$0 - 2\pi$	8

Table 5.1 Binning used for the look-up table of the Probability Density Function.

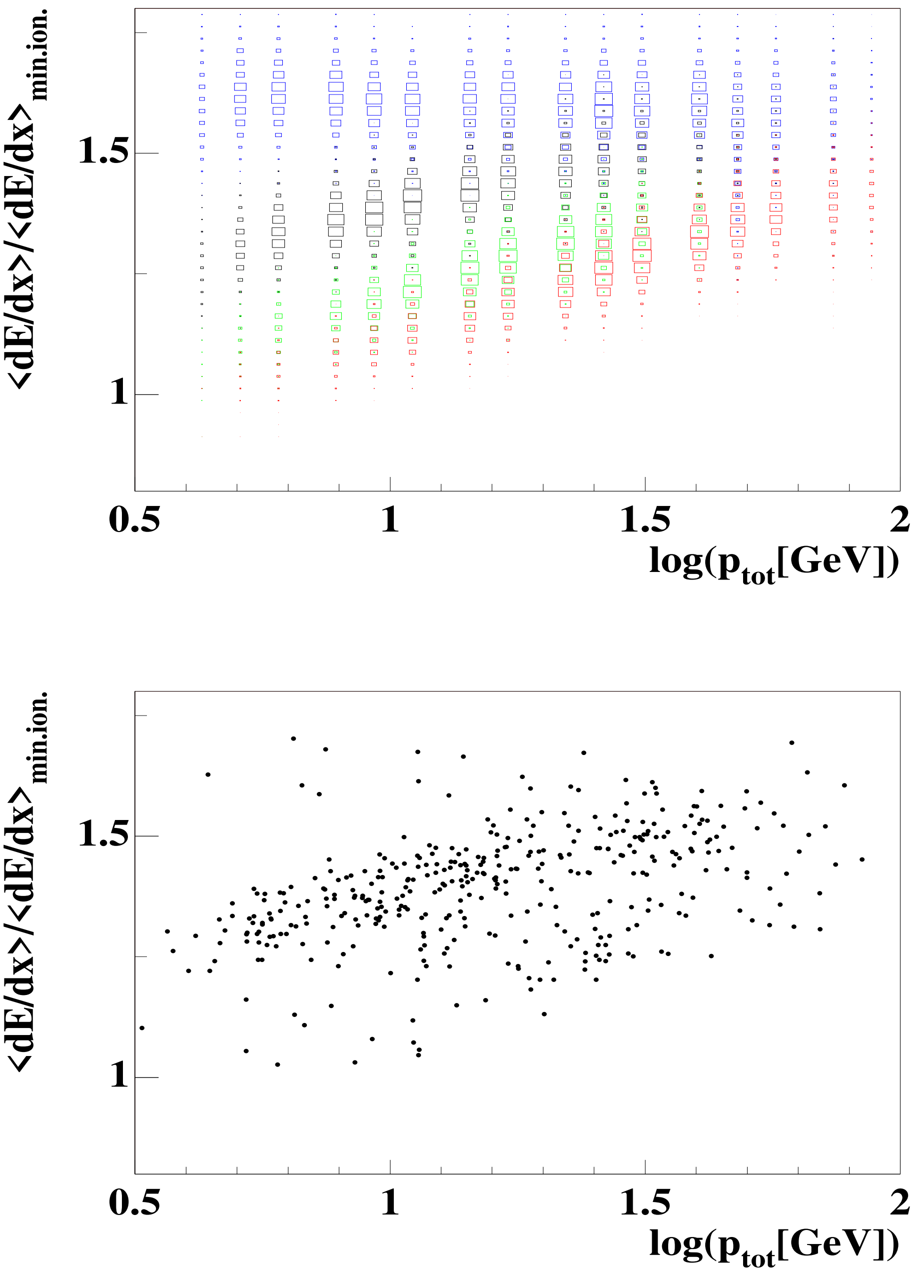

Figure 5.2 Top Panel: Probability Density Function derived from fitting of the dE/dx spectra in phase space bins. The yield of each particle species is normalized to 1. The box size gives the probability of measuring a particle in a given dE/dx and total momentum p_{tot} bin. Bottom Panel: dE/dx and p_{tot} measurements of a single central Pb+Pb event.

Evaluation of Parameters

The actual estimation of the event-by-event K/π-ratio is done by using the numerical minimization procedures of the MINUIT package of the CERN-library [60]. The unknown parameters Θ to be fitted as defined above are further reduced to only the relative yields of the given particle species. The momentum distributions contained within the look-up table of the PDF are assumed to have the same shape for different K/π-ratios measured. Fig. 5.3 shows the event-by-event distribution of the K/π-ratio determined by this method. The mean of the distribution pertains to a limited region of

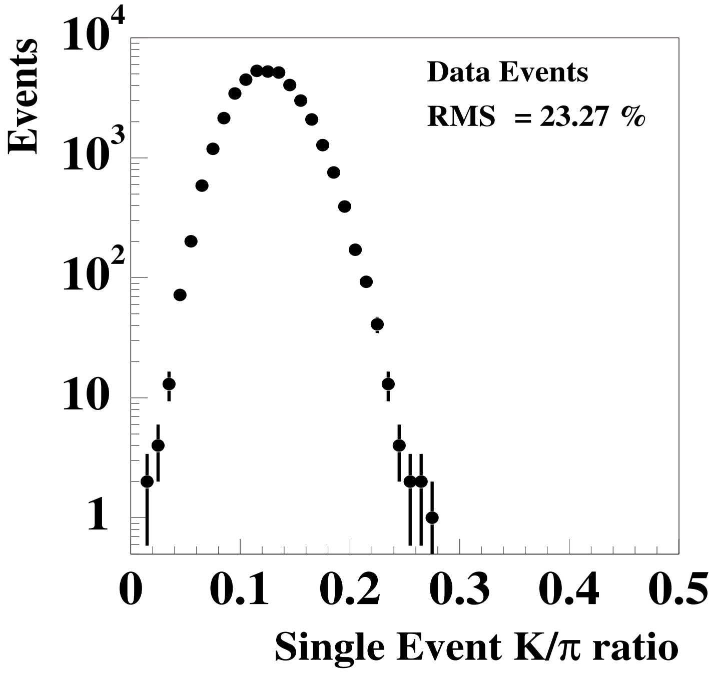

Figure 5.3 Event-by-event K/π-ratio.

phase space and will in general differ from the K/π-ratio determined in full phase space because the acceptance of the MTPCs does not cover the same phase space region for pions and kaons (see Fig. 6.1).

5.2 Event-Mixing

To estimate the amount of dynamical fluctuations in the distribution of an event-by-event observable it is important to have reference events where only statistical fluctuations are present. The method of event mixing has proved very usefull in producing artificial events with statistical variations from event to event. To create mixed events first a track pool ("event-mixer") is filled with the tracks of several events. Mixed events are generated by randomly drawing numbers of particles from the track pool according to the multiplicity distribution of real events. Only one track of any original event is used in a given mixed event to avoid correlations present in the real events feeding into the mixed events. Since the mixed events are random samples from the same inclusive track population they will also reproduce the phase space distributions of the real events. By construction the mixed events have the same single particle distributions as the real events, but no internal correlations. The event-by-event distribution of the K/π-ratio for a set of mixed events can now be derived by the same parameter estimation algorithm as for the real events. The resulting distribution is shown in Fig. 5.4. This represents the distribution of the eventwise K/π ratio for indepentently produced kaons and pions.

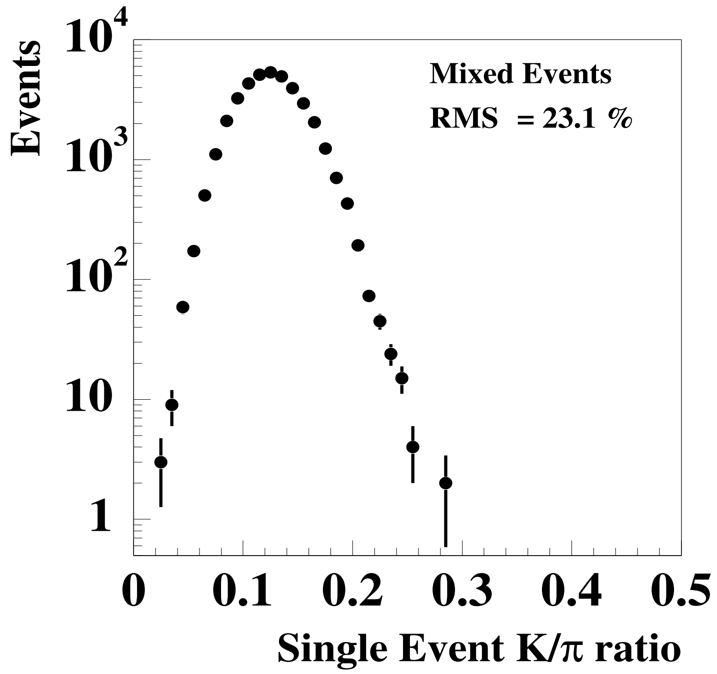

Figure 5.4 Mixed events reference distribution of the event-by-event K/π ratio

5.3 Systematics of the Parameter Estimation

To test the systematic behavior of the parameter estimation it is desirable to generate mixed events with a known K/π-ratio. Such events can be constructed by employing four event-mixers, each containing only particles of a known species, and drawing a certain number of particles from each mixer. Since a unique identification of particles is in general not possible, the filling of the mixers has to rely on a statistical process.
Given the measured momentum and ionization of a particle the probablity of this particle being of a certain species can be calculated. By randomly drawing particles from the complete track sample according to their probability and storing them in the separate event mixers samples of tracks identifiable as a certain particle species can be generated. By construction the track population within an event mixer for a certain particle species will be distributed according to the PDF of this species.
Fig. 5.5 shows the dE/dx spectra generated from the data sample and from the separate event mixers in the same phase space bin. The distributions show that it is possible to statistically distribute the data sample into separate event mixers each representing a given particle species. From the separate track pools one can construct mixed events with known preset particle ratios in order to test the response of the event-by-event fit of the K/π-ratio. Also artificial fluctuations can be introduced to events generated by this method in order to estimate the sensitivity of the event-by-event K/π fit to a certain fluctuation model.

5.4 Performance of the Event-by-Event K/π-Fit

The uncertainty of the eventwise estimation of the K/π-ratio can be evaluated by constructing mixed events with a fixed preset K/π-ratio. This method by construction takes into account the effects of the limited acceptance and particle identification while the finite number fluctuations are eliminated from the measurement. Fig. 5.6 shows the eventwise K/π-ratio distribution derived from mixed events all constructed with the same K/π-ratio of 0.13. The width of 16.7% of this distribution serves as an estimate of the uncertainty of the fit procedure.

To evaluate the width of the measured event-by-event distribution of the K/π-ratio it is necessary to ensure a linear response of the fit to a varying K/π-ratio in the data. This is tested by constructing mixed event with a varying K/π-ratio by the method described above. The response of the fit-algorithm is shown in Fig. 5.7. The test shows a linear response of the fitting procedure. The correlation coefficient of the fit response to the input indicated by the slope of the straight-line shown in the figure is 1.02.

The trivial fluctuations due to finite number statistics can be estimated to lead to a

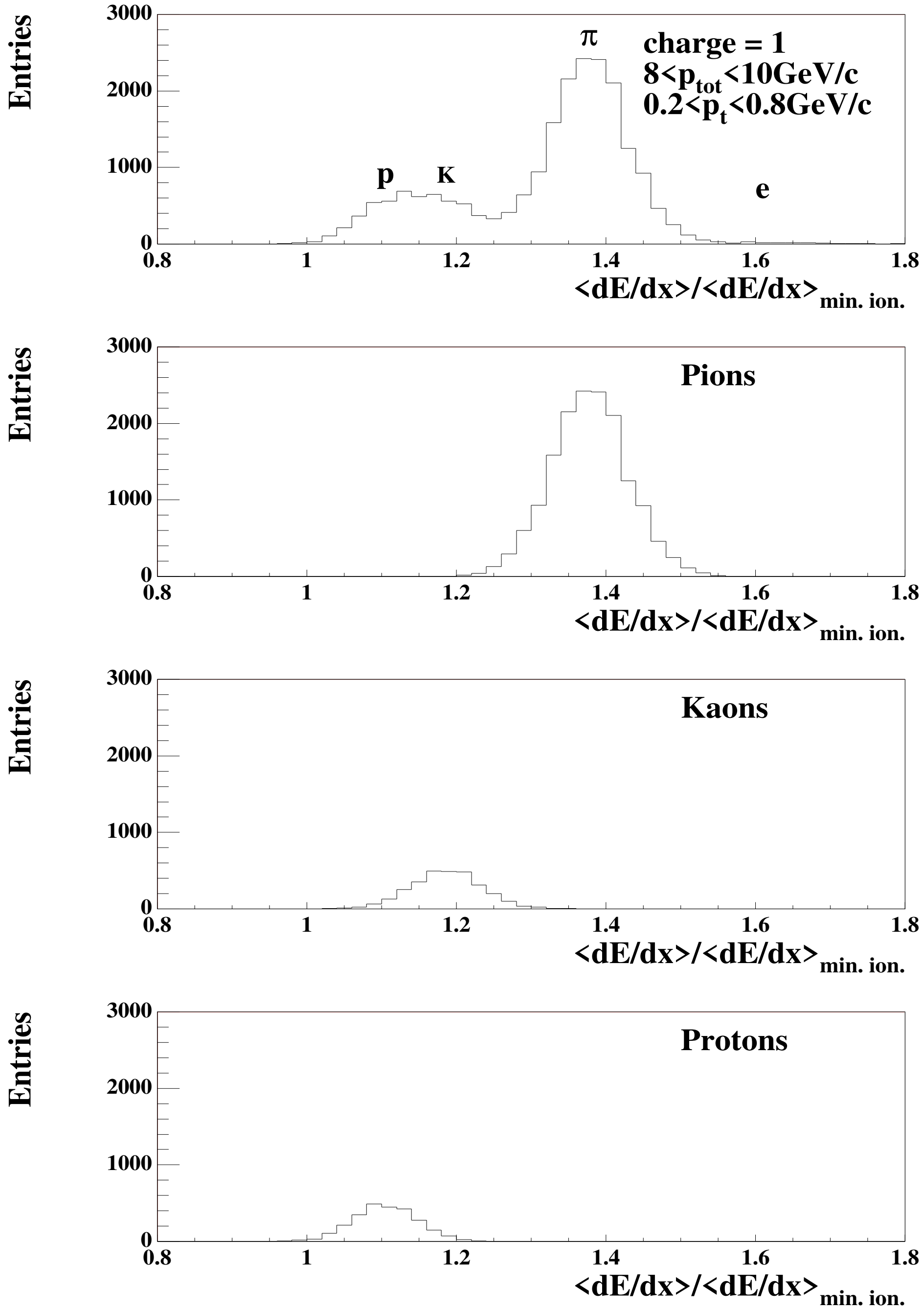

Figure 5.5 Example dE/dx spectra generated from data and from event mixers containing only particles identifiable as one particles species.

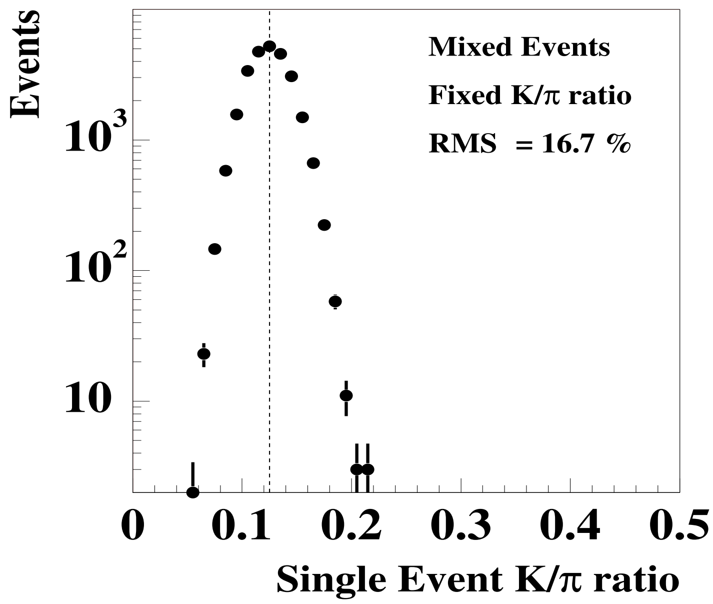

Figure 5.6 Uncertainty of the event-by-event fit of the K/π-ratio tested by mixed events with a fixed K/π-ratio of 0.125. The vertical line indicates the input K/π-ratio. The width of the distribution corresponds to the uncertainty of fit.

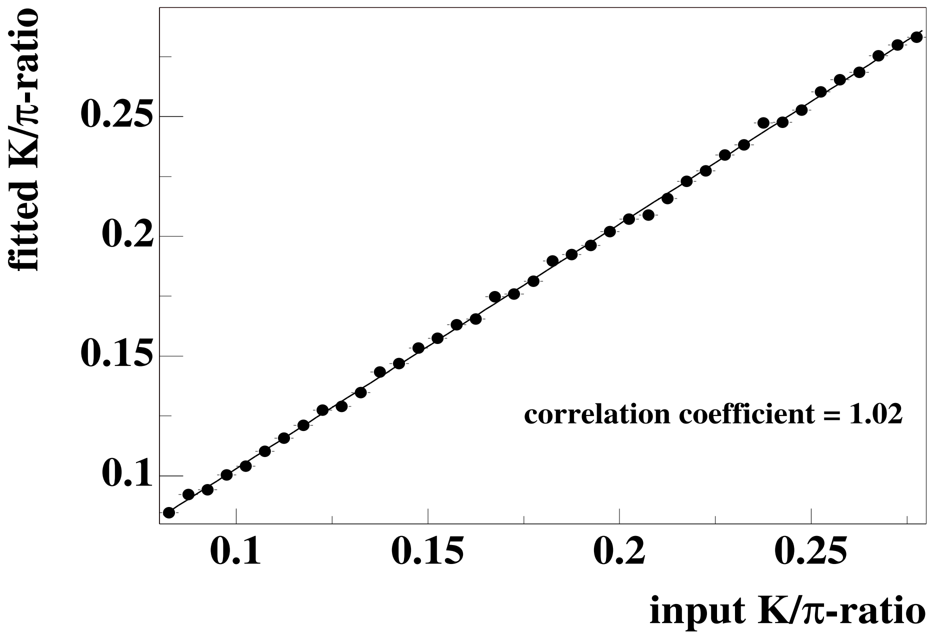

Figure 5.7 Response of the event-by-event K/π fit to variation of the input K/π ratio in simulated events.

width of 15.9%. The contribution due to finite number fluctuations is dominated by the fluctuation in the small number of kaons (about 40) compared to the large number of pions (about 310) per event. The combination of trivial statistical fluctuations and the experimental resolution fully exhausts the width observed in the mixed events. In order to estimate how much of the difference in width observed in real events compared to mixed events can be attributed to dynamical fluctuations it is necessary to further study the systematic behaviour of the method. Event-by-event variations in the mass measurement could cause fluctuations in the data sample that could not be observed in the mixed event sample. These effects can also be simulated by the method described above.

Previous analysis showed that variations in chamber gain and track density dependences of the mass measurement can cause apparent fluctuations in the event-by-event fit of the K/π-ratio. Fig. 5.8 shows the response of the fit method to variations in the total chamber gain, simulated by scaling the dE/dx values of all tracks in a given simulated event by the value indicated in the figure. A variation of the chamber gain will shift the dE/dx-measurement of a single event relative to the inclusive distribution. Since the inclusive distribution is used to derive the probability density function a shift in chamber gain will lead to a misidentification of particles and thus will lead to wrong estimation of the K/π-ratio of the given event. The strong dependence illustrated in this figure shows the need for a very stable ionization measurement in order to be sensitive to fluctuations in the real data.

The track density effects of the dE/dx measurement are simulated in a similar fashion by scaling the dE/dx values of the particles measured in the high-density region depending on the event multiplicity. The result of this study is illustrated in Fig. 5.9.

The combination of the observed dependences with the achieved stability of the dE/dx measurement documented in chapter 4 allows us to estimate the systematic uncertainty in the measurement of the event-by-event fluctuations of the K/π ratio to 2%. Note, however, that variations in the dE/dx measurement will increase only the width of real events and not mixed events, since there the correlation between event multiplicity and dE/dx will not be present. Thus variations of the dE/dx measurement will fake a fluctuation signal but can not reduce it.

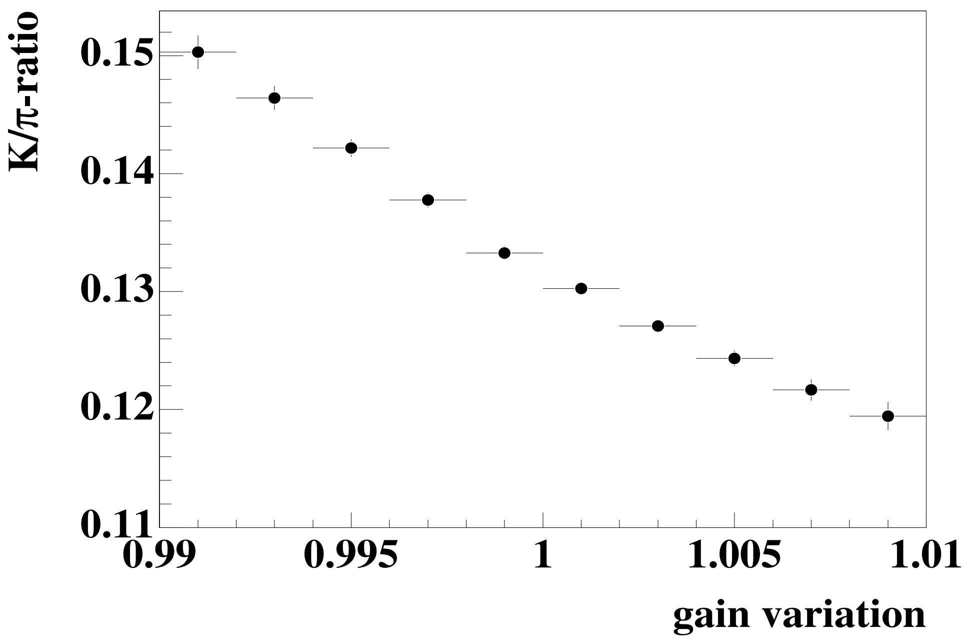

Figure 5.8 Influence of variations of the chamber gain on the event-by-event measurement of the K/π-ratio.

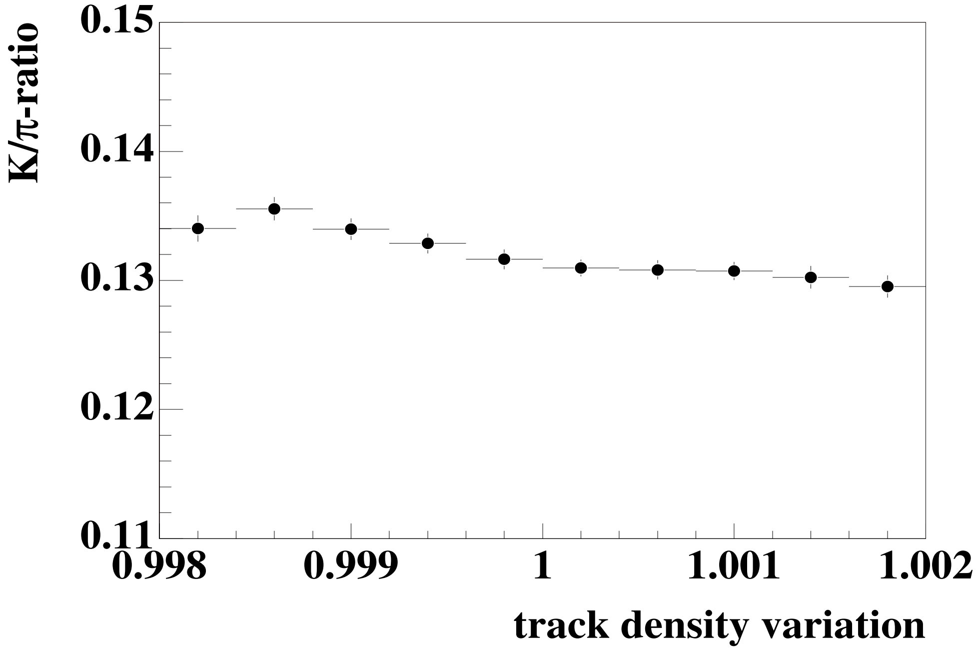

Figure 5.9 Response of the event-by-event K/π fit to a simulation of the multiplicity dependence of the dE/dx measurement.

6 Event-by-Event Fluctuations of the K/π-Ratio

6.1 Data Sample, Event and Track Selection

The analysis presented here is based on a sample of 40000 central Pb+Pb events from the 1996 data taking period. The events are selected online for centrality by the trigger on the veto calorimeter. For this data set the 5% most central events were selected, which corresponds to less than $3.5 fm$ impact parameter [9].
In order to obtain a clean sample of well defined tracks the following cuts were used:

- Tracks identified as bad tracks by the quality assurance algorithm introduced in chapter 3.2 are rejected.

- Vertex tracks are selected by extrapolating the trajectories of good tracks back to the target plane and by calculating their intersection point with this plane. Tracks with a distance to the vertex larger than 4 cm in x or 0.5 cm in y are rejected. This cut rejects a large fraction of decay products of long lived neutral particles as well as badly reconstructed vertex tracks.

- Only tracks that have at least 30 points in the MTPC are used in order to ensure enough samples of the tracks ionization to allow for a reliable particle identification.

- In order to reject tracks visible in the MTPC originating from γ conversions, secondary interactions and decays between VT2 and MTPC, only tracks are used that have a found track match in the VTPC if the particles trajectory traverses the VTPC.

The fraction of all measured tracks rejected by the different cuts is summarized in table 6.1. The percentage quoted gives the fraction of tracks remaining after subsequently applying the track cuts.

selection	number/event	fraction
good	1154.2	100%
vertex	691.1	59.9%
dE/dx	431.7	37.4%
MTPC	417.4	36.2%

Table 6.1 Number of tracks per event usable for the event-by-event K/π-fit. The quoted percentage gives the fraction of tracks remaining after subsequently applying the track cuts.

The selection of tracks results in a limited acceptance for the different particle species. Fig. 6.1 shows the phase space occupation within the acceptance for pions (top panel) and kaons (bottom panel). Note that the acceptance for pions and kaons is different. The particle ratios studied in this analysis are not corrected for acceptance and thus will differ from the value extrapolated to full phase space. The application of a fixed extrapolation factor would obviously not change the amount of fluctuations observed in the data. Systematic studies of the inclusive yields of identified particles extrapolated to full phase space can be found in [61].

Fig. 6.2 shows the event-by-event multiplicity distribution after the track selection. Note that the width of the distribution is bigger than expected for a Poissonian distribution due to the large range of impact parameter accepted by the NA49 trigger. This fluctuation cancels however when examining intensive quantities like the K/π ratio relative to mixed events (see chapter 5.2).

6.2 Results

Combining the information gained about the systematics of the fit procedure discussed in chapter 5.3, the width of distribution of the event-by-event K/π ratio in mixed events, representing an event sample containing only statistical fluctuations can be understood as a combination of two different effects,

1. finite number statistics $\sigma = 15.9\%$.
2. experimental resolution $\sigma = 16.7\%$.

The width due to these two effects quadratically adds up to the width of 23% observed for the mixed event sample. The amount of dynamical fluctuations present in the data is estimated by comparing the width of the event-by-event K/π distribution of the data events to the corresponding distributions generated from mixed events. Fig. 6.3 shows an overlay of the data distribution (symbols) and the mixed event distribution (solid

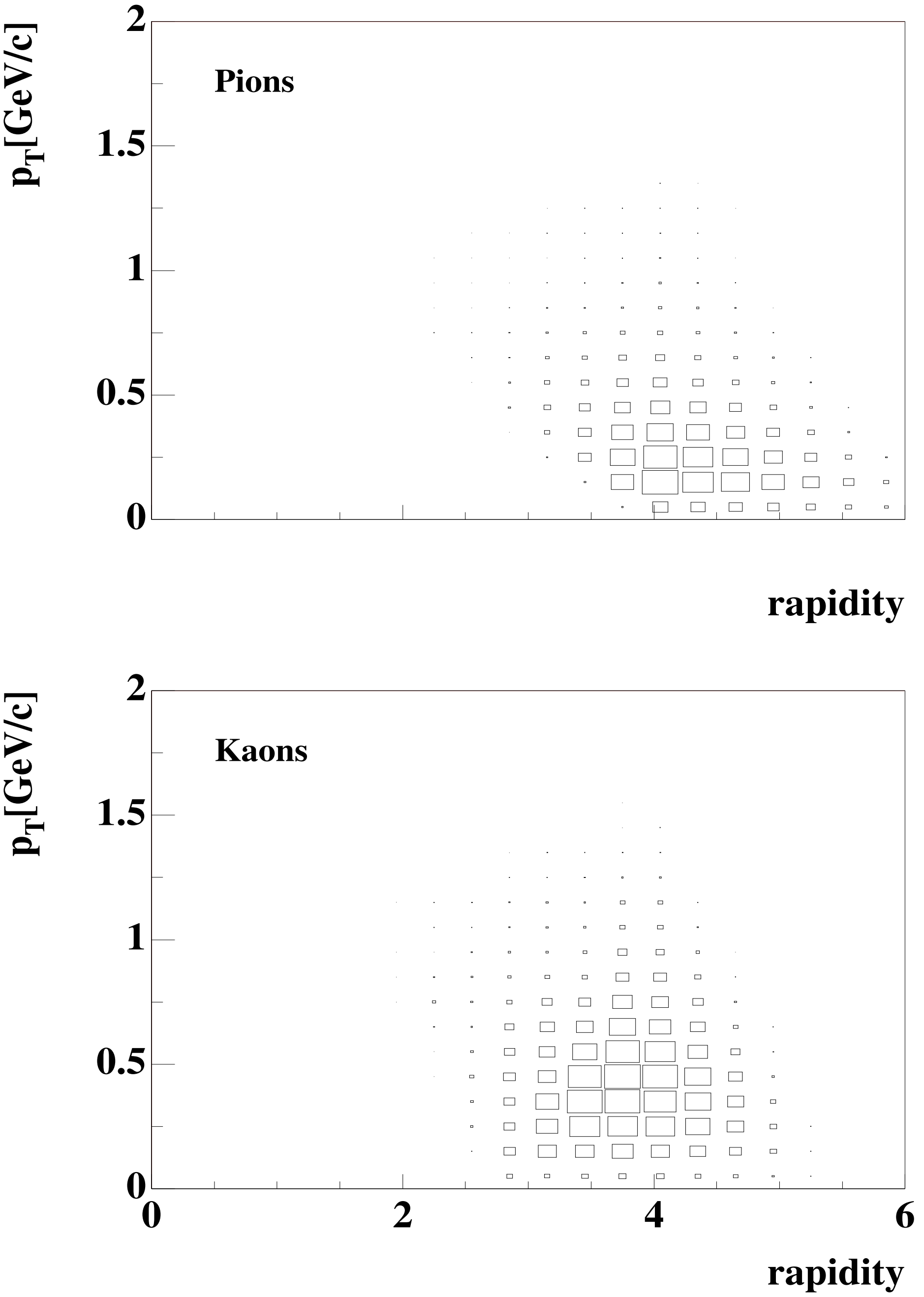

Figure 6.1 Phase space occupation of particles within the MTPC-acceptance.
Top panel: Identified pions.
Bottom panel: Identified kaons.

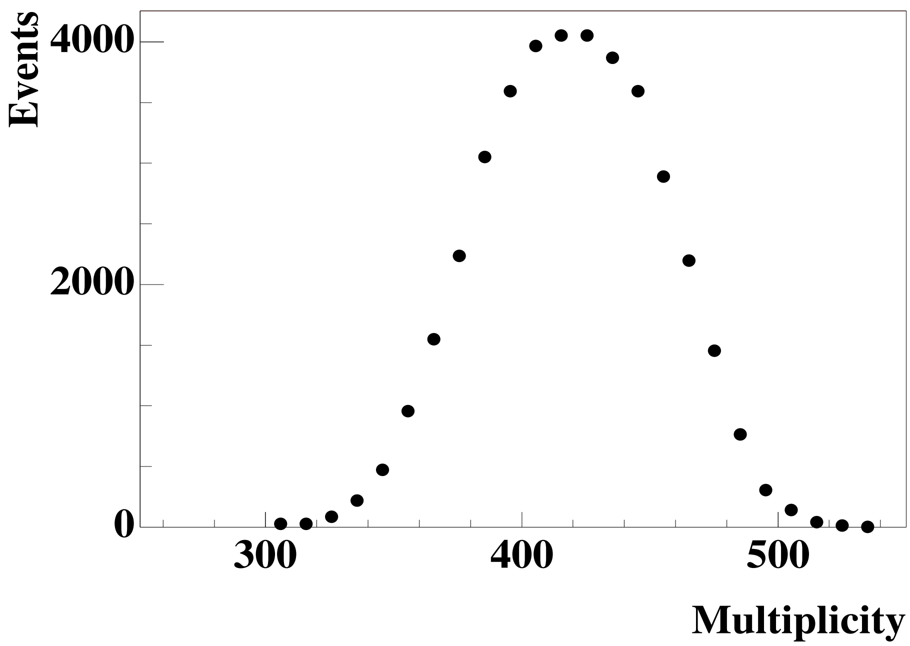

Figure 6.2 Event-by-event multiplicity distribution of tracks used for the K/π fit

line). It is immediately evident that the difference in width is small. The objective of this thesis is to quantify this difference. Therefor we define a measure for the dynamical fluctuations σ_{dyn}, defined as follows:

$$\sigma^2_{dyn} \equiv \sigma^2_{data} - \sigma^2_{mixed}. \tag{6.1}$$

From the difference in width of the distributions, a contribution of dynamical fluctuations of $\sigma_{dyn} = 2.8\%$ is obtained for central Pb+Pb events at the SPS. The statistical error of the measurement is estimated to be $\pm 0.5\%$.

Sensitivity and Systematical Errors

In order to test the sensitivity of this method to dynamical fluctuations present in the data, a simple fluctuation model is used to impose artificial fluctuations on mixed events and to study the response of the parameter estimation. For this test a simple Gaussian fluctuation model is used. Each mixed event is constructed with the K/π-ratio of the inclusive distribution scaled by a random number generated from a Gaussian probability density function. Fig. 6.4 shows 3 examples of the input fluctuation. This simulation containing a known fluctuation is now used to check which amplitude of fluctuations produces a signal corresponding to the signal observed in the data. Fig. 6.5 shows the increase in width of the event-by-event K/π-ratio as a function of the amplitude

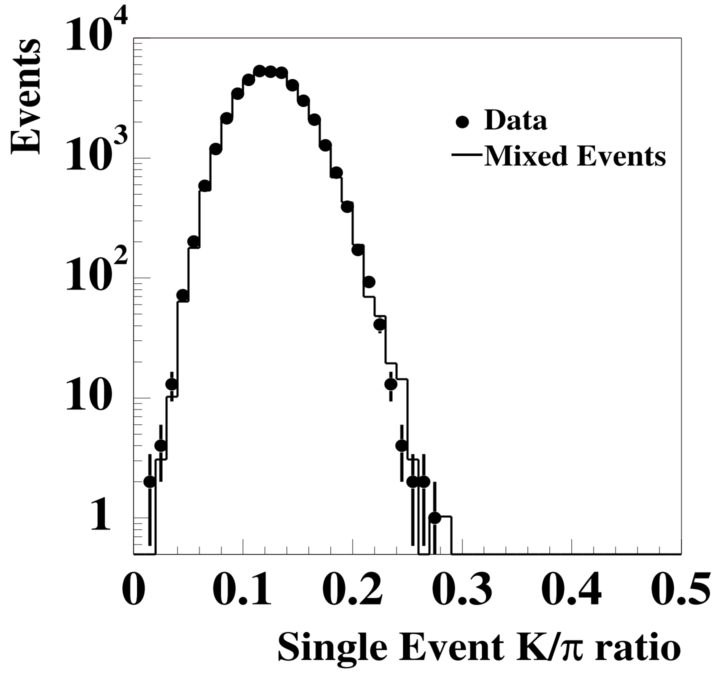

Figure 6.3 Event-by-event distribution of the K/π-ratio (points). For comparison, the solid line shows the K/π-ratio distribution for mixed events.

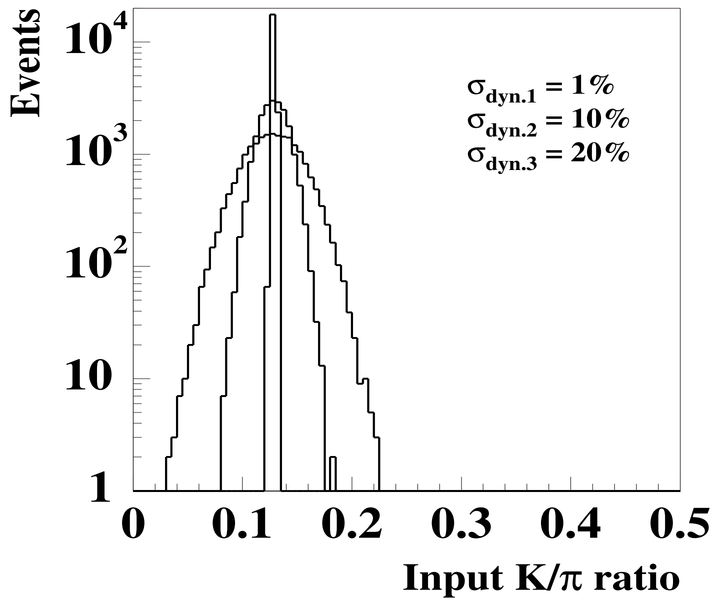

Figure 6.4 Input fluctuations to the sensitivity test. Three distributions are shown for $\sigma_{fluc} = 1\%, 10\%, 20\%$.

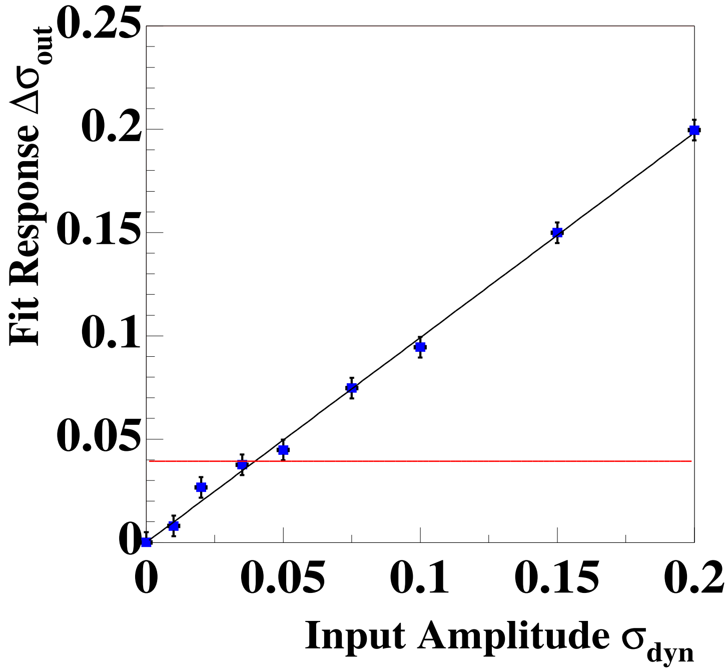

Figure 6.5 Response of the event-by-event K/π fit to simulated events containing input fluctuations of a known amplitude σ_{dyn}.

σ_{dyn} of the input fluctuation. The horizontal line corresponds to values excluded by the fluctuation signal of $\sigma_{dyn,data} = 2.8\% \pm 0.5\%$ in the data at 90% confidence level. The method of estimating dynamical fluctuations shows a linear response to input fluctuations as indicated by the line in the figure. This simulation procedure can also be used to establish limits on fluctuations of the amlitude σ_{dyn} that occur only in a fraction F of all events. Varying the frequency of occurrence of the input fluctuation we can determine the exclusion region shown in Fig. 6.6, where the relative frequency F of events exhibiting fluctuations of amplitude σ_{dyn} is plotted versus σ_{dyn}. We see that for F=1 fluctuations of a relative amplitude $\sigma_{dyn} > 4.0\%$ are ruled out at 90% confidence level, whereas fluctuations occurring in 5% of the events can only be ruled out for $\sigma_{dyn} > 15\%$.

Dynamical flucuations

In order to understand the relevance of dynamical fluctuations observed in the data it is necessary to first identify possible reasons for dynamical fluctuations and to study their effect on the event-by-event observable.

A major source of non-statistical behaviour of the event-by-event K/π distributions is the correlated production of kaons and pions. In order to illustrate this effect Fig. 6.7 shows the result of some simple simulations of correlated particle production. Panel a)

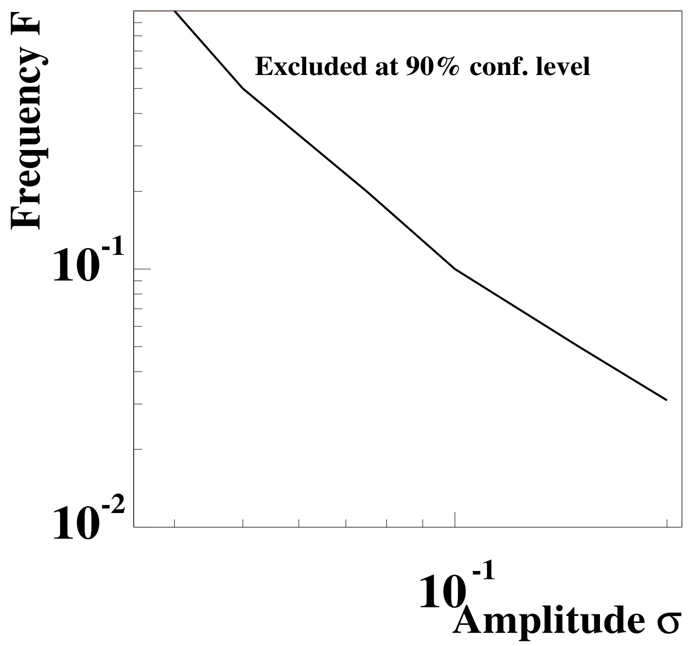

Figure 6.6 Limit on the amplitude of dynamical K/π-fluctuations as a function of the frequency of events showing the fluctuation.

shows the event-by-event K/π distribution of events constructed by randomly generating 500 particles with equal probability of being a kaon or a pion. To this sample 250 *pairs of kaons* and *pions* are added simulating a correlated production of kaons and pions. Comparing the event-by-event K/π ratio distribution of these events to mixed events generated from the same event sample shows that correlated production of kaons and pions results in a narrower distribution for the input events than for the mixed events.
The effect of an anti-correlation is simulated by again randomly generating 500 particles and adding 250 pairs of particles of the same type, choosing randomly if the pair is a pair of kaons or a pair of pions with equal probability. The resulting distributions shown in panel b) indicate an increase in width of the input distribution compared to the mixed event sample.
The third toy simulation shown in panel c) illustrates the effect of critical fluctuations on the event-by-event distributions. In this simulation two classes of events are generated by randomly generating 1000 particles with different probabilities of being kaons or pions the probabilities depending on the class of the event. The shift of the mean of the separate event classes leads to an increase of the width of the event-by-event distribution compared to the mixed event distribution.

Physical origins for correlated particle production are for example decays of resonances and Bose-Einstein statistics. However there is no information on these effects available in the data on an event-by-event basis, so the contribution to the signal of dynamical fluctuations has to be estimated by comparisons to model predictions. An extensive

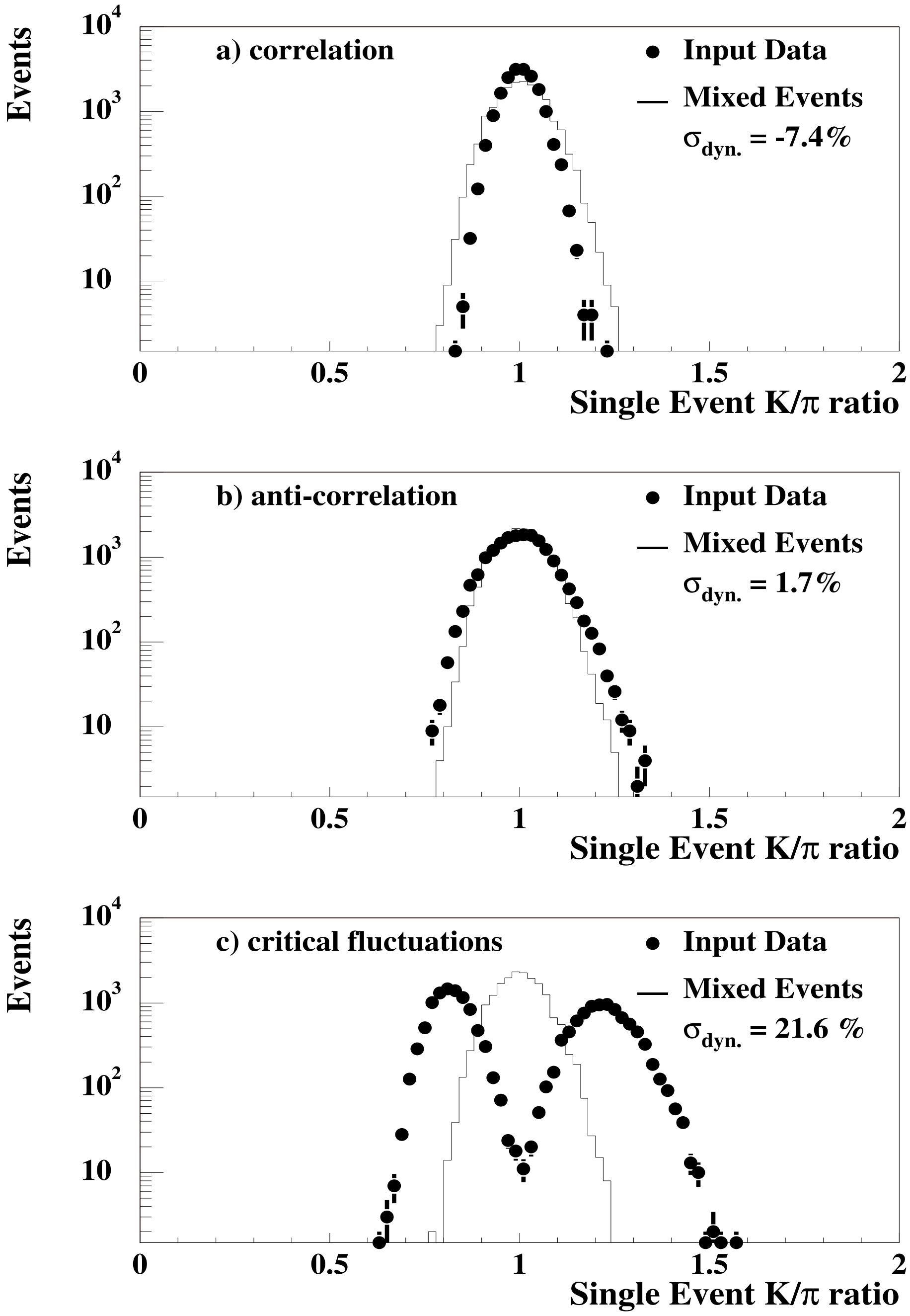

Figure 6.7 Simulation of the effect of non-statistical fluctuations on the event-by-event distribution of the K/π ratio.
a) Correlated production of kaons and pions.
b) Anti-correlated production of kaons and pions.
c) Critical fluctuations.

discussion of the effects of Bose-Einstein statistics and resonance decays on chemical fluctuations can be found in [15, 72].

6.3 Critical Phenomena

Comparing the event-by-event distribution of the K/π-ratio to a reference containing purely statistical fluctuations only, represented by the mixed event distribution, as shown in Fig. 6.3 it becomes evident that the data matches a statistical sample quite closely in shape as well as in width. For large values of the K/π ratio the data distribution shows no outliers relative to the expectations given by the mixed event distribution on a level of $4 \cdot 10^4$ events. Taking the achieved resolution of 23.1% into account a twofold enhancement of the K/π ratio, as was proposed as a signal for events exhibiting critical behaviour, can be ruled out with high statistical significance. A limit for the probability of occurrence of critical events p_{crit} with $\lambda_s > 0.6$ can be set at:

$$p_{crit} < 0.1\% \quad \text{at} \quad 90\% \quad \text{confidence level.}$$

The data therefore indicate a unique freeze out condition common to all events.

6.4 String-Hadronic Models

The main assumption made in string-hadronic models simulating nucleus-nucleus collisions is the binary approximation in which a nucleus-nucleus collisions is decomposed into binary nucleon-nucleon collisions. As an example of a microscopic model the obtained results are compared to those of FRITIOF - 7.02 which is based on a quark-gluon-string model [69]. In FRITIOF - 7.02 a longitudinally exited state is formed, i.e. a string between a single valence quark and the corresponding diquark of the interacting nucleon is stretched. The string is fragmented into hadrons by breakage.

The hadronization process by string breaking features a mechanism of correlated hadron production since in each binary collision conservation laws (e.g strangeness, energy, etc.) have to be fullfilled locally. The local influence of conservation laws within the extended source volume created in heavy ion collisions should lead to dynamical fluctuations of the flavor content of the final state.

To illustrate this statement with experimental data [70, 28], Fig. 6.8 shows the ratio of the mean K^0_S multiplicity to the multiplicity of negatively charged hadrons, n_-, as a function of n_- for p+p interactions at 200 GeV/c. The data show that the K^0_S multiplicity decreases significantly with the event multiplicity. A similar correlation can be expected for the multiplicity of charged kaons. This means that the probability that a

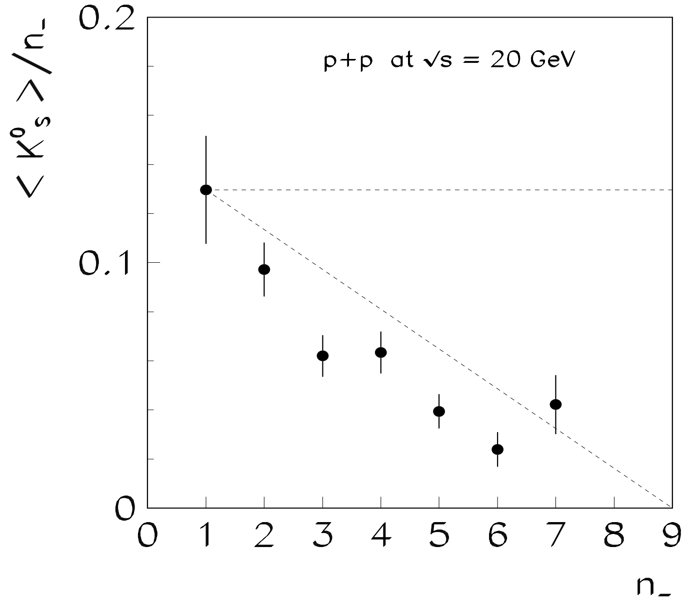

Figure 6.8 The dependence of the ratio $< K_S^0 > /n_-$ on negative hadron multiplicity, n_-, for p+p interactions at $\sqrt{s} = 20GeV$

charged hadron is a kaon depends on the multiplicity of the collision. Thus particles are not produced independently and therefore we expect to see large non-statistical fluctuations in the chemical composition of p+p collisions or in Pb+Pb collisions if they have to fulfill conservation laws locally.
In order to study this effect the analysis of the event-by-event K/π ratio was performed on a sample of 40k Pb+Pb collisions simulated by the FRITIOF model and 40k events produced with the HIJING model [71] which also by construction locally fulfills the conservation laws.

The analysis of simulated events does not contain the effect of the experimental resolution, since there is no need for particle identification. The effects of finite number statistics and acceptance are considered in the analysis by only selecting particles that would fall into the acceptance region of the MTPC. The amount of dynamical fluctuations of the K/π ratio present in the data samples generated with these models was found to be:

$$\begin{array}{lcl} \sigma_{dyn.}^{FRITIOF} & \rightarrow & 11.7\% \pm 0.5\% \\ \sigma_{dyn.}^{HIJING} & \rightarrow & 7.5\% \pm 0.5\% \end{array}$$

The event-by-event K/π ratio distributions derived from the event samples generated with these models are shown in Fig. 6.9 and 6.10.
The dynamical fluctuations observed in Pb+Pb collisions of 2.8% are significantly lower than those in string hadronic models. This suggests that the correlations due to the local

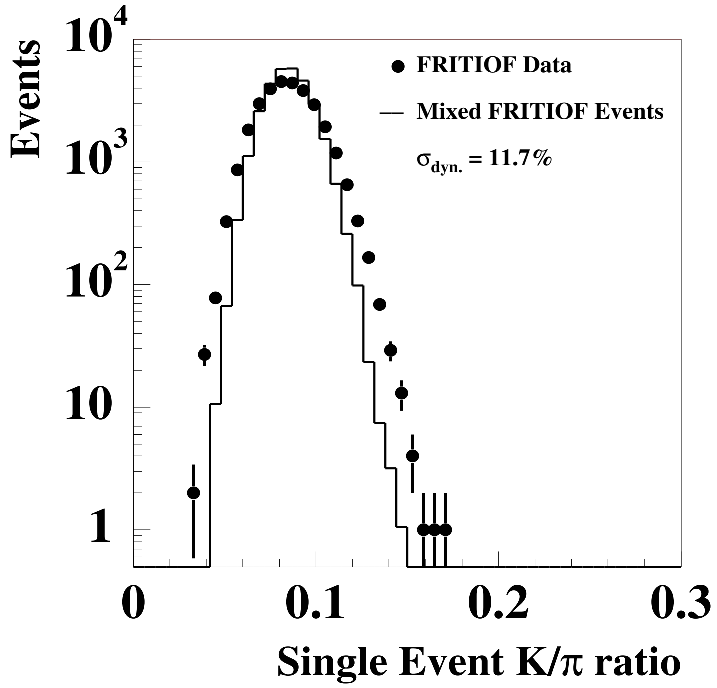

Figure 6.9 Event-by-event K/π-ratio distribution for the FRITIOF model and the corresponding mixed event distribution.

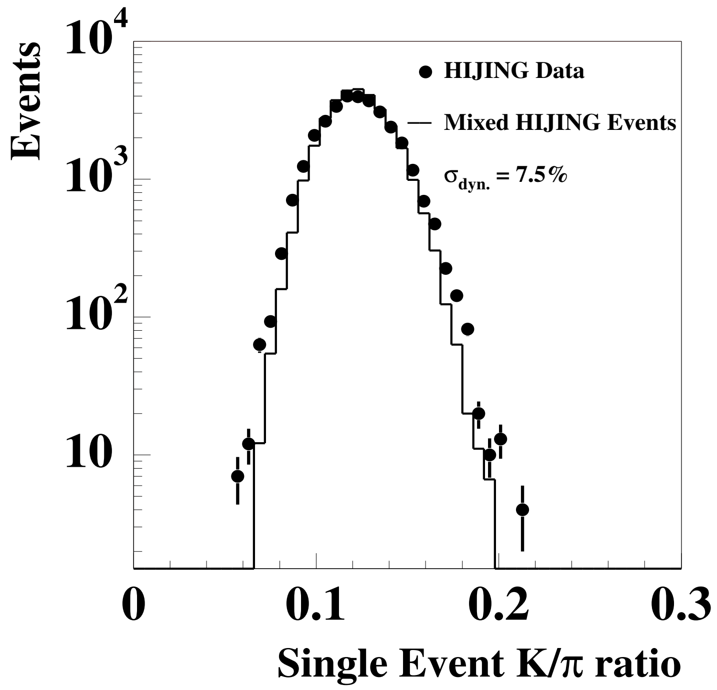

Figure 6.10 Event-by-event K/π-ratio distribution for the HIJING model and the corresponding mixed event distribution.

influence of conservation laws are not present in the data, which leads to the conclusion that a different process of hadronization has to be assumed or that the correlations are destroyed after hadronization e.g. in a rescattering process (see below).

6.5 Hadronic Rescattering

The influence of rescattering of produced particles after hadronisation on the observed fluctuation pattern has been studied with the UrQMD model [74, 75]. Even though the crossections for strangeness producing and annihilating processes are small, inelastic scattering can possibly reduce a fluctuation signal originating from local conservation laws.
The UrQMD model is also a microscopic model based on string exitation, but includes inelastic rescattering of particles after the hadronization process. Fig. 6.11 shows the event-by-event K/π-ratio distributions obtained from the UrQMD model with rescattering. The data obtained without rescattering are shown in Fig. 6.12. For the different datasets the following fluctuation signal σ_{dyn} can be derived:

- UrQMD with rescattering: $\sigma_{dyn} = 3.6\%$
- UrQMD without rescattering: $\sigma_{dyn} = 7.5\%$

Hadronic rescattering shows a significant change in the fluctuation pattern. A reduction of the fluctuation amplitude of about 4% can be estimated. The dynamical fluctuations observed in the data set including rescattering are still above the level found in central Pb+Pb collisions. In order to estimate the significance of the reduction of the fluctuation signal from microscopic models including rescattering to the level observed in the data further studies are needed. It is necessary to determine the amount of fluctuation in the "input channel" of elementary nucleon-nucleon collisions in order to estimate the magnitude of fluctuations expected from local conservation laws in Pb+Pb collisions. It is not enough to study the fluctuations in p+p events produced by microscopic models because these depend on the parameters of the given model and can vary over a rather large range (see above). To get a decicive result this value has to be determined more precisely, if possible [76] directly in p+p interactions as measurable by the NA49 experiment.

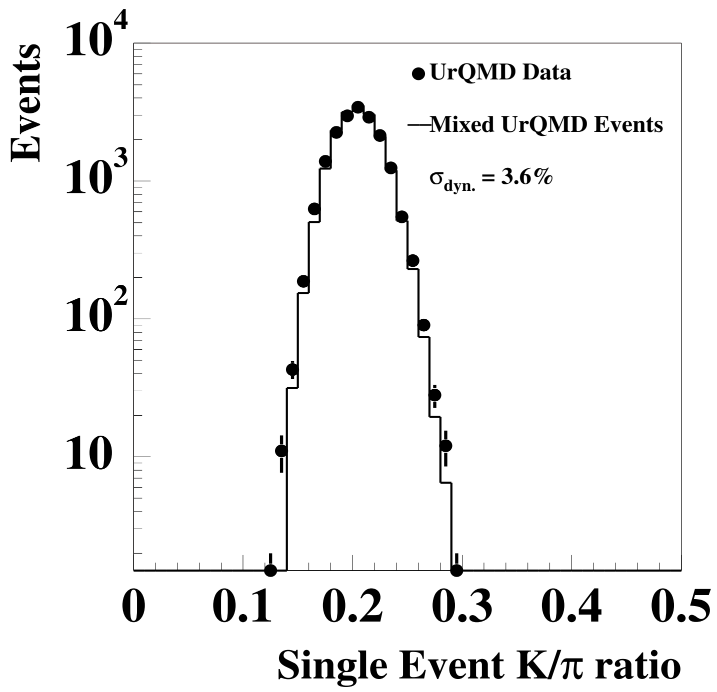

Figure 6.11 Event-by-event K/π-ratio distribution for the UrQMD model and the corresponding mixed event distribution.

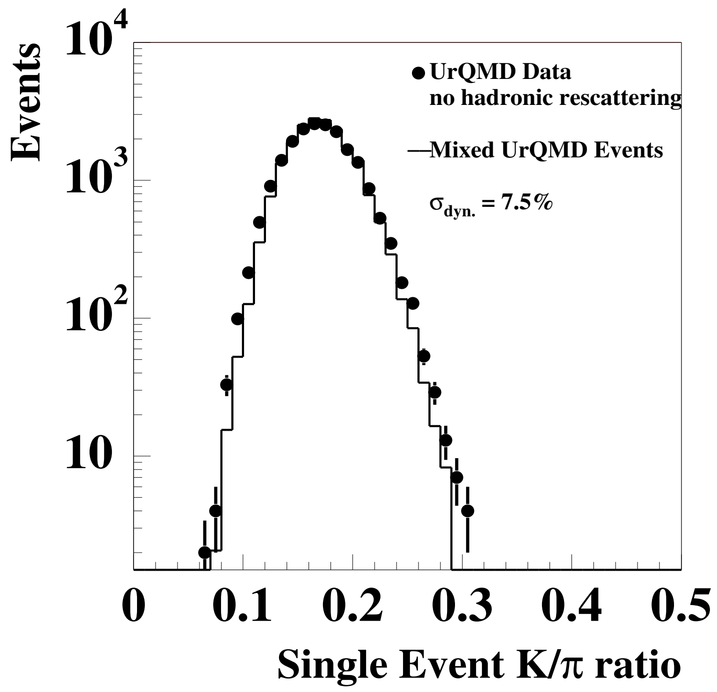

Figure 6.12 Event-by-event K/π-ratio distribution for the UrQMD model without hadronic rescattering and the corresponding mixed event distribution.

6.6 Statistical Models

Recent publications have shown that statistical models [10, 11] are very successful in describing particle yields observed in $e^+ + e^-$, p+p and A+A collisions by characterizing the particle source by few thermodynamically inspired variables such as temperature T, baryo-chemical potential μ_B, and strangeness suppression factor λ_s. A prerequisite for the applicability of statistical models is the chemical equilibration of the particle emitting source.

Naively one would expect a chemically equilibrated system to show only a small amount of fluctuations. Recent calculations of the fluctuations of the event-by-event K/π-ratio [72] expected from a thermally and chemically equilibrated resonance-gas model indeed predict dynamical fluctuations of about 2%, which is consistent with the value observed in our data. The origin of the fluctuations in this model is the decay of higher resonances present at chemical freeze out into kaons and pions, or pairs of kaons or pions. The decay of resonances features a correlated or anti-correlated production of particles depending on the decay channels. This results in a widening or narrowing of the event-by-event K/π-ratio distribution as discussed above the different effects partially cancelling each other.

The contribution from the different decay channels has to be estimated from the abundances of the resonances predicted by the model. Note that the influence of resonance decays of a chemically equilibrated system almost fully exhausts the signal observed in the data, without requiring any further fluctuation induced by the strangeness production mechanism.

6.7 Discussion

It has been shown that with the setup of the NA49 experiment fluctuations of the event-by-event K/π-ratio can be measured precisely. The amount of fluctuation observed in the data is surprisingly small. With the measurement presented here dynamical fluctuations of the event-by-event K/π-ratio of 4.0% can be excluded at 90% confidence level. The observed fluctuations are consistent with fluctuations predicted by a thermally and chemically equilibrated resonance gas. The contribution of correlated particle production by the decay of higher resonances to the dynamical fluctuations of the event-by-event K/π-ratio fully exhausts the signal observed in the data.

Comparisions to string hadronic models based on a superposition of elementary nucleon-nucleon collisions to describe heavy ion collisions show a much stronger signal of dynamical fluctuations. The local fulfillment of conservation laws (e.g. strangeness, energy, etc.) inherent to the hadronization process of these models results in a correlated production of particles that can be ruled out by the data. This suggests a statistical hadronization

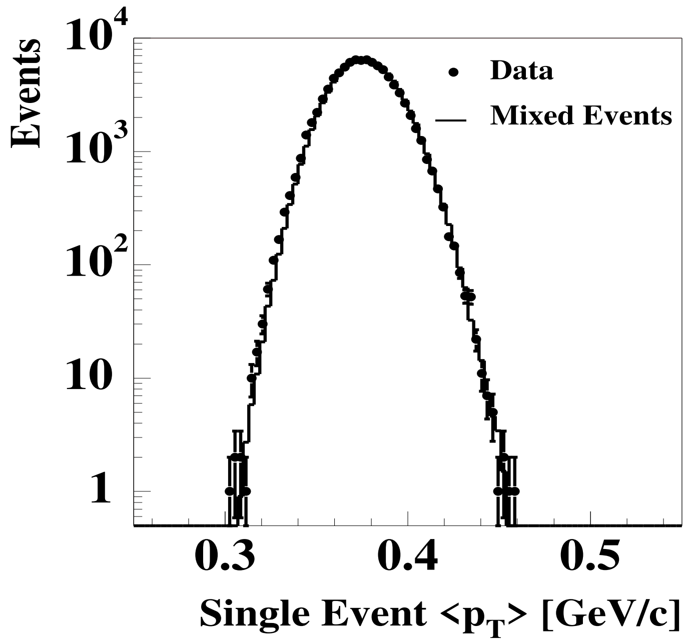

Figure 6.13 Event-by-event distribution of the mean transverse momentum. For comparison, the solid line shows the mean transverse momentum distribution for mixed events.

process from a chemically equilibrated phase, where the conservation laws are fulfilled globally only.
The analysis of fluctations of the average transverse momentum performed by the NA49 collaboration has shown that also in this variable no indications of critical behaviour are observed. Fig. 6.13 shows the event-by-event average transverse momentum distribution for central Pb+Pb collisions and the mixed event reference distribution. We see that the distribution of real events has approximately Gaussian shape and is quite closely matched by the mixed event reference. The observed amount of fluctuations of the average transverse momentum are found to be compatible with independent particle production modified by the known two-particle correlations due to quantum statistics and final state interactions and taking into account the response of the NA49 apparatus. This also supports the assumption of a statistical hadronization process with with the conservation laws fulfilled globally.

The Hadronization Process

However successfull statistical models are in describing the particle abundances, the apparent chemical equilibration of the system can not be reached by inelastic interactions in the hadronic phase of the reaction after the parton-hadron transition of the source. The relaxation time needed to equilibrate the hadronic phase are much longer than the observed lifetime of the system. Instead it was suggested that the apparent equilibration of the resonance populations is an inherent property of the hadronization process itself. In the transition from the partonic to the hadronic phase, the hadronic states are filled according to the available phase space. This process of statistical hadronization naturally leads to a hadronic final state with particle abundances resembling a chemically equilibrated resonance gas whose thermodynamic properties are set by the conditions of the particle source at the point of the parton-hadron phase transition [12]. This picture of statistical hadronization is supported by the fact that a hadro-chemical equilibrium model can be successfully employed [73] to describe the hadron abundances. This model can also be applied to elementary $e^+ + e^-$ collisions, with the parameterset adjusted accordingly. As there is essentially no hadronic rescattering in these collisions among the few hadrons produced, they cannot originate from a stationary state with dynamically maintained population ratios.

This however leads to the conclusion that the strangeness level imprinted on the hadronic final state is reached in the partonic phase of the reaction and remains unchanged during the expansion and cooling of the hadronic phase.

The small amount of flavor fluctuations observed in heavy ion collisions indicate that essentially all events exhibit an identical chemical composition within the limit of finite sampling statistics. Combining this information with the assumption that the strangeness content is set in the partonic phase of the reaction, implies that in every single collision a uniform partonic phase is produced, hadronizing according to a unique set of thermodynamic parameters characteristic to a statistical hadronization process.

6.8 Outlook

The NA49-Experiment was concieved to measure event-by-event fluctuations in heavy ion collisions. The first measurements of fluctuations in "chemical" and "thermal" observables yield very valuable insight in the thermodynamic properties and the hadronization processes of extended systems of strongly interacting matter. To complete this investigation a series of further measurements will be needed. A precise study of the fluctuation pattern of elementary nucleon+nucleon collisions with the NA49-apparatus will provide a reference to further understand and quantify the observed dynamical fluctuations in heavy ion collisions.

The upcoming analysis of data of Pb+Pb Collisions taken at 40GeV/nucleon will feature a test for the hypothesis of appraoching the tricritical point of the phasediagram of strongly interacting matter when probing different regions of the μ_B-T-plane by varying the incident energy of the colliding system.

Of course the next great challenge for the concept of an event-by-event analysis will be the next generation of experiments at the upcoming heavy ion collider facilities at RHIC and LHC.

List of Figures

Bibliography

[1] J. C. Collins and M. J. Perry, Phys. Rev. Lett. **34** (1975) 151.

[2] E. V. Shuryak, Phys. Rep. **C61** (1980) and **C115** (1984) 151.

[3] L. P. Csernai, I. N. Mishustin, A. Mocsy, Heavy Ion Physics, **3**, (1996) 151.

[4] J. Berges, K. Rajagopal, Nucl. Phys. **B**, 538, (1999) 215 1/2.

[5] M. A. Halasz, A. D. Jacson, R. E. Shrock, M. A. Stephanov, J. J. M. Verbarshot, Phys. Rev. **D** 58 (1998) 96007 9.

[6] G. W. Carter, D. Diakonov, Nucl. Phys. **A642** (1998) 78c 1/2.

[7] M. A. Stephanov, K. Rajagopal, E. Shuryak, hep-ph/9806219.

[8] H. Heiselberg, A. D. Jacson, hep-ph/9809013.

[9] T. Alber et al., Phys. Rev. Lett. **75** (1995) 21 3814-3817.

[10] F. Becattini, M. Gazdzicki, J. Sollfrank IKF-HENRG/4-97.

[11] P. Braun-Munzinger, I. Heppe und J. Stachel nucl-th/990310.

[12] R. Stock *Quark Matter Proc.* , Torino, Italy, (1999) to be published in *Nucl. Phys.* **A**

[13] R. Stock, *Nature* **337** (1989) 319-324.

[14] R. Stock, Proceedings of a NATO Advanced Research Workshop on *Hot Hadronic Matter: Theory and Experiment*, 1994, Divonne, France.

[15] St. Mrowczynski, Phys. Lett. **B314** (1993) 118.

[16] M. A. Stephanov, K. Rajagopal, E. Shuryak, Phys. Rev. Lett. **81** (1998) 4816.

[17] M. A. Stephanov, K. Rajagopal, E. Shuryak, hep-ph/9903292.

[18] M. Gazdzicki, St. Mrowczynski, Z. Phys. **C54** (1992) 127.

[19] M. Gazdzicki, A. Leonidov, G. Roland, Eur. Phys. J. **C6**, (1999) 365.

[20] M. Bleicher, M. Belkacem, C. Ernst, H. Weber, L. Gerland, C. Spieles, S. Bass, H. Stöcker, W. Greiner, Phys. Lett. **B435** (1998) 9.

[21] F. Liu, A. Tai, M. Gazdzicki, R. Stock, hep-ph/9909320.

[22] A. Capella, E. G. Ferreiro, A. B. Kaidalov, hep-ph/9903338.

[23] L. Stodolsky, Phys. Rev. Lett. **75** (1995) 1044.

[24] E. V. Shuryak, Phys. Lett. **B423** (1998) 9.

[25] St. Mrowczynski, Phys. Lett. **B430** (1998) 9.

[26] T. Alber et al. (NA35-Collab.), Z. Phys.**C64** (1994) 195.

[27] M. Gazdzicki, D. Röhrich Z. Phys. **C71** (1996) 55-63.

[28] H. Bialkowska et al., Z. Phys. **C55** (1992) 491.

[29] M. Gazdzicki et. al Nucl. Phys. **A556** (1994) 503.

[30] J. I. Kapusta, A. Mekjian Phys. Rev. **D33** (1986) 1304.

[31] S. Afanasiev et al., Nucl. Instr. and Meth. **A430** (1999) 210-244.

[32] J. Harris et al., Nucl. Instr. and Meth. **A315** (1992) 33.

[33] C. Garabatos et al., Nucl. Instr. and Meth. **A283** (1989) 553.

[34] G. Rai et al., IEEE Trans. Nucl. Sci. **37** (1990) 56.

[35] A. Etkin et al., IEEE Trans. Nucl. Sci. **36** (1989) 58.

[36] W. B. Atwood et al., Nucl. Instr. and Meth. **A306** (1991) 446.

[37] F. Sauli, *Principles of Operation of Multiwire Proportional and Drift Chambers*, CERN Report 77-09 (1977).

[38] K. Kleinknecht, *Detektoren für Teilchenstrahlung* , Teubner Studienbücher, Stuttgart (1987).

[39] Orbit Semiconductor, Sunnyvale/CA (USA).

[40] S.A. Kleinfelder, IEEE Trans. Nucl. Sci. **35** (1988) 1988 and **37** (1990) 1230.

[41] F. Bieser et al., Nucl. Instr. and Meth. **A385** (1997) 535.

[42] S.R. Klein et al., STAR Note 239, BNL, Brookhaven, NY (1995).

[43] W. R. Leo, *Techniques for Nuclear and Particle Physics Experiments*, Springer Berlin (1987).

[44] W. Blum, L. Rolandi *Particle Detection with Drift Chambers*, Springer Berlin (1993).

[45] H. Appelshäuser, Dissertation (1997), Universität Frankfurt am Main.

[46] A. Mock Dissertation (1997), Max-Planck-Institut für Physik München.

[47] R. Renfordt, Institut für Kernphysik, Universität Frankfurt am Main, private communication.

[48] H. G. Fischer, CERN, private communication.

[49] U. Fano, Ann. Rev. Nucl. Sc. **13**, 1 (1963).

[50] R. M. Sternheimer, R. F. Peierls, Phys. Rev. B **B3** (1971), 3681.

[51] K. Ambrus, Dissertation (1986), Universität Heidelberg.

[52] L. Landau, *Journal of Physics U. S. S. R.* 8 (1944) 201–205.

[53] E. Fermi, Phys. Rev. **57** (1940), 485.

[54] C. DeMarzo et al., Nucl. Instr. and Meth. **217** (1983) 405.

[55] T. Alber et al., Phys. Rev. Lett. **75** (1995) 3814.

[56] O. Hadeler Diplomarbeit (1995), J.W.Goethe-Universität Frankfurt am Main.

[57] M. Kröcker Diplomarbeit (1995), J.W.Goethe-Universität Frankfurt am Main.

[58] C. Roland Diplomarbeit (1995), J.W.Goethe-Universität Frankfurt am Main.

[59] H. Appelshäuser et al., Phys. Let. B **459** (1999) 679-686.

[60] CERN-Program Library, CERN-IT.

[61] F. Sikler *Quark Matter Proc.* , Torino, Italy, (1999) to be published in *Nucl. Phys.* **A**

[62] M. Toy Dissertation (1999), Univerisity of California, Los Angeles.

[63] H. A. Bethe, Annalen der Physik 5(1930), 325

[64] F. Bloch, Z. Physik 81 (1933), 363

[65] W. Blum et al., The ALEPH Handbook, ALEPH 89-77 CERN(1989).

[66] F. P. Brady, J. Dunn, NA49 Internal Note 85 (1996).

[67] T. Sammer, Dissertation in preparation, Max-Planck-Institut für Physik München.

[68] M. Gazdzicki, Nucl. Instr. and Meth. in Phys. Res. A 345 (1994) 148-155.

[69] B. Andersson, G. Gustavson, and B. Nilsson-Almquist, Nucl. Phys. **281** (1987) 289.

[70] K. Jaeger et al., Phys. Rev. D **9**, 2405 (1975).

[71] X. N. Wang and M. Gyulassy, Phys. Rev. **D 44**, 3501 (1991).

[72] V. Koch, S. Jeon, private Communication, Publication in preparation.

[73] F. Becattini, A. Giovannini, S. Lupia, Z. Phys. **C72**, (1996) 491-497.

[74] S. A. Bass et al., Prog. Part. Nucl. Phys., **41**, (1998) 255.

[75] M. Bleicher et al., J. Phys., **G25**, (1999) 1859-1896.

[76] M. Gazdzicki, Eur. Phys. J. **C8**, (1999) 131-133.

Danksagung

Zuerst möchte ich Herrn Prof. Dr. Reinhard Stock danken, der mein Interesse für die Hochenergie-Kernphysik geweckt und mir die Chance gegeben hat, an dem CERN-Experiment NA49 mitwirken zu dürfen. Herrn Prof. Dr. Herbert Ströbele danke ich für die freundliche Unterstützung und die Anregungen, welche wesentlich zu dem Gelingen dieser Arbeit beigetragen haben. Herrn Dr. habil. Marek Gazdzicki gilt ebenfalls mein Dank für seine Hilfsbereitschaft und die Klärung vieler physikalischer Fragen.
Besonderer Dank gilt meinem Bruder Dr. Gunther Roland für die erfolgreiche Zusammenarbeit, trotz unserer Verwandtschaft, und für sein Vertrauen in meine Fähigkeiten.
Herrn Dr. Rainer Renfordt danke ich für die Zeit, die er sich für die Beantwortung meiner Fragen genommen hat, und für die vielen wertvollen Beiträge zum Entstehen dieser Arbeit.
Bei meinen Kollegen Glenn Cooper und Milton Toy aus Berkeley möchte ich mich herzlich für ihr Mitwirken und für die moralische Unterstützung in den arbeitsreichen Monaten in Genf bedanken.
Ein spezielles Dankeschön möchte ich auch an Herrn Dr. Charles A. Whitten richten, der in der CERN-Cafeteria viel Zeit und Servietten verbraucht hat um mir Dinge zu erklären, die so nicht in den Lehrbüchern stehen.
Ebenfalls bedanken möchte ich mich bei der Frankfurter UrQMD-Gruppe um Herrn Prof. Dr. Horst Stöcker für die freundliche Zusammenarbeit und ihre Hilfsbereitschaft.
Für eine sowohl angenehme wie auch produktive Zeit an der GSI bedanke ich mich bei Herrn Prof. Dr. Braun-Munzinger, meinen dortigen Kollegen und vor allem bei Frau Eisold und Frau Busch.
Der Frankfurter Arbeitsgruppe, insbesondere Herrn Werner Amend, Frau Heidrun Rheinfels-Immanns und Frau Jutta Berschin, danke ich für die Unterstützung und für die vielen und nicht immer selbstverständlichen Hilfestellungen während meiner Zeit am IKF.
Allen hier nicht persönlich genannten Mitgliedern der NA49-Kollaboration möchte ich ebenfalls für die gute und erfolgreiche Kooperation danken.
Größter Dank gebührt an dieser Stelle meinen Eltern, die durch ihre Unterstützung in allen Lebenslagen mein Studium und diese Arbeit erst ermöglicht haben.
Entschuldigen muß ich mich besonders bei meiner Freundin und allen Freunden, Bekannten und Verwandten, die ich in den letzten Monaten sträflich vernachlässigt habe. Danke, daß Ihr trotzdem zu mir gehalten habt!

Curriculum Vitae

Geboren:	26.März.1970 in Frankfurt am Main
Eltern:	Manfred Roland
	Eleonore Roland

Schulbildung:

1976 -	1980	Besuch der Grundschule Wehrheim
1980 -	1982	Besuch der Förderstufe der Christian-Wirth-Schule in Usingen
1982 -	1989	Besuch des Christian-Wirth-Gymnasiums in Usingen
Juni	1989	Abitur

Zivildienst:

1989 -	1990	Zivildienst in der Übergangseinrichtung für Drogenabhängige in Hasselborn

Studium:

Okt.	1990	Studium der Physik an der J.W. Goethe-Universität in Frankfurt
Nov	1992	Vordiplom in Physik ("sehr gut")
Sept.	1993	Aufnahme in das Institut für Kernphysik
Sept	1995	Diplom in Physik ("mit Auszeichnung") Thema der Diplomarbeit: "Positionsbestimmung von Spurendriftkammern mit Hilfe von Laser- und Teilchenstrahlen"
Nov	1995	Förderpreis der Heraeus Stiftung
Okt.	1995	Beginn des Promotionsstudiums am Institut für Kernphysik
Feb.	1996	Wissenschaftlicher Angestellter der Gesellschaft für Schwerionenforschung in Darmstadt
Aug.	1999	Wissenschaftlicher Angestellter des Instituts für Kernphysik der J.W. Goethe-Universität, Frankfurt am Main.